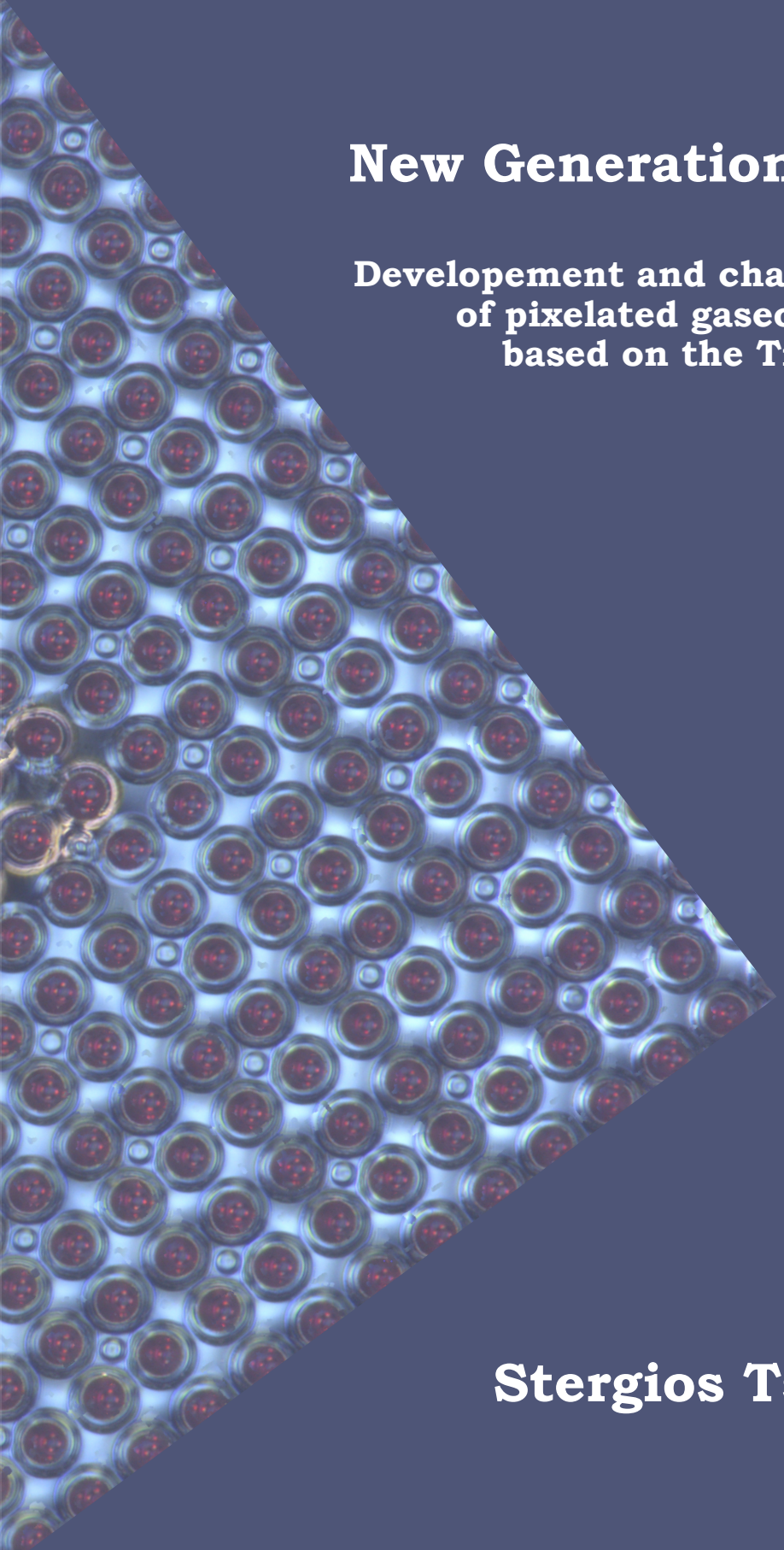

New Generation GridPix

Developement and characterisation of pixelated gaseous detectors based on the Timepix3 chip

Stergios Tsigaridas

Next generation GridPix

≡

Development and characterisation of pixelated gaseous detectors based on the Timepix3 chip

Stergios Tsigaridas

Next generation GridPix

≡

Development and characterisation of pixelated gaseous detectors based on the Timepix3 chip

ACADEMISCH PROEFSCHRIFT

ter verkrijging van de graad van doctor
aan de Universiteit van Amsterdam
op gezag van de Rector Magnificus
prof. dr. ir. K.I.J. Maex
ten overstaan van een door het College voor Promoties
ingestelde commissie, in het openbaar te verdedigen
in de Agnietenkapel
op donderdag 23 November 2017, te 10:00 uur

door

Stergios Tsigaridas

geboren te Kozani, Griekenland.

Promotiecommissie:

Promotor:	Prof. dr. ir. P.J. de Jong	Universiteit van Amsterdam
Copromotor:	dr. N.P. Hessey	TRIUMF
Overige Leden:	dr. N.A. van Bakel	Nikhef
	Prof. dr. ir. E.N. Koffeman	Universiteit van Amsterdam
	Prof. dr. F.L. Linde	Universiteit van Amsterdam
	Prof. dr. T. Peitzmann	Universiteit Utrecht
	Prof. dr. A. Pellegrino	Rijksuniversiteit Groningen
	dr. H.L. Snoek	Universiteit van Amsterdam

Faculteit der Natuurwetenschappen, Wiskunde en Informatica

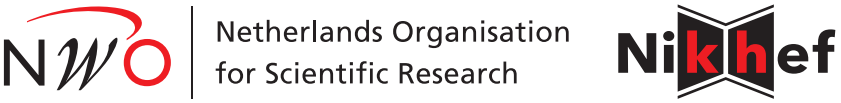

This work is part of the research programme of the Foundation for Fundamental Research on Matter (FOM), which is part of the Netherlands Organisation for Scientific Research (NWO). It was carried out at the National Institute for Subatomic Physics (Nikhef) in Amsterdam, the Netherlands.

A plan view of a GridPix detector focusing on a part of the grid and the pixels below
Typeset by LaTeX.
Printed by Printed by ProefschriftMaken | ProefschriftMaken.nl.
ISBN: 978-946-295-755-8

Στην παρούσα και την μελλοντική
οικογένεια μου

(To my present and future family)

Contents

Chapter 1

Motivation for GridPix

"Αρχάς είναι των όλων ατόμους και κενόν,
τα δ΄ άλλα πάντα νενομίσθαι..."
— Δημόκριτος

1.1 Introduction

The foundation of modern physics is rooted back in the pre-Socratic era when the Greek philosopher Democritus introduced his atomic hypothesis. In his model Democritus states that matter consists of invisible particles called atoms and void i.e. an empty space. The atoms are homogeneous with no internal structure and therefore are indivisible.

Today, about 2500 years after the atomic hypothesis, scientists are striving to come up with a rational interpretation to the remaining unanswered questions regarding the origin of matter and its basic constituents. The past century the advances both at the theoretical and the experimental level led to the formulation of a modern theory called "the Standard Model" which describes the nature of the elementary particles and their interactions.

The interactions between the elementary particles occur at very small scales. In 1924 L. de Broglie proposed that matter has wave properties [1], which suggests that in order to study a small wavelength λ we need a large momentum p. Therefore, large energies[1] are required in order to probe the structure of the matter. Because of this requirement, the study of the elementary particles nowadays is often called high-energy physics.

In modern experiments, large and complex machines called "accelerators" boost particle beams to extreme energies and collide them at one or more interaction

[1]In high energy physics the energy is measured in electron volts (eV). The electron volt is the amount of energy gained by a single electron moved across an electric potential difference of one volt, 1 eV = $1.6 \cdot 10^{-19}$ J. Taking into account Einstein's famous formula about energy-mass equivalence $E = mc^2$, the mass of a particle can be expressed in terms of eV/c^2. Usually, the convention $c = 1$ is used.

points. The centre of mass energy at the interaction point is sufficient in order to create new particles and study their properties. For the recording of the out-coming particles each interaction point is surrounded by detection devices. However, for the successful determination of the path and the properties of the out-coming particles, there is a need for particle detectors.

The GridPix detector is a novel detector concept which enables the reconstruction of particle tracks in three dimensions with high precision within a single module. After a brief introduction to the Standard Model and high energy physics, this chapter describes the motivation for the development of GridPix detectors along with potential applications in high energy and medical physics.

1.2 The Standard Model of particle physics

The field of particle physics is focusing on the study of particles and their interactions. The first particle that was discovered, was the electron by J. J. Thomson in 1897 [2]. Later on, the treatment of the electromagnetic radiation as a particle and the discovery of the atomic nucleus, were two important milestones which revolutionised modern physics and led to the discoveries of many new particles and the further investigation of the structure of matter.

The remarkable progress achieved resulted in the development of a theoretical framework, called the Standard Model of particle physics [3–6], which classifies the fundamental particles according to their spin properties and explains their interactions. The fundamental particles of the Standard Model are divided in two categories, the fermions which are particles with a half integer spin and the bosons which are particles with an integer spin. An overview of the fundamental particles of the Standard Model is given in figure 1.1.

The fermions of the Standard Model are divided into two families, the quarks and the leptons. In total there are six quarks, six leptons and their corresponding antiparticles (with the same mass and opposite charge). The fermions of both families are split in three "generations" which are formed by one pair of quarks and one pair of leptons. The first generation is composed by a pair of the up and the down quark (u, d) and the lepton pair of the electron and the electron-neutrino (e^-, ν_e). The charm and the strange quark (c, s) along with the muon and its neutrino form the second generation. In the third generation the quark-pair consists of a top and a bottom quark (t, b) and the lepton-pair includes the tau and the tau-neutrino (τ, ν_τ).

The fermions of the second and the third generation possess larger masses compared to the fermions which constitute the first generation. Therefore these fermions are unstable and they decay to lighter fermions. The ordinary stable matter that we know consists of the lightest fermions of the first generation.

The interaction between the fermions is expressed as an exchange of gauge bosons (see figure 1.1) which are the mediators of the four fundamental forces of nature, in relative strength order:

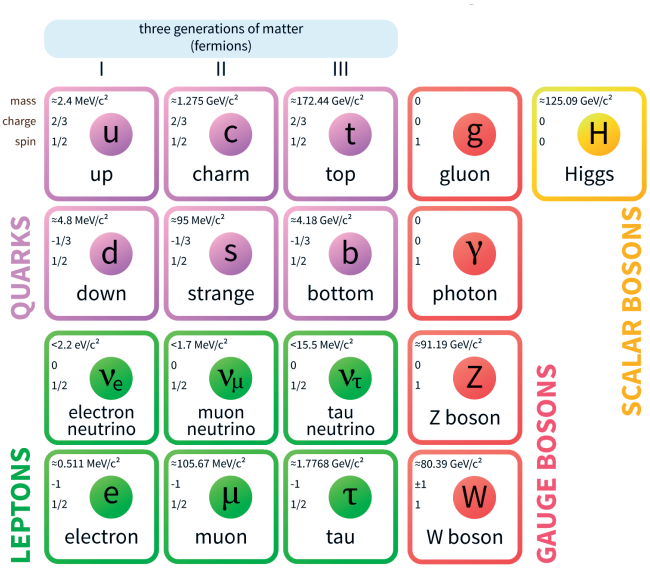

Figure 1.1: *An illustration of the classification of the elementary particles of the Standard Model. The particles are sorted according to their properties.*

- **Strong interaction:**

  In nature except the elementary particles we also observe another category of composite particles called hadrons. The hadrons are divided in two families, the mesons which consist of a quark-antiquark pair and the baryons which are combinations of three quarks. A typical example of mesons is the triplet of pions (π^+, π^0, π^-) (the superscript denotes the charge) which are the lightest mesons. On the other hand, famous baryons are the neutron (n) and the proton (p) which constitute the nuclei. The quarks in these particles are bound together due to the strong interaction. The strong force is mediated by the massless gluons and has a typical range of 10^{-15} m.

- **Electromagnetic interaction:**

  The electromagnetic interaction is the second force of nature in terms of strength and is mediated by the photon (γ). The electromagnetic force takes effect on charged leptons and quarks and depends strongly on the distance. Its the range is infinite and explains why the electrons are bound in the atoms and many other phenomena of every day life.

- **Weak interaction:**

  The weak interaction is a short-ranged fundamental force acting on the fermions of the Standard Model. The term weak is assigned to this interaction

due to its field strength which is a few orders of magnitude lower for a given range compared to the electromagnetic and the strong interaction. For very small distances though the weak force becomes stronger than the electromagnetic interaction. The weak interaction is expressed as the exchange of massive gauge bosons, namely the (W^+, W^-, Z). The weak interaction is responsible for the beta decay (β^-) in nuclear physics. The weak and the electromagnetic interaction are described under a unified theory called the electroweak theory.

- **Gravitational force:**

  The fourth and weakest fundamental force of nature is gravity. The range of gravity is infinite, however due to its strength which is many orders of magnitude lower than the other three forces, it has a negligible impact on the elementary particles. Gravity is a classical field theory described by the general theory of relativity introduced by Einstein and there is no quantum analogue. Therefore particle physicists quite often refer only to the first three forces of nature.

In its early days, the elementary particles of the Standard Model were treated as massless which of course contradicts the experimental observations. However, in 1964 P.W. Higgs and F. Englert together with R. Brout in separate works [7–9] proposed a mechanism which explains how the W^+, W^- and the Z bosons acquire mass within the Standard Model. This mechanism is known as the Brout-Englert-Higgs mechanism and is accompanied by a scalar boson called the Higgs boson (see figure 1.1). The experimental observation of the predicted Higgs boson is the last remaining piece in order to verify the Standard Model. In 2012, a new particle consistent with the Standard Model Higgs boson was observed experimentally by the ATLAS and the CMS collaboration at CERN, [10,11]. So far there is no indication for deviations from the Standard Model, however additional precision measurements have to be performed.

1.3 Experiments at the high-energy frontier

In particle physics experiments, one of the main objectives is to reach energies high enough to enable the creation of new particles or the study of the structure of the composite ones. Up to the first half of the previous century the only available "source" of high energy particles was cosmic rays or particles from radioactive decays. However, cosmic rays provide particles which vary in energy and type. The breakthrough in this respect came with the development of the accelerators.

Accelerators are machines that can speed up charged particles to high energies by making use of electric fields. The first accelerators built were the Cockcroft-Walton and the Van der Graaff accelerators, [12,13]. Both techniques make use of electrostatic fields for the acceleration and have been used extensively in the early years. However the fact that they require extremely high electric fields in order

to reach an adequate energy, their operation and maintenance becomes a tricky problem.

In order to overcome such limitations a second accelerator type was introduced, which makes use of alternating electromagnetic fields for the acceleration. The first accelerator of this type was the linear accelerator also known as "linac" [14], introduced by R. Wideröe and improved later on by R. Alvarez et al. [15]. At the same time, the basic idea behind the linac has been has been used by E. O. Lawrence and M. S. Livingston in order to construct a circular accelerator called the cyclotron, [16].

The linac and the cyclotron revolutionised particle physics experiments. The alternating electric fields along the accelerator cavities are switching at a given frequency and therefore push the particles forward. The use of several consecutive cavities enables the acceleration of particles at higher energies. The extraction of the particles is usually performed in bunches while magnets are used in order to focus or steer the particle beam if necessary.

Both linear and circular accelerators have been used in a wide range of applications in physics and medicine. In the beginning the accelerators were used for fixed target experiments. However, soon enough it was realised that accelerators can be used in order to perform colliding beam experiments. In these experiments, two separate particle beams are accelerated by two linacs or in opposite directions at a circular accelerator and are collided at dedicated interaction points. The advantage compared to the fixed target experiments is that the total energy of the two beams is available at the centre of mass.

In the modern experiments, the so-called colliders are part of a large complex consisting of several parts. The most common type used is the synchrotron where the particles move in a closed-loop path. The acceleration of particles is performed in several stages before entering the synchrotron. At the final stage the particle beams are accelerated at the maximum energy. Such machines can be used in order to accelerate beams of electrons, protons or heavy ions to extreme high energies.

At the designated interaction points the beams are crossed and interactions between the particles may occur. The production of new particles strongly depends on the energy at the centre of mass of the colliding beams. Therefore for the production of heavy particles it is necessary to build large machines able to deliver an energy at the centre of mass to the order of several TeV. The production rate also depends on the specific physics process which takes place. For a given process, the production rate $\mathcal{R}$ is defined as,

$$\mathcal{R} = \sigma \cdot \mathcal{L} \tag{1.1}$$

In eq. 1.1, the parameter σ is the cross section which is related to the probability of the given process to occur. The cross section depends on the centre of mass energy and is usually expressed in terms of area. The parameter $\mathcal{L}$ is called luminosity and depends on the parameters of the accelerator. The unit of the luminosity is $\mathrm{cm}^{-2}\,\mathrm{s}^{-1}$.

Nowadays the largest accelerator complex is located at the European Organisation for Nuclear Research (CERN) in Geneva. Beginning in the 80's an underground

tunnel with a circumference of 27 km was built in order to host the Large Electron-Positron (LEP) collider. The LEP was able to deliver a centre of mass energy from 91 GeV up to 209 GeV and was used for the detailed study of the electroweak theory and the Standard Model in general through the production of the $W^{\pm}$ and the Z bosons. Until its decommission in 2000 the LEP collider has been used for detailed studies of the electroweak theory and the precise determination of basic Standard Model quantities like the masses of the W and the Z bosons.

The same tunnel is used currently for the Large Hadron Collider (LHC), figure 1.2. The LHC is currently the world's most powerful machine for high-energy physics experiments. The LHC was designed in order to collide proton beams with a centre of mass energy of 14 TeV and a luminosity of 10^{34} cm^{-2} s^{-1}, [17]. In each one of the four interaction points, one of the large experiments is installed, namely A Large Ion Collider Experiment (ALICE) [18], A Toroidal LHC Apparatus (ATLAS) [19], Compact Muon Solenoid (CMS) [20] and Large Hadron Collider Beauty (LHCb) experiment [21].

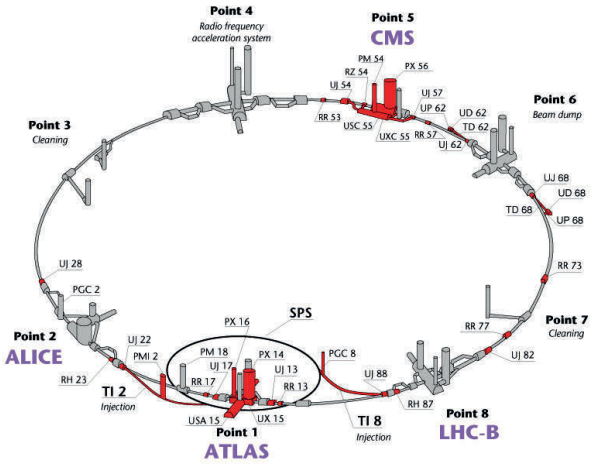

Figure 1.2: *The current layout of the LHC showing the location of the ALICE, the ATLAS, the CMS and the LHCb experiments. The proton beams are accelerated in several stages and reach 450* GeV *at the Super Proton Synchrotron (SPS). Finally the beams are transferred in the LHC where they are accelerated in opposite directions to their maximum energy.*

The proton beams are accelerated in opposite directions in two separate beam pipes. The pipes are kept at high vacuum and for the steering of the beams strong superconducting electromagnets are used. During operation, the electromagnets are cooled down to a temperature of -271.3 °C which is even lower than the temperature of the outer space (-270.5 °C).

The first proton beams were circulated successfully in the LHC in 2009. The first data from proton collisions were recorded in early 2010 at a centre of mass energy of 7 TeV with a time between bunch-crossings of 50 ns. The following years the energy was increased to 8 TeV as the machine was delivering a growing luminosity. The analysis of the data collected from the experiments in the first run period (Run-1) revealed significant results, having as a highlight the observation of the Higgs boson.

With many questions still puzzling the scientists, the LHC has a rich physics programme to accomplish. After a technical stop for maintenance and necessary preparations, the LHC today is in the middle of Run-2. Thanks to the developments, the LHC in Run-2 delivers a centre of mass energy of 13 TeV with a time between bunch crossings of 25 ns and would be able to reach the nominal design values for the centre of mass energy and the luminosity. In the future, the planning includes two more technical stops in order to prepare the machine for Run-3 and the high luminosity LHC era (HL-LHC), [22]. The HL-LHC is expected to deliver luminosities 5-7 times larger that the nominal design ($\mathcal{L}$ =10^{34} cm^{-2} s^{-1}). The increased number of collisions enables the study of rare physics processes.

Over the past few years the LHC was the first collider able to bring physics at the TeV scale. Due to its high energy and the composite nature of the proton the LHC can probe physics processes over a large energy range. Since the proton is not an elementary particle, its energy is shared among its constituents. Taking into account this fact, only a random fraction of the proton energy is involved in the collisions.

The LHC and hadron colliders in general, due to their ability to scan a large energy range without modifying their parameters, have a large discovery potential and therefore quite often are referred to as "discovery machines". However, the fact that the initial state of the collision is not known, limits the precision of the measurements.

In order to overcome the limitations of the hadron colliders, lepton colliders can be used. In the past, the discoveries made at hadron colliders were followed by the construction of lepton colliders for precision measurements. The leptons are elementary particles and therefore the initial state of the collisions is known precisely. This advantage of lepton colliders was exploited for example by the LEP collider in order to produce large amounts of Z or $W^{\pm}$ bosons.

The properties of the newly discovered Higgs boson have to be studied in detail. Moreover, there are still phenomena observed in nature which can not be explained by the Standard Model, for example like the matter-antimatter asymmetry and the nature of dark matter and dark energy. For such measurements unprecedented precision is required which motivates the realisation of a new generation lepton collider. The design of the future lepton collider is crucial and several technologies are currently under consideration.

One of the basic requirements for the lepton collider would be the delivery of energies at the centre of mass up to the TeV scale. In order to achieve such energies a future circular lepton collider would require a tunnel which is larger compared to the one which is located at CERN and currently is used for the LHC. A limiting

factor for the large circular lepton colliders is the energy loss of the particles per turn due to the emission of synchrotron radiation[2].

The average energy loss ΔE of a relativistic charged particle of mass m and energy E per turn in a circular collider with radius r is given by,

$$\Delta E \propto \frac{1}{r} \cdot \left(\frac{E}{m}\right)^4 . \tag{1.2}$$

The eq. 1.2 suggests that for a high energy circular lepton collider, in order to compensate for the energy loss per turn we should go to a larger radius or even to combine a larger tunnel with the use of heavier leptons, such as muons. Currently there are two collaborations focusing on the study of future circular electron-positron colliders with a circumference up to 100 km, the Future Circular Collider (FCC) at CERN [23] and the Circular Electron Positron Collider (CEPC) in China [24].

Another possibility to explore high energies would be to build a linear lepton collider where the particles would be accelerated in one go before the collisions. Today, two projects are under consideration for the construction of the future linear collider, the International Linear Collider (ILC) and the Compact LInear Collider (CLIC). Both projects aim to perform the same physics however the proposed accelerator technology differs.

The ILC design will be based on superconducting magnets and has a centre of mass energy of 250 GeV upgradable to 500 GeV and 1 TeV. Figure 1.3 shows an illustration of the layout of the ILC. On the other hand, the CLIC features a new two-beam acceleration where the main beam is powered by a second beam called the drive-beam, figure 1.4. The CLIC machine would be able to deliver energies at the centre of mass beginning from 360 GeV up to 3 TeV. More information about both projects along with the conceptual design reports can be found at the dedicated websites [25,26]. The decision on which technology will get the final approval for the construction is a function of several variables and is beyond the scope of this thesis.

1.4 Particle detectors

In modern colliding beam experiments the particle beams are brought into collision at the interaction point. The amount of energy that is involved in the collisions quite often is sufficient in order to produce new particles. These particles however may be unstable and after a short time the unstable particles decay to secondary particles which fly away from the interaction point.

Each interaction point is surrounded by a detector system which is responsible for the determination of the path and the properties of the produced particles. The detector is accompanied by a magnet system which provides information about

[2]The electronmagnetic radiation that is emmitted when charged particles are accelerated in a curved path. This type of radiation is emmitted by relativistic particles in circular accelerators called synchrotrons and therefore is referred as synchrotron radiation.

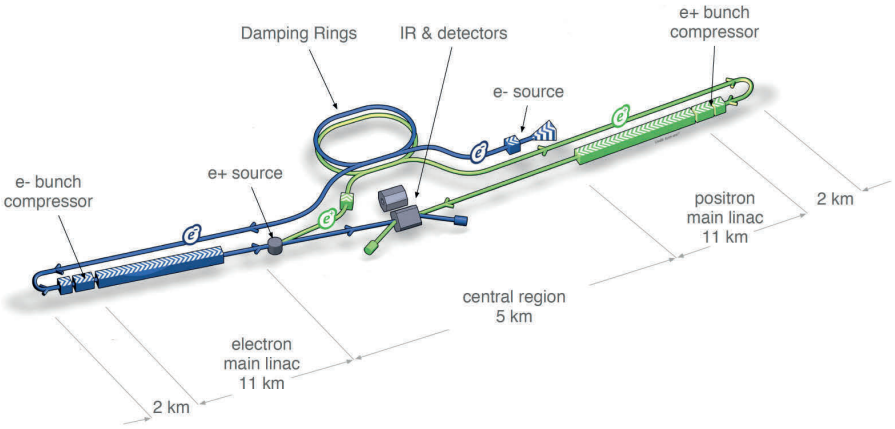

Figure 1.3: *The proposed layout of the International Linear Collider (ILC). For the acceleration the ILC will make use of superconducting magnets*

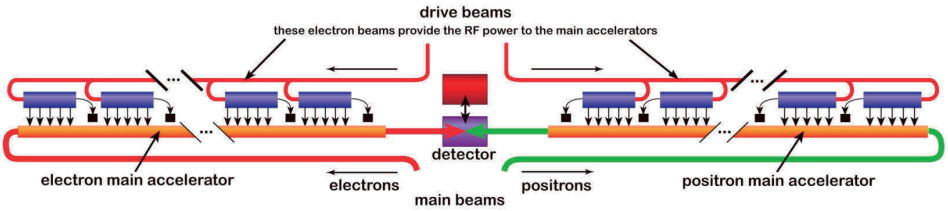

Figure 1.4: *The proposed layout of the Compact LInear Collider (CLIC). The energy of a high-intensity drive beam is used to power up the main electron and positron beams.*

the particle charge and enables the momentum measurement. By combining the information obtained by the sub-detector systems we can reconstruct which particles have been created during the collisions since their products leave a unique signature in the detector.

The layout of a modern detector system is illustrated in figure 1.5. The detector system consists of a stack of several sub-detectors which have a specific functionality. The most important sub-detectors are the following:

- **Tracking detectors:**

  Such detectors are placed close to the interaction point and are responsible for the determination of the track of the particles with high accuracy. The track information is then used in order to reconstruct the primary or the secondary vertex. Under the presence of the magnetic field it is also possible

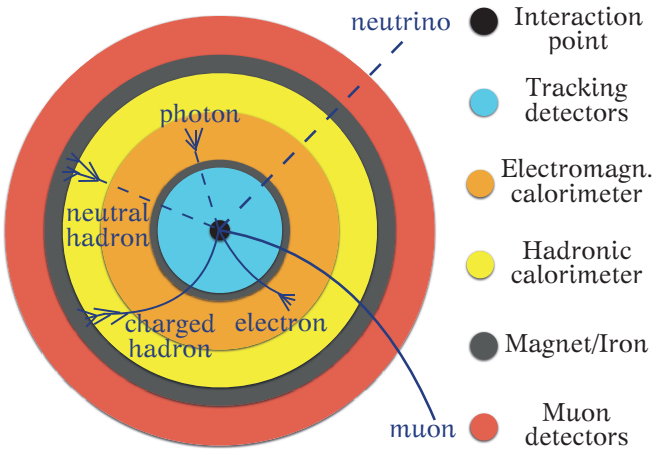

Figure 1.5: *An illustration of the cross section of a typical detector used in high energy physics experiments. The interaction point where the collisions occur is surrounded by the sub-detector systems and the magnet system. The electric signals created in the sub-detectors provide all the necessary information about the out-coming particles.*

to measure the curvature of charged particles and therefore their momentum. Nowadays the majority of the tracking detectors make use of a gas mixture or a semiconductor as active medium.

- **Calorimeters**:

  The calorimeters are devices which measure the energy of charged or neutral particles in a destructive way. This means that the particles stop in the detector and the deposited energy in the active medium is measured. There are two basic types of calorimeters, the electromagnetic calorimeter (ECAL) and the hadronic calorimeter (HCAL). The ECAL is used in order to measure the energy of the electrons and the photons which interact electromagnetically and are absorbed completely. On the other hand the HCAL is used to stop particles which interact with the strong force i.e the hadrons. The active medium choice depends on the application and can be a semiconductor, a gas mixture, a noble liquid or a scintillating crystal.

- **Muon detectors**:

  The outer layers of the detector are covered with the sub-detector system known as the muon spectrometer. The muons are particles that can travel through several meters of dense media and leave their trace in all the sub-detectors. The muon chambers are used to reconstruct the track of the muons and to measure

their momentum. In addition they provide precise timing information that is used for triggering purposes. The muon chambers are large area detectors and therefore it is more convenient to use gas as a detection medium.

Additional to the basic sub-detectors that were discussed before, there are also special sub-detectors known as particle identification detectors. Such detectors aim to identify of particles by measuring their mass. The mass of a particle can be obtained by measuring its velocity for a given momentum.

1.5 The GridPix detector concept

The developments in high energy physics experiments follow the technological evolution. As a result the experiments become more and more demanding. From the point of view of the detectors there is an everlasting hunt towards the improvement of the performance in terms of precision and reliability.

In the early years, the detectors that were used for particle tracking were based mostly on gas leading to many discoveries. Later on, thanks to the rapidly emerging CMOS[3] technology, semiconductors and especially silicon found immediate application in particle physics as sensitive detection medium. Today, the majority of the inner tracking detector systems in high energy physics experiments are based on silicon detectors in combination with Application Specific Integrated Circuits (ASIC). In simple words the ASIC is a chip used for the readout of the electric signals that are generated by the particles in the active medium.

Due to their high segmentation, silicon planar detectors provide excellent position resolution. A single silicon planar detector gives the crossing point of a particle track at the detector plane with a precision of a few micrometers (1 μm = 10^{-6} m). Hence the full information of the track in three dimensions can be obtained by stacking several detector layers. This however increases the material budget of the detector and particles interacting with the silicon might be deflected from their original path. Moreover one of the major concerns about silicon sensors is the deterioration of the performance due to radiation damage after a long term usage in harsh radiation environments.

An innovative detector concept with a high potential for use in tracking applications is the GridPix detector. The GridPix concept combines a gas layer as a detection medium with a CMOS pixel chip for the readout. This technology enables the construction of low mass and relatively low cost detectors. Since the gas is constantly flushed through the detector the detection medium is renewable which increases significantly the radiation tolerance.

The basic element of the GridPix detector is the integrated grid (InGrid), shown on the left of figure 1.6. The InGrid is fabricated with photolithography techniques

[3]Complementary metal-oxide-semiconductor or CMOS is a technology used for the fabrication of integrated circuits.

directly on top of a CMOS pixel readout chip. The whole structure is enclosed in a gas tight chamber. A traversing particle releases electrons in the gas which are multiplied, creating an electric signal which is collected by the readout chip. For more information about the working principle as well as the detector geometry see the following chapters.

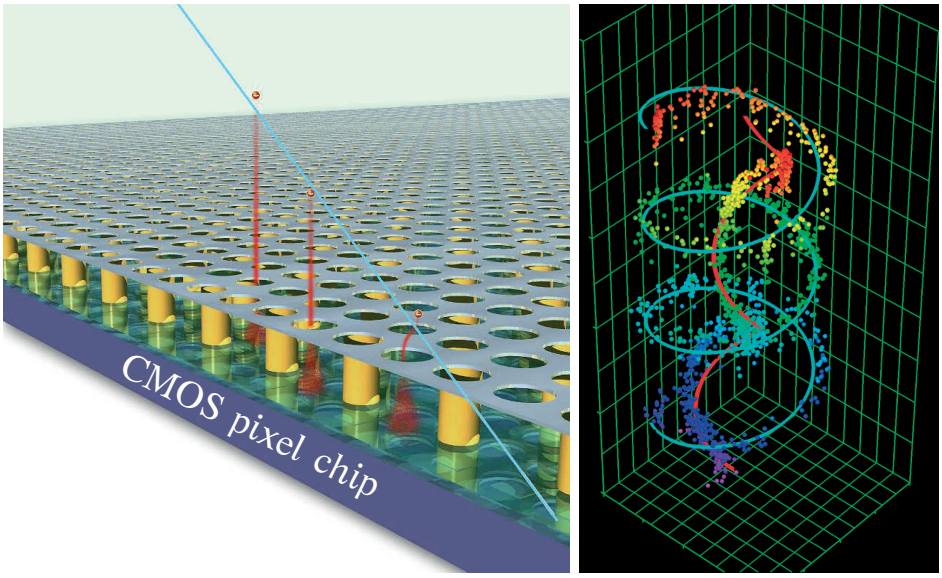

Figure 1.6: *On the left, an illustration of the GridPix detector concept. On the right, an event display of two electron tracks emitted from a* ^{90}Sr *source. The event was recorded with a GridPix detector operating in a magnetic field. The detector is able to record every single electron (coloured dots) released by the incoming particles. The colour corresponds to the drift time of the electron from its creation position to the grid. Pictures are taken from* [27].

Thanks to the detector specifications and the functionality of the chip a single GridPix module is able to reconstruct with high accuracy a track segment in three dimensions instead of a single point. The best feature however of the GridPix detector is the ability detect all the single electrons that are created from particles crossing the active volume of the detector. As a result a reconstructed event with a GridPix detector contains the full information of the track, enabling at the same time energy loss measurements. For example figure 1.6 (at the right) shows an event recorded with a GridPix detector operating in a magnetic field. This events shows the tracks of two highly energetic electrons emitted from a ^{90}Sr source. These electrons lose a fraction of their energy by knocking out single electrons from the gas atoms. The coloured dots in the figure correspond to the creation position of all the single electrons released by the traversing fast electrons.

The GridPix detector shows a great potential for tracking applications in high-energy physics experiments or medicine. However despite the excellent tracking performance there are still a few steps to take so that GridPix becomes a mature technology. Limitations set by the readout chip and the discharges occurring in the gas, at the moment prevent the use of GridPix in future high energy physics experiments. In this thesis we address these questions and perform research towards the improvement of the performance and the construction of reliable GridPix detectors in the future. In the next section we discuss a few potential applications of the GridPix detectors.

1.6 Potential applications of GridPix detectors

1.6.1 GridPix in the ATLAS experiment

The ATLAS experiment

ATLAS is one of the four large experiments at the LHC at CERN. Its detector system has a cylindrical shape with a length of 44 m and a diameter of 25 m. The various sub-detector systems are placed in concentric layers following the detector scheme presented in section 1.4. An illustration of the ATLAS detector is shown in figure 1.7.

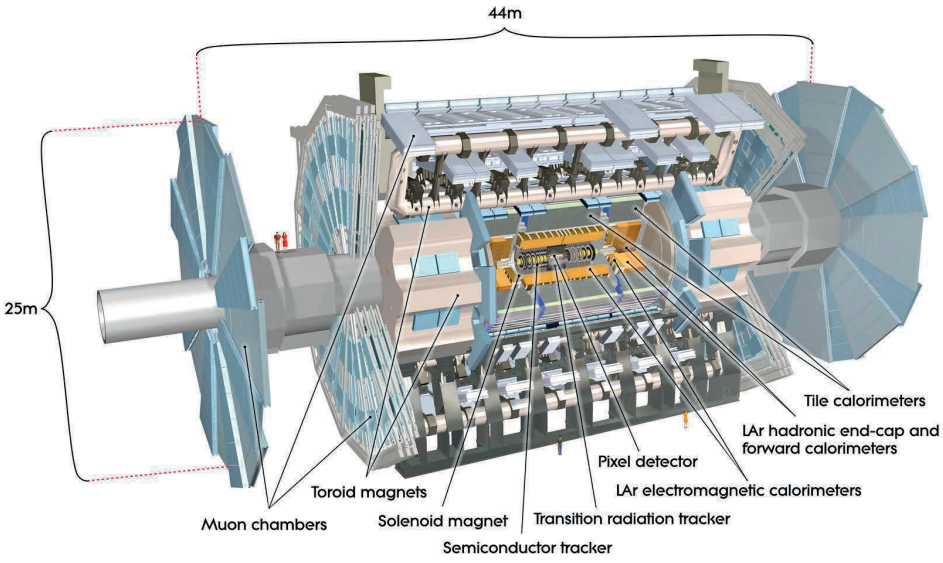

Figure 1.7: *A schematic of the ATLAS detector at CERN showing its various sub-detector systems.*

The ATLAS inner detector

The ATLAS Inner Detector (ID) is the sub-detector system that is placed close to the interaction point. Figure 1.8 shows the current layout of the ID after the upgrade for the Run-2. In total it consists of three sub-systems arranged in concentric barrel layers, covering a radial distance of about 1 m.

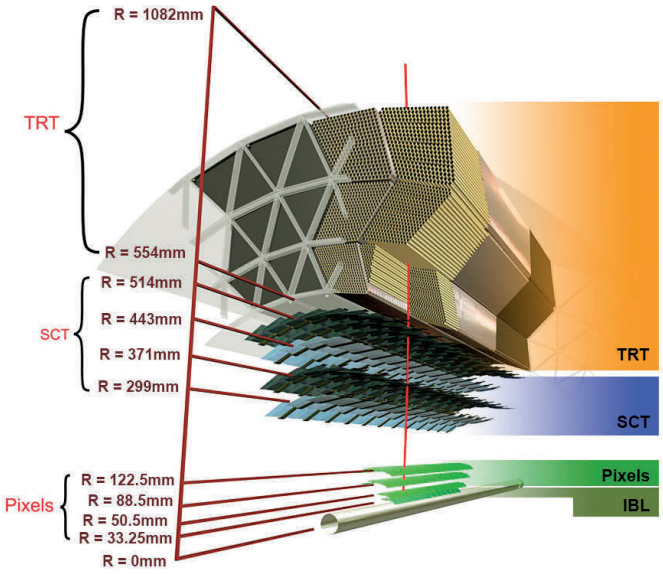

Figure 1.8: *An illustration of the layout of the Inner Detector of the ATLAS detector experiment including the recently istalled Inserticle B-Layer (IBL),* [28].

The innermost sub-system is the Pixel Detector (PD) which consists of three layers of hybrid silicon pixel detectors, the inner layer being about 50 mm away from the beam line. Three layers of end-caps on each side complete the barrel for full coverage. During the shutdown for maintenance and the preparations for Run-2 a fourth pixel layer at a distance about 30 mm from the beam line was installed in order to improve the performance. Four barrel layers and nine end-cap layers on each side of silicon micro-strip detectors, follow the PD and form the sub-system known as the SemiConductor Tracker (SCT). The last component of the ID is the Transition Radiation Tracker (TRT) which contains 73 layers of thin-walled straw tubes for the barrel and 160 layers for the end-caps. The chambers are filled with a Xenon-based gas mixture and are used for tracking and particle identification.

The GridPix as track trigger in ATLAS

The ATLAS experiment is already planning the upgrade of its detector system in order to cope with increased track rates at the HL-LHC. For the HL-LHC conditions the expected total track rate at the outer layers of the ID would be at the order of 1 MHz $cm^{-2}s^{-1}$, [29]. However, the low momentum tracks are not interesting for the physics and have to be rejected. A GridPix detector equipped with on-chip pattern recognition would be able to perform basic track fitting and reject the low momentum tracks. The reconstructed 3D track in the GridPix detector, due to the high positional and angular accuracy can be used in order to trigger only on interesting tracks.

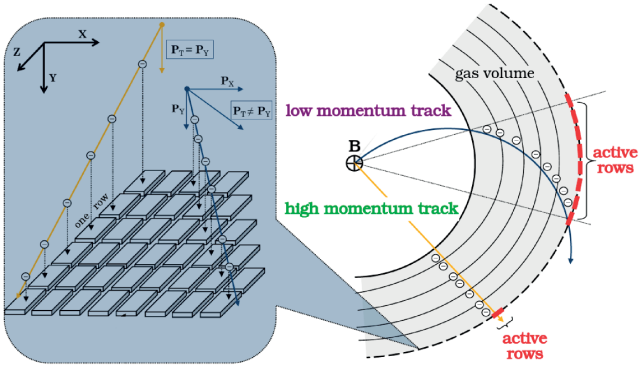

Figure 1.9: *An illustraction of the principle for the track triggering with GriPix in the ATLAS experiment. For more details see the text. Picture is taken from* [30].

The principle is illustrated in figure 1.9. When a charged particle moves in a magnetic field it follows a curved trajectory. The curvature however of the track depends on the momentum of the particle. As a result a low momentum track is characterised by its high curvature, while a high momentum particle is hardly affected by the magnetic field and its track practically follows a straight-line.

A low momentum particle will generate many electrons along its track through the active gas volume of a GridPix detector. In a well-aligned pixel array this results in electric signals which will be collected by several pixels. Due to the large curvature of the low momentum track the pixels fired will belong to different rows. On the other hand, for the high momentum track the pixels fired usually belong to the same row. The number of "active" rows can be a measure of the momentum of the particle.

A future application of the GridPix detector as a track trigger in the ATLAS experiment offers an alternative solution for the reduction of the track rate in the HL-LHC. The advantage of the GridPix in this respect is that only a single detector layer is required which reduces significantly the material budget. In addition to the

track trigger, the identification of particles can be done in combination with the calorimeters or by adding a radiator in front of the detectors as demonstrated in [31]. However, this is still on a preliminary stage and more tests have to be performed.

1.6.2 GridPix in a future linear collider

The International Large Detector concept

The ILC project that was described in section 1.3 in its preliminary design is expected to host two detector systems. The reason for this is based on the prior experience which suggests that multiple experiments targeting the same physics case are required for the systematic cross-checks and the experimental validation of the results obtained.

The proposed scheme implements two detectors installed on a push-pull machine in order to share the same interaction point. The International Linear Detector (ILD) is one of the two detector baseline systems that were proposed for the ILC. The foreseen detectors are the Silicon Detector (SiC) based on an all-silicon tracker and the International Large Detector (ILD) where the main tracking detector would be a large area Time Projection Chamber[4] (TPC). Figure 1.10 shows the layout of the ILD. For detailed information about the design consult the technical design report [32].

GridPix as the TPC readout in the ILD.

The baseline design of the ILD is a hybrid detector which combines silicon strips and pixels arranged in concentric layers with a TPC. The silicon detectors would be placed close to the interaction point for the precise determination of the vertex. However its basic feature would be a TPC able to perform continuous tracking and particle identification based on the energy loss measurement.

The TPC is a large volume cylinder filled with gas which consists of the main barrel and two endplates. In colliding beam experiments the TPC is placed in such a way that the interaction point is in the centre of the barrel. An electrode at the central plane acts as cathode while the endplates are equipped with detectors for the readout of the electric signals that are generated by traversing particles.

The main technologies that are proposed for the readout of the ILD TPC are the Micromegas and the GEM which are discussed in chapter 3. However an alternative technology of the readout which is under consideration is the GridPix detector. Thanks to its high granularity and the pixel functionality the GridPix is an excellent candidate for the readout of a TPC. The high-precision track reconstruction as well as the great potential for particle identification due to the detection single electron meet the requirements for the precision physics at the ILC.

In 2015, a Pixel-TPC demonstrator [33] was constructed and tested in an electron beam at the Deutsches Elektronen-Synchrotron (DESY). For the readout of the

[4]The Time Projection Chamber (TPC) and its working principle are explained in the following chapters.

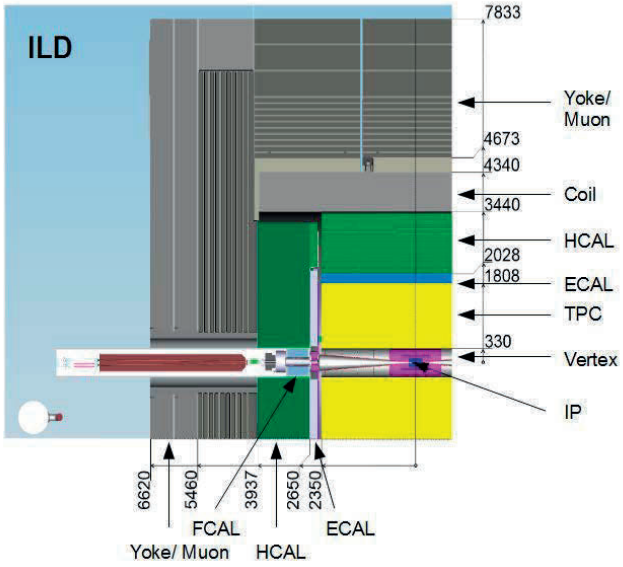

Figure 1.10: *An illustration of a quadrant view of the International Large Detector (ILD) concept showing its various sub-detector systems. The dimensions are in* mm. *Picture is taken from* [32].

modules in total 160 GridPix detectors were used. This study is the proof of concept that the successful construction and operation of large area detectors based on GridPix is feasible. However, further studies and the development of GridPix detectors on more sophisticated readout chips is required.

1.6.3 GridPix in medical physics

Treatment with protons

A large part of the field of medical physics nowadays is focusing on the diagnosis and the treatment of cancer. Lately, a common modality that is used for the treatment is the radiation therapy. This kind of therapy is making use of ionising radiation on in order to target the DNA in the tumour cells aiming to destroy of the tumour cells.

The conventional techniques that are used for this purpose are based on the irradiation with X-ray photons. However, the photons on their way to the tumour, release a significant fraction of their energy in the surrounding tissue. As a result the delivered dose to the normal tissue before and after the tumour is increased. In addition, the photons under certain circumstances can knock out an atomic electron (Compton scattering), which in turn causes additional damage to the surrounding

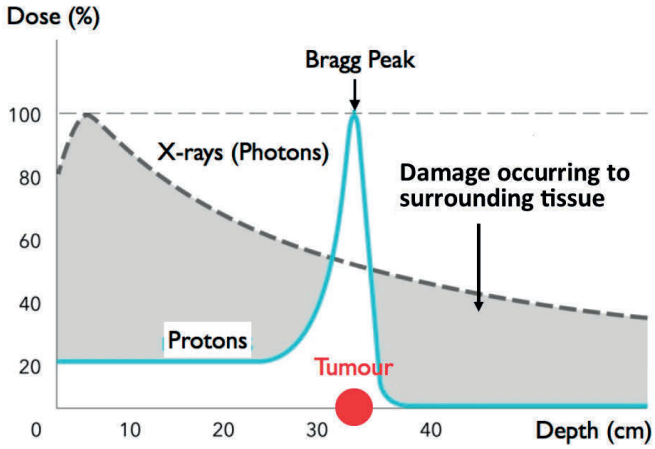

Figure 1.11: *A comparison of the relative dose delivered to a tissue versus the penetration depth during irradiation with photons (dashed curve) and protons (solid curve). The photons deposit a significant amount of dose in the normal tissues around the tumour. On the contrary, the protons deposit the maximum dose within the tumour, miniming the damage to healthy tissues.*

tissues.

A treatment modality that is rapidly emerging is the radiation therapy making use of proton beams. The protons interact in a different way with the matter compared to photons. The energy loss of protons and charged particles in general, penetrating in matter, is proportional to the inverse square of their velocity. As a result the protons lose only a small fraction of their energy when they move in matter and lose most of their energy right before they stop. As a result a peak is observed in the energy loss which is known as the Bragg peak, figure 1.11.

The energy of the protons can be tuned so that the Bragg peak is localised in the tumour. As a result the dose delivered to the tumour can be maximised while the dose delivered at the normal tissue is limited only to a small fraction only before the tumour. Practically only a few protons can make it to after the tumour and therefore the normal tissue after the tumour is affected very little.

Proton radiography with GridPix

One of the basic challenges for the proton therapy is the localisation of the Bragg peak in the tumour with high accuracy. At the moment the position and the size of the tumour is determined with the conventional imaging techniques such as the Computed Tomography (CT), the Positron Emission Tomography (PET), Magnetic Resonance Imaging (MRI), etc. These techniques offer high resolution images, although uncertainties arise from the fact that the imaging and the treatment take

place at different locations. Therefore the exact position of the tumour is not known which can be crucial for the proton treatment planning.

An alternative approach to the conventional imaging techniques is to use the proton beam in order to create radiographs. This technique is called proton radiography and can be used for the precise determination of the proton stopping power, reducing the uncertainties in the treatment planning. The basic idea behind this technique is that the energy of the proton beam can be tuned in such a way that the Bragg peak is well outside the patient. The protons that enter in the tissue, will lose a fraction of their energy and scatter from their initial direction. The basic objective of the technique is determine the energy loss and the scattering angle of individual protons. The distributions of the energy loss and the scattering angle can be used in order to improve the quality of the treatment plan.

Due to its low mass and its precision the GridPix detector is an excellent candidate for proton radiography. The idea is to use GridPix detectors before and after the patient in order to determine the path of the protons and a calorimeter for the measurement of the residual energy. A small size prototype of a proton radiography setup has been developed by Nikhef in collaboration with KVI - Centre for Advanced Radiation Technology (KVI-CART) at Groningen. The setup was used in a proton beam at the KVI-CART facilities in order to perform the first proof of principle experiments, [34]. The results obtained are very promising, however further studies have to be performed.

For a realistic application the irradiation time of the patients should be as low as possible in order to minimise the uncertainties due to the movement of the patient. Therefore a large number of protons over short times are required for a high quality radiograph. At the moment, besides the well known issues of GridPix detectors, the readout speed is also a limiting factor.

1.7 Outlook and scope of the thesis.

The last missing piece of the Standard Model of particle physics seems to be in place after the observation of a new particle consistent with the Standard Model Higgs boson, independently by the ATLAS and the CMS experiments at the LHC. So far, there are no signs for deviation from the Standard Model hypothesis. Nevertheless, even if the picture is complete, there are still many remaining intriguing questions.

As a result, high energy physics enters in a new era focusing on the quest of new physics at the high energy frontier. The LHC with its rich physics programme along with the future facilities under consideration are ready to fulfil the expectations. Due to the increasing demands of the experiments there is a need for particle detectors which enable high precision measurements.

In this regard, the GridPix detector is a novel detector concept which combines the benefits of a pixel chip with an integrated gas amplification structure. The resulting unit is a detector sensitive to single electrons with a great potential for

particle tracking and energy loss measurements. So far, the experiments performed the past few years are the proof of concept for several applications in high energy and medical physics.

However, the Timepix[5] chips that were used for the proof-of-principle experiments were limiting the performance due to the slow front-end and the time-resolution. These limitations led to the design of new chips towards the final development of its successor, the Timepix3 chip. In addition, the reliability of the detectors for long term operation was under question due to the discharges occurring in the gas which might lead to breakdown. In the past, the technology used for the protection layer did not offer sufficient protection.

This thesis addresses these questions and is focusing on the development and characterisation of GridPix detectors based on the Timepix3 chip aiming to a design of a reliable GridPix detector for precision tracking applications in the future.

Chapter 2 introduces the physics of gaseous detectors, covering the interaction of radiation with matter and the energy loss mechanisms along with the charge transport and the multiplication in the gases. The gaseous detector concepts that are used for particle tracking are presented in chapter 3 beginning from the traditional gaseous chambers towards the development of the micro-pattern gaseous detectors and finally the GridPix detector.

In chapter 4 we present the results obtained with a GridPix detector based on a small scale prototype chip that was designed towards the development of the Timepix3. This was the first readout chip to implement a high-resolution time-to-digital converter (TDC) per pixel, which is expected to improve the position resolution along the drift direction. However the resolution is dominated by the timewalk effect. The author was involved in the preparation of the experiment, the installation and the data taking. Afterwards the author performed the analysis and extracted the results.

Chapter 5 concerns the development of a detector module based on the Timepix3 chip. The Timepix3 chip, thanks to the simultaneous measurement of the arrival time and the charge of the recorded signals enables the correction for the timewalk effect and is expected to improve further the performance. The personal contribution of the author concerns the construction of the detector, the data taking as well as the analysis presented in the chapter.

Finally, chapter 6 deals with the discharges in the GridPix detector. In order to study in a systematic way the resistive layers used for the protection against discharges, a dedicated setup has been developed. This chapter presents the results obtained from lab measurements and a testbeam in a hadron beam. The author was involved in the construction of the setup, the data taking and performed the analysis. The manuscript finishes with the summary.

[5]More information about the Timepix/Timepix3 chips can be found in the following chapters.

Chapter 2

Gaseous detectors' physics

"Nothing is more practical than a good theory."
— Ludwig Boltzmann

2.1 Introduction

The detection of a particle penetrating in matter requires its interaction with the basic constituents of the detection medium. Depending on the detection medium used, the properties of the incident particle and its energy several kind of interactions might take place. Each interaction makes the particle lose a fraction of its energy or change its direction.

This thesis is focusing on the development of detectors where a gas mixture is used as a detection medium. Particles passing through the gas interact with the gas molecules along their trajectory. The result of the interaction is that electrons are kicked out from the gas molecules in a process called ionisation. By applying an electric field the ionisation electrons are separated from the ions and drift to the anode electrode where an electric signal is formed.

In the first part of this chapter we briefly describe the energy loss mechanisms in the gas for charged particles and photons. Then we proceed with the description of the ionisation mechanisms followed by the transport of electrons and ions in the gas. Before we conclude we discuss the multiplication of electrons and several aspects which contribute to the choice of the gas mixture.

2.2 Cross section and mean free path

The probability of an interaction of a particle with the detection medium is quantified in terms of the cross section σ. The cross section is expressed in area units since sometimes it can be interpreted as the geometrical cross section. A commonly used unit in high energy physics is the barn (1 b = 10^{-28} m^2).

Often enough it is useful to relate the cross section with the mean distance that a particle can travel without encountering an interaction. This distance is known as the "mean free path" is given by equation 2.1:

$$\lambda = \frac{1}{n\sigma} . \tag{2.1}$$

where n is the electron density of the medium and σ is the cross section. Hence, for a detection medium with a given thickness l the expected mean number of interactions is l/λ which is Poisson distributed. For a more detailed discussion see [35,36].

2.3 Energy loss of charged particles

Fast charged particles traversing a gas detection medium lose energy mainly through ionisation and excitation processes. In this section we treat the energy loss mechanisms of charged particles by splitting them in two categories:

- Heavy charged particles with a mass $M >> m_e$ ($\mu^{\pm}$, $\pi^{\pm}$, p, etc.).
- Electrons (e^-) and positrons (e^+).

2.3.1 Heavy charged particles

Heavy charged particles lose energy due to electromagnetic interactions with the atomic electrons and the nuclei in the gas. Nuclear interaction processes can also occur. However, due to the short range of the strong force they are rare and as a result the contribution to the energy loss is minor compared to the atomic collisions.

The collision of a charged particle with a nucleus in the gas is an elastic scattering process where typically the particle is deflected at a small angle from its original trajectory. In the literature this process is referred as multiple Coulomb scattering and it is more dominant in dense media.

The inelastic collisions of the traversing particles with the atomic electrons is the major process contributing to the energy loss. During such collisions a fraction of the particle energy is transferred to the gas molecules. The impact of the transferred energy could be one of the following:

- **Excitation** of the atom: The transferred energy brings the atom to an excited state. After excitation the atom might return to a lower excited state or to its ground state or by emitting one or more photon(s) with a characteristic energy.
- **Ionisation** of the atom: In this case the transferred energy is enough to free an atomic electron which can move independently in the gas. Sporadically, such electrons are energetic enough to further ionise the gas and are referred to as δ-rays.
- **Molecular vibration**: The transferred energy enables a vibration mode of the gas molecule. This process is tricky for gaseous detectors since it is not contributing to the generation of the signal.

Additionally, there are other processes occurring which contribute to the energy loss. Charged particles might lose energy by emitting Bremsstrahlung, Cherenkov or Transition radiation. However these processes are beyond the scope of this thesis and are not discussed.

Energy loss due to ionisation

The theoretical description of the energy loss of heavy charged particles was given first by H. Bethe in 1930 [37] and later on corrected by F. Bloch [38]. The average energy loss is described by eq. 2.2 known as the "Bethe" formula, taken from [39]:

$$-\left(\frac{dE}{dx}\right) = Kz^2\frac{Z}{A}\frac{1}{\beta^2}\left[\frac{1}{2}\ln\frac{2m_ec^2\beta^2\gamma^2Q_{max}}{I^2} - \beta^2\right]. \tag{2.2}$$

The constant $K = 4\pi N_A r_e^2 m_e c^2$ where m_e is the electron mass, r_e is the classical electron radius and N_A is the Avogadro's number. Eq. 2.2 gives the average energy loss rate per unit path length of a particle with $\beta\gamma$[1], penetrating a gas medium where Z is the atomic number and A the atomic mass. The incident particle of mass M and charge z in electron units interacts with the medium. The maximum energy Q_{max} that can be transferred in a single collision is given by eq. 2.3:

$$Q_{max} = \frac{2\gamma^2 m_e V^2}{1 + 2\gamma m_e/M + m_e^2/M^2}. \tag{2.3}$$

The parameter I in eq. 2.2 is the mean excitation energy of the atom. This parameter is crucial for energy loss calculations. Its value is typically extracted from fitted data. Several tables of the mean excitation energy values for the elements can be found in [40–42]. For compound and mixtures the mean excitation energy is calculated by approximation methods. For more information see [36,43].

[1] β is the ratio of the particle velocity over the speed of light and γ is the relatvistic lorentz factor given by $\gamma = 1/\sqrt{1-\beta^2}$. For a particle with a momentum p and mass M, $\beta\gamma = p/Mc$.

Eq. 2.2 gives the average rate of energy loss or the mass stopping power in MeV per unit path length in g/cm^2 which depends primarily to the velocity and the charge of the particle and slightly on the density of the medium. For intermediate energies (below 200 MeV) the energy loss shows a strong dependance $1/\beta^2$, it decreases with increasing momentum and eventually reaches a minimum. Above this point it increases again with a logarithmic rise.

For lower energies the velocity of the particle is comparable to the velocity of the outer atomic electrons. As a result the Bethe formula fails to describe the energy loss. Additive shell corrections [44] have to be used in order get an adequate description. For higher energies the polarisation density of the medium has to be taken into account, [45]. Due to this "density effect" the expected energy loss reaches a plateau ("Fermi plateau"). The density effect is essential for dense media. For gases under normal pressure and intermediate energies, it can be neglected.

Figure 2.1 shows the energy loss rate for muons in commonly used gases for intermediate energies.

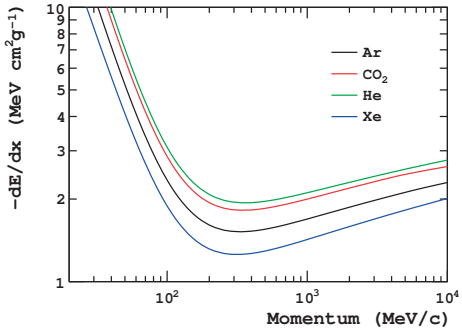

Figure 2.1: *Average energy loss rate of muons in gases commonly used in particle detectors. Radiative effects are not included. For increasing momenta up to 200 MeV the energy loss decreases and reaches the minimum at about 250 MeV. Particles at this point are considered as minimum ionising particles (MIPs). As shown in the figure this point is independent of the medium. Data are taken from* [46].

Mean range

The range is the distance which the particle can travel in a medium before it loses its energy and stops. A heavy charged particle traversing matter loses energy continuously which depends on the type of the medium and the energy of the particle. The energy loss is a statistical phenomenon and as a result not constant. This means that the range of identical particles with the same energy is a statistical distribution

around a mean value. The mean value of the range can be calculated by integrating eq. 2.2:

$$\textit{Mean Range} = R = \int_{E_0}^{0} \left(\frac{dE}{dx}\right)^{-1} dE\,. \tag{2.4}$$

Eq. 2.4 gives an approximation of the mean range of a heavy charged particle and it does not take into account the multiple Coulomb scattering which could be essential for dense media. However for heavy charged particles in a gas medium the multiple scattering is minimal which makes the particles travel on a straight line. As a result the range is approximately equal to the path of the particle. The ratio R/M of the incident particle is a function its momentum. Figure 2.2 shows the ratio R/M for muons in various gases as a function of their momentum. For a more detailed discussion see [36].

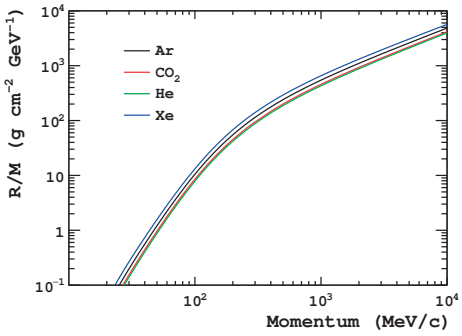

Figure 2.2: *The ratio R/M as a function of the momentum for muons in gases commonly used in particle detectors. Data are taken from* [46].

2.3.2 Electrons and positrons

The interaction of electrons (e^-) and positrons (e^+) are treated together in this section. However their final destination differs. The positrons, when they lose their energy and approach an electron, initiate the electron-position annihilation process which leads to the production of two photons with the same energy in opposite directions. On the other hand, electrons after losing their energy, become atomic electrons due to the absence of positrons in matter. Nevertheless, the term "energy loss of electrons" refers to the energy loss of both electrons and positrons.

Energy loss of electrons

Like the heavy charged particles, the electrons lose energy due to inelastic collisions with the atomic electrons and the nuclei. Hence, electrons lose energy mainly due

to ionisation and excitation processes. During these processes the electrons might lose a large fraction of their energy or even their whole energy and stop. Due to the their small mass, they suffer from multiple scattering. As a result the electrons are deflected from their initial trajectory and their total path is far from straight. Throughout an ionisation process it is also possible that the knock-on electron possess enough energy to cause further ionisation. These high energetic electrons are known as δ-rays.

Additional to the ionisations and excitations, electrons lose energy by emission of Bremsstrahlung radiation. Bremsstrahlung is electromagnetic radiation emitted when a charged particle is decelerated in the Coulomb field during an inelastic collision. The incident particle then loses a part of its energy, which is converted into a photon because energy is conserved. The effect is more present at higher energies. In general it is larger for electrons due to their small mass compared to heavy charged particles where the effects are negligible.

The total energy loss of electrons per unit length is the sum of the energy loss due to ionisation and excitation and the energy loss due to Bremsstrahlung:

$$\left(\frac{dE}{dx}\right)_{total} = \left(\frac{dE}{dx}\right)_{ion} + \left(\frac{dE}{dx}\right)_{Brem} . \tag{2.5}$$

Figure 2.3 shows the total energy loss of electrons in argon as a function of their energy.

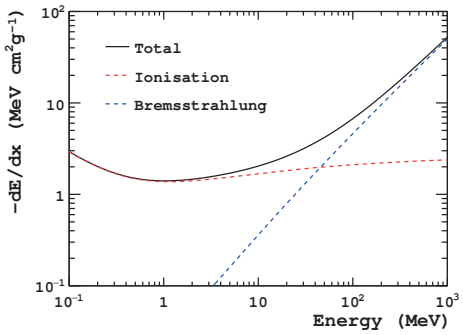

Figure 2.3: *Total energy loss rate of electrons in argon gas as a function of the energy. The energy loss due to ionisation and excitation is more dominant at low energies due to the dependance on the inverse square of the velocity β. For high energies the energy loss due to Bremsstrahlung increases with the energy of the particles. Data are taken from* [47].

The energy in which the energy loss due to ionisation is equal to the energy loss due to Bremsstrahlung radiation is known as "Critical Energy" and depends mainly on the type of the material. According to [39], an accurate approximation for the

calculation of the critical energy for gases is given by eq. 2.6:

$$E_{cr}^{gas} = \frac{710(MeV)}{Z + 0.92} \,. \tag{2.6}$$

Range

The definition of the range of electrons is not straightforward due to the multiple scattering which deflects the electrons from their original path. As a result for the calculation of the range the integration of the Bethe formula is not sufficient. However, approximations are feasible by using empirical formulae. Figure 2.4 show the range of electrons in various gases calculated using as continuous-slowing-down approximation (CSDA).

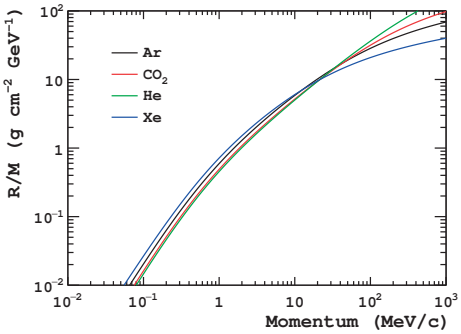

Figure 2.4: *The ratio R/M as a function of the momentum for electrons in gases commonly used in particle detectots. The calculation is performed assuming the continuous-slowing-down of the electrons* (CDSA). *Data are taken from* [47].

2.3.3 Fluctuations to energy loss

The Bethe-Bloch formula calculates the average energy loss for a charged particle with a given energy. However due to the statistical nature of the interactions, the energy loss per collision fluctuates around a mean value. The theoretical description is a complicated mathematical problem and depends on the medium. However it is easier to study separately thick and thin media.

For particles traversing thick media typically a large number of interactions occur. Thanks to the Central Limit Theorem[2] (CLT) it can be derived that the energy loss is gaussian distributed around a mean value.

[2]Suppose n independent random variables following the same distribution. The average of the variables as $n \to \infty$ follows a Gaussian distribution.

On the other hand, for particles transversing thin media the number of collisions is not as large as the CLT would require. As a result the distribution of the energy loss is asymmetric. The theoretical description was given by L. Landau in [48] and generalised by P.V. Vavilov in [49].

The "Landau-Vavilov" theory the energy loss is parametrised by the most probable energy loss during a collision where the maximum energy transfer is given by Q_{max}. An example distribution is shown in figure 2.5. In some cases of thin absorbers the Landau distribution fails to describe the energy since the width of the energy loss broadens [50].

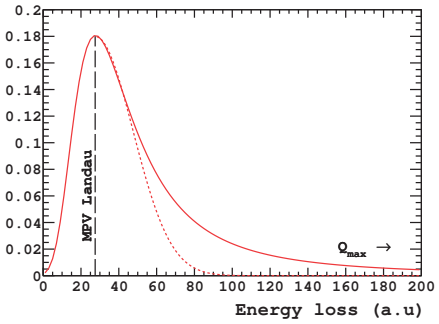

Figure 2.5: *An example Landau distribution which describes the energy loss of a charged particle in thin absorbers. The distribution is strongly asymmetric and presents a long tail as the energy loss approaches the maximum energy tranfer Q_{max} during a collision. In comparison the dotted line represents a gaussian tail. The parametrisation is done according to the most probable value.*

In general the discussion of the energy loss and its fluctuations in particle detectors is a tricky problem. A particle detector is measuring the energy deposition in its active volume. However, the deposited energy in the detector is not always the energy loss of the traversing particle, since the detectors are not able to observe fluctuations of the energy loss. This happens for example when a δ-ray produced is energetic enough to escape the active volume. As a result there is only a partial deposition of energy measured by the detector. The δ-rays of a kinetic energy Q_e and momentum p_e are produced at an angle θ given by

$$\cos\theta = \left(\frac{Q_e}{p_e}\right)\left(\frac{p_{max}}{Q_{max}}\right), \tag{2.7}$$

where p_{max} is the momentum of an electron with the maximum possible energy transfer Q_{max}. Figure 2.6 shows a δ-ray produced from a high energetic muon.

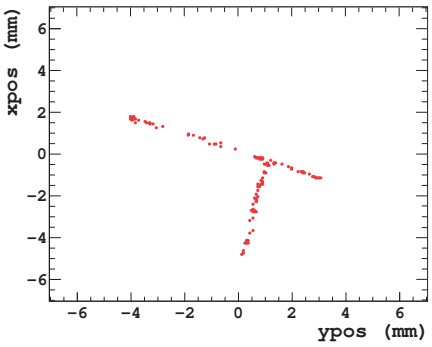

Figure 2.6: *A δ-ray produced from a muon (entering on the left) with a momentum of* 180 MeV/*c. The event was recorded with a gaseous pixel detector filled with* CO_2/DME *mixture.*

2.3.4 Multiple scattering

Charged particles crossing a medium can be deflected due to the Coulomb potential of nuclei and the atomic electrons. This effect is called multiple Coulomb scattering and is mainly caused by collisions with the nuclei. The scatters lead to declinations at small angles from the original path of the particle, see figure 2.7.

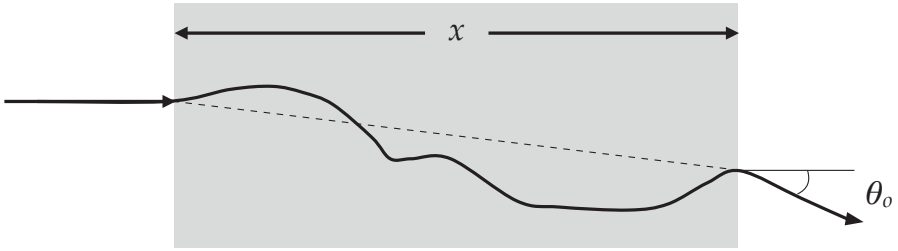

Figure 2.7: *A simplified sketch showing the effect of the multiple Coulomb scattering on the path of a charged particle.*

The theory of multiple scattering was introduced by Molière [51]. Taking into account small scattering angles, their distribution is a gaussian with a mean value of $\theta = 0$ and width given by eq. 2.8:

$$\theta_0 = \frac{13.6MeV}{\beta cp} z \sqrt{\frac{x}{X_0}} \left[1 + 0.038 \ln\left(\frac{x}{X_0} \right) \right], \tag{2.8}$$

where p is the momentum, β the velocity and z the charge of the incident particle. The thickness of the scattering medium is expressed in terms of the radiation length x/X_0. The radiation length is a characteristic of the medium and is defined as a) the mean distance over which a high-energetic electrons loses all but $1/e$ of its energy due to Bremsstrahlung radiation or b) the 7/9 of the mean free path for pair production (described in the next section) by a high-energy photon.

2.4 Energy loss of photons

The interaction of photons with matter is rather different than the interactions of charged particles. During an interaction, a photon either is absorbed by the medium or deflected at large angles. Photons interact with matter with one of the following processes. Each process shows a different dependence on the energy of the incident photon and the medium.

- **Photoelectric effect:**

  The effect occurs at low energies when the energy $E_\gamma = hf$ of an incident photon with frequency f is absorbed by an atomic electron. The effect occurs if the photon energy is larger than the binding energy of the electron Φ. In this case, the electron is ejected from the atom with a kinetic energy $E_{kin} = hf - \Phi$. The photoelectric effect generates secondary processes like the characteristic X-ray fluorescence and the Auger effect [52].

- **Compton Scattering:**

  Compton scattering occurs for energies approaching the rest mass of the electron and describes the scattering of a photon by an atomic electron. The photon is scattered from its original direction and a fraction of its energy is transferred to the recoil electron which, after the scattering, is moving to a different direction. The probability for the scattering to occur is independent of the atomic number of the medium.

- **Pair production:**

  The pair production effect is the conversion of a photon into an electron - positron pair. The effect occurs under the presence of the Coulomb field of the nucleus if the energy of the photon is at least twice the rest mass of the electron i.e. $E_\gamma \geq 1.022$ MeV. The probability of the pair production effect depends on the energy of the photon and the atomic number of the medium. Generally, the pair production effect occurs at high energies. After the pair production, the positron loses its energy, attracts an electron and annihilates into two photons each with an energy of 0.511 MeV. At high energies, the

positron loses its energy through ionisation and Bremsstrahlung radiation processes until its energy is low enough for the annihilation to occur.

- **Rayleigh scattering:**

  Rayleigh (or coherent) scattering is the elastic scattering of a photon from an atom. Since there is no energy transfer, the atom remains at the same state, while the photon continues on a different direction. This process is negligible for high energies.

Photon attenuation

The attenuation of a photon beam in matter is given by eq. 2.9:

$$I = I_o \cdot e^{-\mu x}\,, \tag{2.9}$$

where $\mu = N \cdot \sigma = \frac{1}{\lambda}$ is the mass attenuation coefficient of photons, I_o the incident intensity of the beam, σ the total cross section per atom, N the atom density and λ is the mean free path in the absorber material.

For photons, the total cross section per atom is the sum of the cross sections of the aforementioned processes:

$$\sigma = \sigma_{photoelectric} + \sigma_{compton} + \sigma_{pair} + \sigma_{rayleigh}\,. \tag{2.10}$$

Figure 2.8 shows the total cross section of photons in argon.

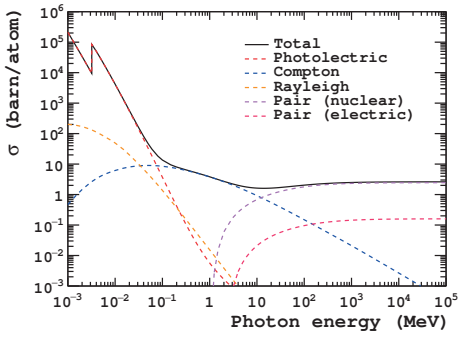

Figure 2.8: *The total photon absorption cross section for argon gas. The photoelectric effect occurs at low energies, while at intermediate energies the Compton effect dominates. At high energies, greater than 1.022 MeV, the pair production becomes dominant. Data are taken from* [53].

2.5 Charge transport in the gas

The working principle of gaseous detectors is based on the collection of the charge that is created by ionisation. The electrons and ions that are created in ionisation processes, under the presence of an electric field, move in the gas and interact further with the gas molecules. This section describes the charge transport in the gases which is essential for the particle detectors.

2.5.1 Ionisation processes

The previous sections describe the energy loss of particles penetrating a gas medium. The electrons and ions that are produced during these processes are called primary ionisation. However a large fraction of the charge along the path of the incident particle is generated by the secondary ionisation.

The secondary ionisation processes arise from the ionisation electrons. The knock-on electrons may have sufficient energy (i.e. δ-rays) in order to further ionise the gas. As long as their energy is larger than the ionisation potential of the medium, ionisation occurs and eventually they lose their energy and approach thermal equilibrium. The cross sections of ionisation electrons interacting with gases can be found in the literature [54,55].

Additional ionisation occurs due to excited states of the gas atoms. Due to a prior interaction with particles these atoms might move to one of their excited states. If the energy of this metastable state is larger that the ionisation energy, then secondary ionisation is possible to occur. This effect introduced by F.M. Penning [56] occurs in compound gas mixtures where atoms of two types are present or between atoms of the same type.

Figure 2.9 shows the cross section of electrons moving in argon and carbon dioxide gases. Elastic scattering processes dominate for low energies while ionisation takes over for high energies. The cross section in argon shows local minima and maxima due to the Ramsauer effect [57]. It is an effect explained by quantum mechanics and describes a drop at the cross section of slow-moving electrons in noble gases. The drop is observed when the wavelength of the incident electron wave function is comparable to the atomic size.

Besides the ionisation processes that are responsible for the creation of the electron and ion pairs, there are processes working to the opposite direction. Electronegative molecules like O_2, CO_2, H_2O, etc. tend to attract electrons and form negative ions. This process is called electron attachment. Additionally, the electron-ion pairs might recombine. Those two processes reduce the amount of ionisation produced and therefore affect the performance of the detector.

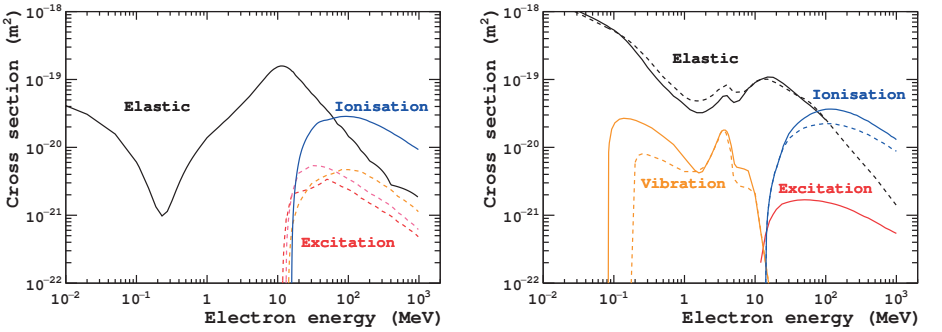

Figure 2.9: *The cross section for electrons for selected processes in argon (on the left) and in carbon dioxide (on the right) as a function of the kinetic energy. The data obtained from* [55].

2.5.2 Drift

The electrons and the ions created during the primary ionisation are accelerated and drift along the lines of the applied electric field. The motion is hindered by collisions with the gas molecules which randomise the motion. In order to describe the drift properties we assume an average "drift velocity" which is smaller than the velocity between consecutive collisions.

For a particle moving in a gas under the influence of an electromagnetic field the equation of motion is given by eq. 2.11:

$$m\frac{d\vec{v}}{dt} + \eta(t) = e\vec{E} + e \cdot \vec{v} \times \vec{B}\,, \tag{2.11}$$

where m is mass, e the charge of the particle and $\eta(t) = -m\vec{v}/\tau$ is a stochastic term introduced by P. Langevin [58] due to the Brownian motion of the particle where τ represents the average time between two collisions. Assuming, $\vec{E} \perp \vec{B}$, $t >> \tau$ and a constant electric field, the drift velocity v_d is given by eq. 2.12:

$$v_d = \mu \frac{E}{\sqrt{1 + \tan\theta_L}}\,, \tag{2.12}$$

where μ is the mobility of the particle and θ_L is the Lorentz angle i.e the angle between the drift direction and the electric field. For detailed calculations see [35,59]. For the case where there is no magnetic field the drift velocity is given by eq. 2.13,

$$v_d = \mu E = \frac{qE}{m}\tau\,. \tag{2.13}$$

Eq. 2.13 gives a generic expression of the drift velocity. For a derivation of the drift velocity of electrons and ions in gases one has to approach the problem at the

microscopic level. For example, drifting electrons collide with the gas molecules. The average time τ between two collisions is related to the molecule density n, the cross section σ of the process under consideration and the velocity υ of the electron between two consecutive collisions,

$$\frac{1}{\tau} = n\,\sigma(\epsilon)\,\upsilon(\epsilon)\,. \tag{2.14}$$

In eq. 2.14, the cross section and the velocity are a function of the energy ϵ of the electron which is the sum of its thermal energy and its kinetic energy due to the acceleration in the electric field. The electron energy ϵ also depends strongly on the energy transfer per collision.

Increased values for the drift velocity can be obtained if the electron energy remains at low levels where elastic scattering mostly occurs. For noble gases, large drift velocities are obtained due to the low cross section thanks to the Ramsauer minimum. However, due to the absence of vibrational modes the electron energy tends to increase and exceed the ionisation and excitation potentials. As a result, the cross section increases and therefore the drift velocity is lower.

Molecular gases, due to the vibrational modes usually maintain the electron energy at lower levels. Gases that preserve the average electron energy at low levels are know as "cold" gases. On the contrary hot gases are the gases where the average electron energy is high. By mixing the noble gas with a small amount of a molecular gas the drift velocity increases significantly.

Figure 2.10 shows a comparison of the drift velocity of electrons for the gases used in the context of this thesis. The $Ar/CF_4/iC_4H_{10}$ gas mixture shows increased drift velocity compared to pure argon gas due to the molecular additives, which is maximised due to the Ramsauer effect. The CO_2/DME is a molecular cold gas mixture with a low drift velocity capable for high precision tracking measurements.

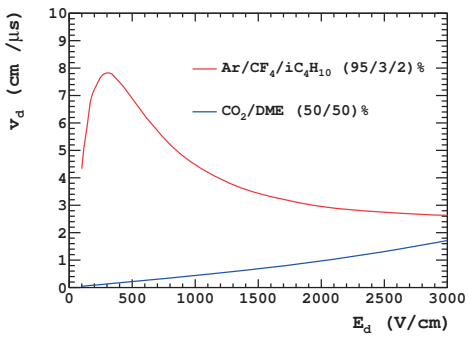

Figure 2.10: *The drift velocity as a function of the electric field for the gas mixtures used in this thesis. The data are obtained from simulations performed with the computer program Garfield* [60].

The ions produced during the primary ionisation drift towards the cathode. Due to the their large mass, their motion is not as random as the electron motion and up to a good approximation the ions follow the electric field lines. The drift properties of ions are discussed in detail in [35]. The "back-flow" of ions in the drift area gives rise to space charge effects which might distort the electric field locally. This can alter the detector performance especially at high particle rates. More details about the ion back-flow in GridPix detectors can be found in [61].

2.5.3 Diffusion

The previous section describes the drift of electrons in gases. Due to collisions with the gas molecules the drifting electrons are deflected and follow a random path. Let us consider a point-like cloud of electrons with density n_0, which begins at time $t = 0$ and drifts along the electric field direction. Assuming that the electric current is conserved, it can be derived that after time t the electron density $n(t)$ follows a gaussian distribution which spreads to all directions

$$n(t) = \frac{n_0}{e(4\pi D_T^c)(4\pi D_L^c)^{1/2}} \exp\left[-\frac{(x^2+y^2)}{4D_T^c t}\right] \exp\left[-\frac{(z+v_d t)^2}{4D_L^c t}\right]. \tag{2.15}$$

Eq. 2.15 denotes that the electric field points to the opposite direction of the drift, where D_T^c, D_L^c are the diffusion constants in the transverse and longitudinal direction. For a given drift velocity v_d and an electric field E the transverse and longitudinal diffusion is given by eq. 2.16, 2.17,

$$D_T = \sqrt{\frac{2D_T^c}{v_d}}, \tag{2.16}$$

$$D_L = \sqrt{\frac{2D_L^c}{v_d}}. \tag{2.17}$$

The diffusion coefficients are often expressed as the gaussian spread of the diffusion on the transverse and longitudinal direction over a drift distance l_d in units of $\mathrm{mm}/\sqrt{\mathrm{mm}}$.

$$D_T = \sigma_T / \sqrt{l_d}, \tag{2.18}$$

$$D_L = \sigma_L / \sqrt{l_d}. \tag{2.19}$$

Eq. 2.18, 2.19 give the contribution of the diffusion to the error of the position measured by the detector. Therefore the diffusion has a strong impact on the detector position resolution. In order to minimise the diffusion and improve the precision on the measurement of the position cold gases like CO_2/DME can be used. Figure 5.46 shows diffusion coefficients as a function of the electric field for the gases used in this thesis.

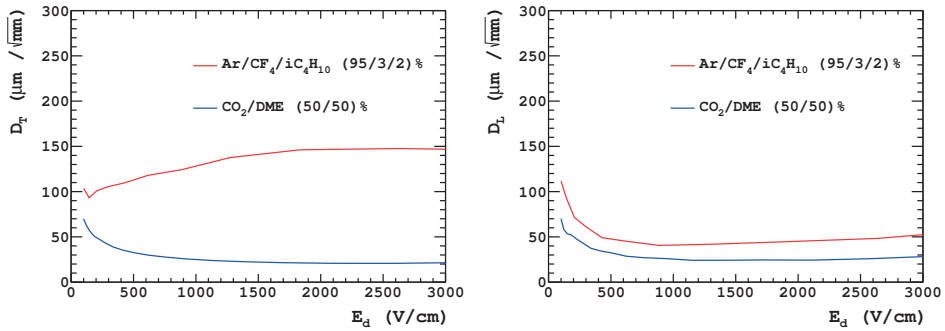

Figure 2.11: *The diffusion coefficients for the transverse (on the left) and the longitudinal (on the right) direction for the gas mixtures used in this thesis. The data are obtained from simulations performed with the computer program Garfield* [60].

2.6 Multiplication of electrons

In gaseous detectors the primary ionisation takes place in the drift region where a moderate electric field is applied. Under the influence of the electric field, the electrons drift towards the anode electrode. Close to the anode the electric field is much stronger. As a result the electrons are accelerated by the electric field and their energy exceeds the ionisation potential of the atoms or molecules.

The increased electron energy leads to the further ionisation and therefore the electron multiplication since for every ionisation an extra electron is obtained. As the electrons drift to the anode, the multiplication takes the form of an avalanche (figure 2.12) and the number of electrons grows till the electrons reach the anode.

2.6.1 Townsend coefficient

The multiplication of electrons can be described by the first Townsend coefficient α. If λ is the mean free path for an ionisation, i.e the average distance which an electron can travel without engaging in an ionisation, then the first Townsend coefficient is its inverse

$$\alpha = \frac{1}{\lambda} = N\sigma_{ion}\,. \tag{2.20}$$

The first Townsend coefficient is the probability of an ionisation per unit path length and is related to the ionisation cross section and the electron energy. In eq. 2.20, N is the number of gas atoms or molecules per unit volume.

Let us consider n electrons in an avalanche. The number of electrons created in

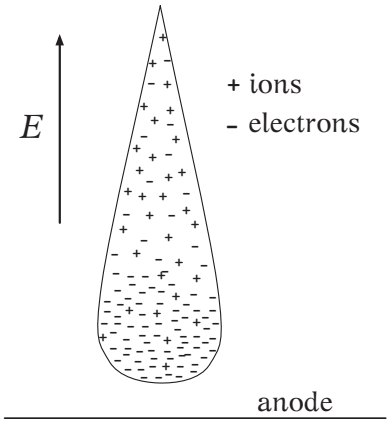

Figure 2.12: *An artistic impression of the formation of an electron avalanche. Under the influence of the electric field the electrons are pushed to the "head" of the avalanche and the ions to its tail.*

the avalanche after a drift path dl_d would be

$$dn = n_0 \, \alpha \, dl_d \, . \tag{2.21}$$

By integrating eq. 2.21 we derive the total number of electrons that were created over a drift distance l_d:

$$n = n_0 e^{\alpha l_d} \, , \tag{2.22}$$

such that

$$G = \frac{n}{n_0} = e^{\alpha l_d} \, . \tag{2.23}$$

The equations above are valid for a given value of a uniform electric field E. In eq. 2.23, the ratio of the total number of electrons n created over the number of electrons before the multiplication n_0 defines the multiplication factor G well known as "gas gain".

2.6.2 Gain fluctuations

The gas gain represents the average number of electrons $\bar{n}$ created from a single primary electron. Besides the local variations [35] due to mechanical imperfections, the electric field uniformity, environmental settings, etc. the number $\bar{n}$ is subject to large statistical fluctuations.

For a given value of the first Townsend coefficient α, the probability to have n electrons created [62] after a drift path l_d is

$$P(n,\, l_d) = e^{\alpha l_d}\left(1 - e^{\alpha l_d}\right)^{n-1} . \tag{2.24}$$

Eq. 2.24, for $\bar{n} = e^{\alpha l_d}$ becomes

$$P(n,\, l_d) = \frac{1}{\bar{n}}\left(1 - \frac{1}{\bar{n}}\right)^{n-1} \approx \frac{1}{\bar{n}} \exp\left(-\frac{n}{\bar{n}}\right). \tag{2.25}$$

For large values of $\bar{n}$ the approximation in eq. 2.25 was introduced by H.M. Furry in [63]. In this model, the probability distribution seems to depend only on $\bar{n}$ and not explicitly on the drift distance, which suggests that typically the avalanche has the same shape. The mean and the standard deviation of the distribution are equal to the average size of the avalanche $\bar{n}$. However this approximation is valid only for moderate electric fields. Experimentally it has been shown by J. Byrne in [64] that for high electric fields the single electron avalanche distribution evolves from an exponential into a peaked shape distribution.

A phenomenological peaked shape distribution frequently used to described the gas gain known as the Polya distribution is given by eq. 2.26

$$P(n,\theta) = \frac{1}{\bar{n}}\frac{(\theta+1)^{\theta+1}}{\Gamma(\theta+1)}\left(\frac{n}{\bar{n}}\right)^{\theta} \exp\left(-\frac{(\theta+1)n}{\bar{n}}\right), \tag{2.26}$$

where the variance is given by $\sigma^2 = \bar{n}^2/(\theta+1)$. Figure 2.13 show the Polya distribution for various values of θ.

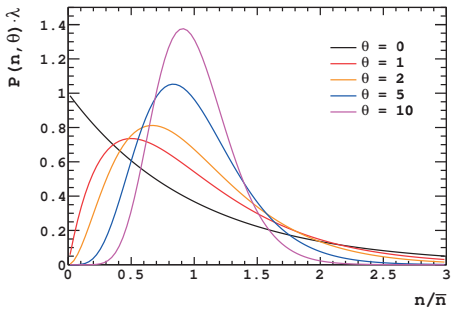

Figure 2.13: *The Polya distribution of various values of the parameter θ. The Polya distribution for $\theta = 0$ is an exponential distribution. As the value of θ increases, it evolves to a peaked shaped distribution and for high values of θ becomes a gaussian distribution.*

2.6.3 Streamer formation - Discharges

In gaseous detectors, the amplification of the charge created in the primary ionisation through the avalanche process is a basic requirement. Typically the gaseous detectors are operated in a gas gain of several thousands. In order to achieve such numbers high electric fields are required. There is a physical limit though, which constraints the maximum gain that can be achieved.

For high values of the gas gain, besides the electrons also photons contribute to the development of the avalanche. As a result there is a lateral spread of the charge in the active gas volume. This lead to an increased amount of ionisation and therefore to a raise of the space charge locally.

The natural consequence of the enlarged space charge is a local electric field deformation, figure 2.14a. Under the influence of the distorted electric field, photo-electrons from the surrounding area move in the avalanche and initiate secondary avalanches, 2.14b, 2.14c.

The propagation of the charge along the longitudinal direction pushes the avalanche beyond the proportional region and evolves to a narrow plasma streamer, 2.14d. Eventually the streamer will reaches two electrodes of the detector which are now in contact.

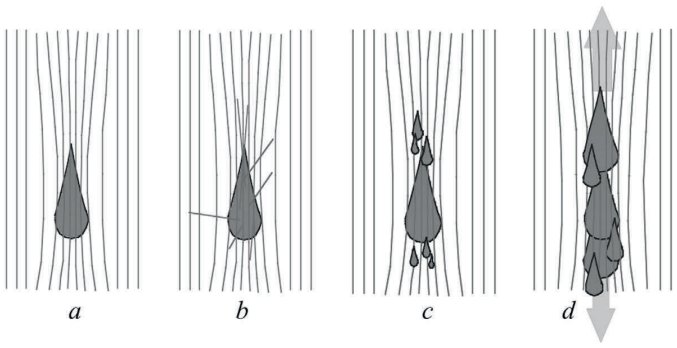

Figure 2.14: *An illustration of the streamer formation which leads to a discharge. The picture is taken from* [62]. *For a detailed description from left to right see the text.*

The process of the steamer formation which leads to discharges is shown in figure 2.14. This process was studied by H. Raether [65] who set an empirical limit on the size of the avalanche $\bar{n} < 10^8$, above which the transition of an avalanche evolves to a streamer. By using this number in eq. 2.23 we extract $\alpha\, l_d < 20$ which is an alternate expression for Raether's limit.

2.7 Gas mixture

Gaseous detectors have been used extensively in a wide range of applications and experiments in the past and are under consideration for use in the future. Depending on the application, the composition of the gas mixture varies and there are several aspects that one has to take into account for the choice of the gas mixture. In this section we briefly discuss the main characteristics which play an important role to this choice.

Drift velocity and diffusion

The drift velocity and the diffusion are two basic parameters for the choice of the gas mixture. Both drift velocity and diffusion have a strong dependence on the electric field and the electron energy. The choice of mixture however is a compromise between precision and fast charge collection time. With a large drift velocity better timing can be achieved due to the fast charge collection. In this case, the diffusion is larger and therefore the position measurement is less accurate. On the other hand, high precision position measurements require low diffusion which makes the charge collection time slower due to the low drift velocity. As we will discuss later, the low diffusion also improves the precision of the measurement when a time-to-digital converter (TDC) is used to reconstruct the creation position of ionisation electrons.

For noble gas based gas mixtures by taking advantage of the Ramsauer effect, a maximum drift velocity can be achieved for low electric fields. For low fields however the diffusion is large. An increase of the electric field would reduce the diffusion but it has a drawback for hot gases as we discussed in subsection 2.5.2.

On the contrary, molecular cold gases do not face this problem. For the same electric field strength the drift velocity is lower, though the diffusion is much lower which improves the position resolution. Such a gas mixture is composed by CO_2 and DME. For the precision measurements in this thesis we make use of this gas mixture. For an electric field of 1 kV/cm figure 2.10 gives about 5 cm/μs for the drift velocity and figure 5.46 25 $\mu m/\sqrt{mm}$ for the transverse and longitudinal diffusion.

Gain

The gas gain, taking into account that a sufficient amount of ionisation is produced, is strongly related to the electric field strength and it is a property of the gas mixture. The multiplication factor is an important parameter for the working point of a gaseous detector. Due to the gain fluctuations, in order to have clean signals above the noise level there is a requirement for sufficient gain. A typical range of gain that can be achieved with gaseous detectors operating at normal temperature and pressure is $10^3 - 10^5$ electrons.

High values for the gain however, have a drawback. As the gas gain is getting higher, the probability of a streamer formation leading to a spark is increased. This

has a major impact on the reliability of the detector. An additional parameter to take into account for the gas gain is the composition of the gas mixture. A sufficient value for the gain can be achieved with several gases. Nevertheless, for each gas the detector has to be operated in a different setting. For example, a molecular mixture like CO_2/DME compared to an argon based mixture, requires twice the strength of electric field in order to achieve the same average gain.

Electron attachment

The electron attachment is an important parameter of the gas mixture which strongly affects the efficiency of the detector. As we discussed in subsection 2.5.1, the drifting ionisation electrons might attach to electronegative molecules like O_2, CO_2, H_2O. As a consequence these electrons do not contribute to the avalanche development. Therefore they can not be detected and the efficiency of the detector drops.

The choice of the mixture with regard to the attachment depends also on the size of the active volume. For example, in a large area time projection chambers where the drift distances reach up to O(1m) a CO_2/DME would be insufficient due to electron attachment.

Ageing

Gaseous detectors in use for long periods show a deterioration in their performance due to irradiation know as "ageing". The ageing is influenced by the materials used for the detector construction and strongly depends on the gas mixture. The main mechanism responsible for the ageing is the formation of polymers during the avalanche. These impurities show excellent adhesion to surfaces and might attach to the detector electrodes. This could lead to a degradation of the gas gain, reduced efficiency and resolution, self-sustained currents leading to discharges, etc.

The composition of the mixture is essential for the ageing. For example the use of carbohydrates in the mixture accelerates the ageing. In order to restore aged detectors, small quantities of O_2, H_2O or a solvent can be added to the gas mixture. The additives can reduce the polymerisation rate and prevent the ageing process. However in some cases the impurities are resistant to chemicals and solvents.

Chapter 3

Gaseous detectors for tracking

"I've worked on many detectors, some were very elegant and useless, and didn't have a Nobel Prize, so this one was not the most elegant, but it was useful."
— Georges Charpak

3.1 Introduction

Beginning from the early years and the discovery of x-rays by Röntgen in 1895, people where experimenting with radiation and its detection techniques. A few years later, J.J. Thomson with his famous experiment about cathode rays [2] concluded to the existence of the electron. The discovery of electrons, gave a huge boost to the studies of radiation both at the theoretical and experimental level.

Soon enough it was realised that gases can be used as a detection medium for radiation. Charged particles transversing the gas are generating electron-ion pairs. Thanks to the high transportability of electron and ions in gases, the charge created by the ionisation can be collected. In 1912, C.T.R. Wilson invented the first ionisation chamber able to visualise the tracks of charged particles [66].

During the first half of the 20^{th} century, thanks to the cloud chamber and the "Geiger-Müller" tube [67], significant progress has been made in the counting and tracking of charged particles. Later on, the next generation of ionisation chambers was introduced by D.A Glaser with the famous "Bubble Chamber" [68].

However the groundbreaking advance in the field of ionisation chambers came in 1968 with the invention of the multi-wire proportional chamber (MWPC) by G. Charpak [69]. The MWPC revolutionised the way that particles are localised and has been used extensively in particle physics experiments leading to many discoveries.

The success of the MWPC stimulated the realisation and the development of the drift chamber [70] and later on the time projection chamber [71]. These devices brought a significant advance in the field of experimental particle physics. However with the increasing demands of the experiments they also showed limitations. In order to overcome such limitations the development of the Micro-pattern gas detectors was realised. This chapter gives a brief overview of the gaseous detectors used for particle tracking.

3.2 Traditional ionisation chambers

3.2.1 Wire chamber

The wire chamber is a device with a quite simple geometry. It consists of a metallic tube of radius R filled with gas. In the centre of the tube there is a thin metallic wire of radius r_w. The geometry of the chamber is shown in figure 3.1.

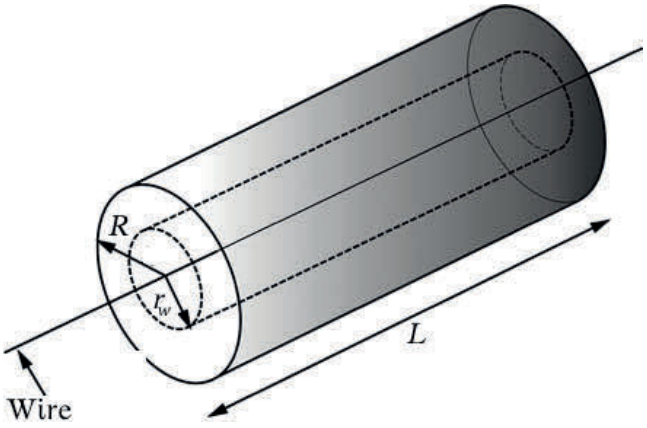

Figure 3.1: *An illustration of the wire tube geometry. Picture is taken from* [72].

A positive high voltage V_0 is applied on the wire while the tube acting as cathode is at ground potential which results in an electric field between the cathode and the anode. The electric field strength at a distance r from the centre of the wire is given by eq. 3.1 and can be derived by using Gauss' theorem, assuming a cylinder with length $L >> R$,

$$E = \frac{V_0}{ln(R/r_w)} \frac{1}{r} . \tag{3.1}$$

Since the tube is filled with a gas, traversing particles create electron-ion pairs. Under the influence of the electric field, the electron and ions drift towards the anode and cathode respectively. When the electrons reach close to the wire where

the electric field is strong enough, they acquire enough energy in order to initiate an avalanche process which is collected at the anode forming the signal.

The amplitude of the signal depends on the gas used, the type of the incident particle and the electric field strength. Depending on the voltage V_0 that is applied on the wire, the chamber can be operated in various modes. Figure 3.19 shows the collected charge as a function of the applied voltage at the wire. The operation mode of the wire tube can be distinguished in the following regions:

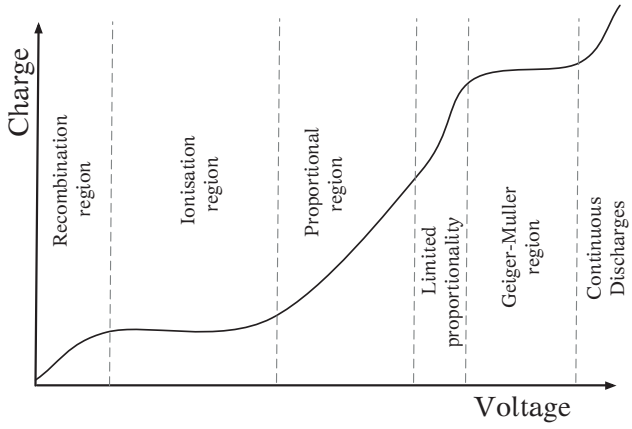

Figure 3.2: *The various operation modes of a wire chamber. For more details about each mode see the text.*

- **Recombination region:** The voltage is too low and therefore the electric field too weak in order to accelerate the ions. Hence, the recombination effects are counter-acting the ionisation.
- **Ionisation region:** The voltage is sufficient for the separation of electrons and ions. The primary electrons created at the ionisation are collected by the anode. The signal amplitude depends on the type and the energy of the incident particle. The chamber is identified as ionisation chamber.
- **Proportional region:** The primary electrons gain enough energy due to the acceleration by the electric field in order to ionise further and initiate avalanche processes. In this region the amplitude of the signal depends on the amount of primary ionisation. Since the amount of primary ionisation depends on the type of the particle, the chamber can be used for energy loss measurements. A detector operation in this regime is know as a proportional chamber.
- **Limited proportionality region:** In this region, the secondary ionisation is high enough and space charge effects start to dominate. As a result the signal amplitude increases with the voltage and the proportionality is limited.

- **Geiger-Müller region**: The proportionality is lost and the signal amplitude is independent of the voltage. No matter the type of particle, huge avalanches are recorded and the chamber can be used only for counting. A detector operating in this domain is known as a Geiger-Müller counter.
- **Discharge region**: The size of the avalanche exceeds Raether's limit and therefore the transition of the avalanche to a streamer takes place.

3.2.2 Multi-wire proportional chamber (MWPC)

The multi-wire proportional chamber consists of two parallel plate cathode planes at a distances $y = \pm L/2$. In between the cathode planes at $y = 0$, several thin wires are placed in equal spacing d along the x axis while the z axis is along the wires. The distance between the cathode planes is typically three or four times larger than the spacing of the wires. Figure 3.3 shows a artistic impression of the detector geometry.

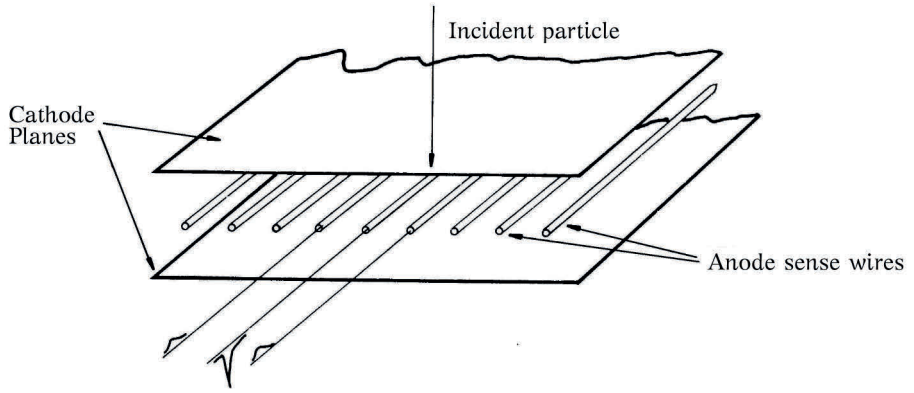

Figure 3.3: *An illustration of the MWPC geometry. Picture is taken from* [36].

In order to create an electric field in the active volume, negative potentials are applied on the cathode planes while the wires are kept to the ground potential. Assuming the coordinate system that was described before, the electric field strength is given by

$$E(x,y) = \frac{CV_0}{2\pi\varepsilon_0}\left[1+\tan^2\left(\frac{\pi x}{d}\right)\tanh^2\left(\frac{\pi y}{d}\right)\right]^{1/2}\left[\tan^2\left(\frac{\pi x}{d}\right)\tanh^2\left(\frac{\pi y}{d}\right)\right]^{-1/2}. \qquad (3.2)$$

In eq. 3.2, V_0 is the voltage applied to the cathode plane and C is the capacitance per unit length. The geometry of the electric field in MWPCs is shown in figure 3.4.

The working principle is the same as the proportional chamber. Particles penetrating the active volume ionise the gas along their path. The ions drift to the cathode planes while the electrons drift to the nearest anode wires and when the electric field is strong enough they initiate avalanche processes.

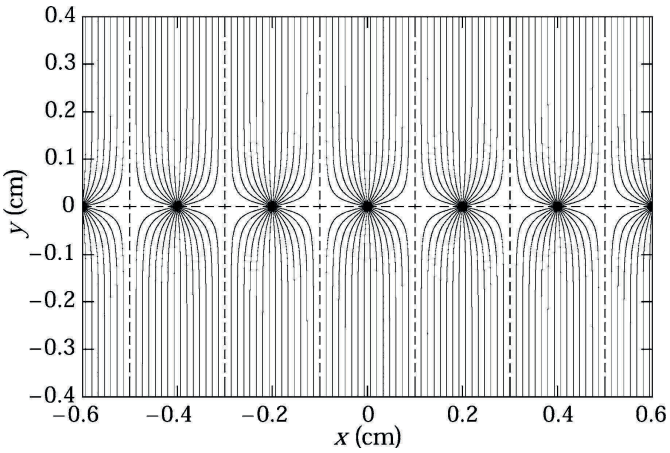

Figure 3.4: *Electric field geometry in a multi-wire proportional chamber. Picture is taken from* [72].

The main purpose of MWPCs is to enable the localisation of charged particles. This can be done with by reading out the signal of the wires. A single MWPC provides information only about the position in xy plane. For the z direction (along the wire) one has to stack several MWPCs with different wire orientations. However this method is not efficient for high particle rates when particles cross two MWPCs at the same time.

A solution to this problem is the segmentation of a cathode plane in strips which collect the ion signals. The coordinate along the wire is then given by the centre of gravity of the induced charge on the cathode strips. Depending on the segmentation, the position resolution can be improved dramatically. Usually the second cathode plane is segmented in a different orientation in order to exclude ambiguities.

3.2.3 Planar drift chamber

The drift chamber as a concept was introduced in 1971 by A.H. Walenta [70] and is a structure with geometry similar to the MWPC. The difference from the original design of the MPWC is that in the drift chamber between the anode wires are placed thicker "field wires". A sketch of the geometry is shown in figure 3.5.

The use of the field wires improves the uniformity in the region between the wires. A comparison of the electric field geometry of MWPCs and planar drift chambers is illustrated in figure 3.6. The electric field created in the region between the field and the anode wires pushes the electrons towards the anode wires. Close to the anode wires the electric field is getting stronger and the electrons create avalanches. By making use of appropriate electronics the time when the particle crosses the drift chamber can be measured. Therefore, the distance of the particle track from the

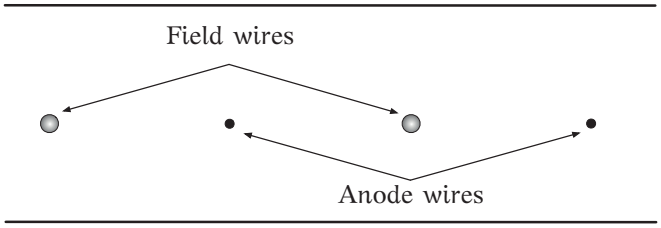

Figure 3.5: *An illustration of the geometry of a multi-wire planar drift chamber.*

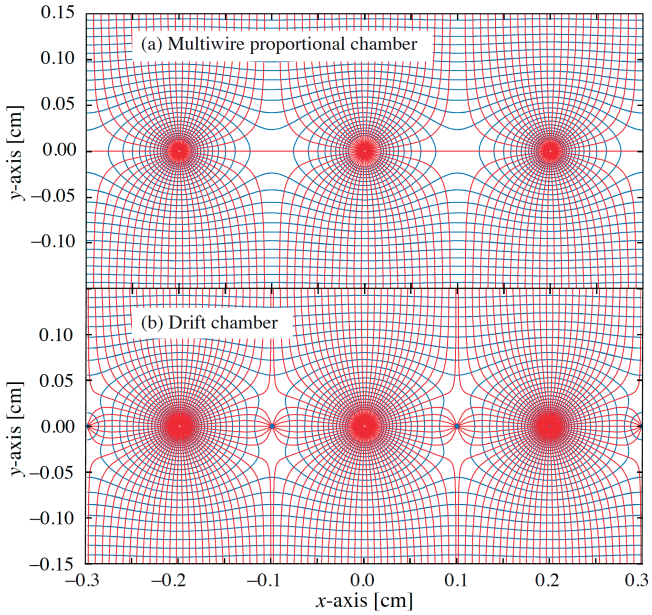

Figure 3.6: *Electric field lines and equipotentials in (a) a multiwire proportional chamber and (b) a planar drift chamber. Picture is taken from* [39].

anode wire can be measured by knowing the time difference between the crossing time of the particle and the arrival time of the avalanche at the anode i.e. the drift time.

The precision of the position measurement depends on the spacing of the wire and the resolution of the time measurement. The latter strongly depends on the time resolution of the electronics and the gas properties. Drift chambers have been used in different configurations in a large variety of experiments due to their high spatial resolution.

3.2.4 Time projection chamber

The time projection chamber (TPC) is a detector concept which combines both the principles of the MPWC and the drift chamber. The TPC is a large area cylindrical detector that was introduced for colliding beams experiments in 1978 by D. Nygren [71]. The chamber is split in two by a high voltage electrode placed at the central plane. The two end-caps of the chamber are filled with MWPCs equipped with alternating anode and field wires. The inner side of the end-caps is segmented in pad-rows parallel to the wires. Field shaping electrodes make sure that the electric field between the central electrode and the end-caps is uniform. Figure 3.7 shows a schematic of a TPC.

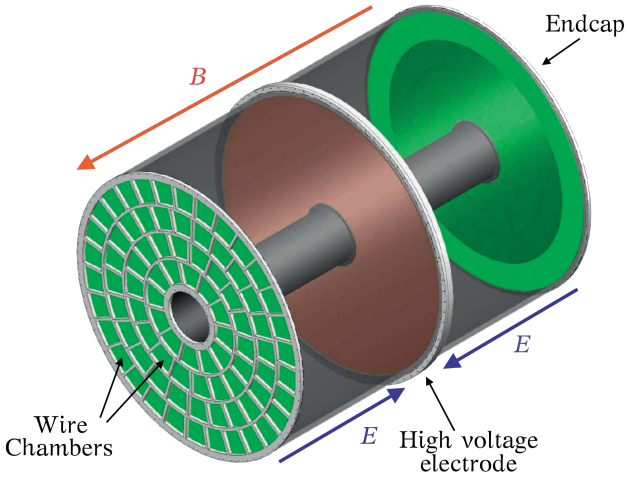

Figure 3.7: *An illustration of the geometry of a time projection chamber.*

The particles produced in beam collisions ionise the gas along their track. The electrons created drift towards the end-caps and eventually reach the anode wires where amplification occurs. The avalanche electrons are collected by the anode wires, while a positive signals due to the ions are induced on the pad-rows. With this configuration the particle track can be reconstructed in three dimensions. The pad position gives the x and y coordinates while the z coordinate is provided by the drift time measurement.

The analog signals of the anode wires can be used for energy loss measurements. This, together with the momentum measurement from the curvature of the tracks due to the magnetic field, make the TPC an excellent tool for particle tracking and identification. However, there are limitations in the rate capability due to the large drift times and the ion back-flow. A solution to the latter is provided by placing a gating grid between the end-caps and the central plane. For a detailed discussion on gating grids see [35].

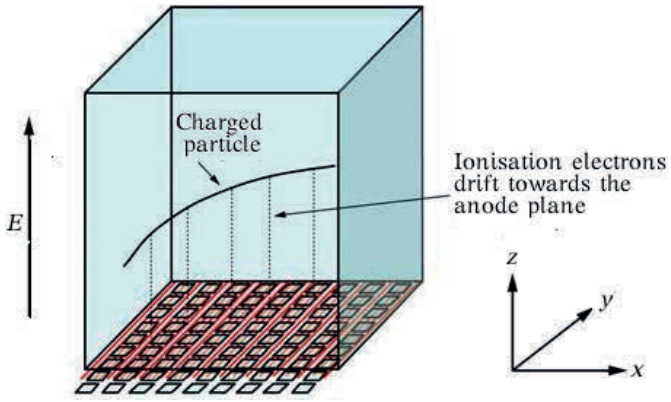

Figure 3.8: *An illustration of the working principle of a time projection chamber. Picture is taken from* [72].

3.3 Micropattern gaseous detectors

As we discussed in the previous section, the invention of the multi-wire proportional chamber gave a boost to the instrumentation of particle physics experiments. The traditional gaseous detectors have been used extensively as tracking detectors in many experiments. However, over the years with the modern experiments becoming more and more demanding, limitations have been reached in the rate capability and the segmentation.

Even if the construction techniques of detectors were optimised in order to improve the granularity, practical limitations rise when the wire spacing is reduced which make the detectors unstable. In order to overcome these limitations, a new generation of gaseous detectors was introduced. These detectors make use of micro-patterns for the amplification instead of wires. Such detectors belong to the family of the Micro-pattern Gas Detectors (MPGD).

Among a large variety of MPGD schemes, the most important are the MICRO-MEsh GAseous Structure (Micromegas) and the Gas Electron Multiplier (GEM). A honorary placement in the "hall of fame" of the MPGDs belongs to the micro-strip gas chamber (MSGC) which is the first MPGD developed. Nowadays the RD51 collaboration at CERN [73] is devoted to the development of micro-pattern gas detectors.

3.3.1 The micro-strip gas chamber (MSGC)

The first MPGD concept introduced was the micro-strip gas chamber (MSGC) by A. Oed in 1988 [74]. The MSGC is a parallel plate gas chamber where the top plane is conductive and acts as drift electrode. The back-plane consists of an

insulating substrate on which thin metallic parallel strips are deposited by using photolithography methods. The strip configuration is periodic such that wide cathode strips alternate with narrow anode strips, with a typical pitch of 100 μm. A schematic of the geometry is shown in figure 3.9.

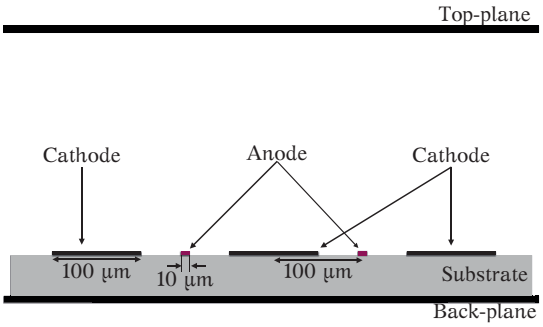

Figure 3.9: *An illustration of a cross section of the micro-strip gas chamber. The back-plane is filled with anode strips which alternate every 100* μm *with cathode strips.*

A traversing particle ionises the gas molecules along its path. Under the influence of the electric field between the top and the back-plane, the electrons released drift towards the back-plane. Due to the potential difference between the anode and the cathode strips a much stronger field is applied in the region close to the strips. Avalanche multiplication occurs and the electrons are focused to the anode strips while the ions are collected by the cathode strips. The electric field geometry close to the strips of a MSGC is shown in figure 3.10. Occasionally this geometry might change due to the accumulation of ions on the substrate surface.

Due to its fine granularity the MSGC delivered a much improved spatial resolution compared to multi-wire chambers. In addition, the fast collection time of the ions by the cathode strips improved the rate capability. Consequently the MSGCs have been used in high luminosity experiments. However, the vulnerability to discharges due to charging-up effects in the substrate and the ageing after long term use at high rates, led to the realisation of new detector concepts.

3.3.2 The micro-mesh gaseous structure (MicroMeGaS)

The micro-mesh gaseous structure or briefly micromegas was introduced by Y. Giomataris in 1996 [76]. The micromegas is a two-stage parallel plate chamber where the amplification takes place within an approximately uniform electric filed. The chamber is divided in two parts by a thin metal mesh, the drift region between the mesh and the cathode and the amplification region between the mesh and the anode. Insulating pillars every 1-2 mm keep the mesh flat at a distance 40-128 μm above the anode.

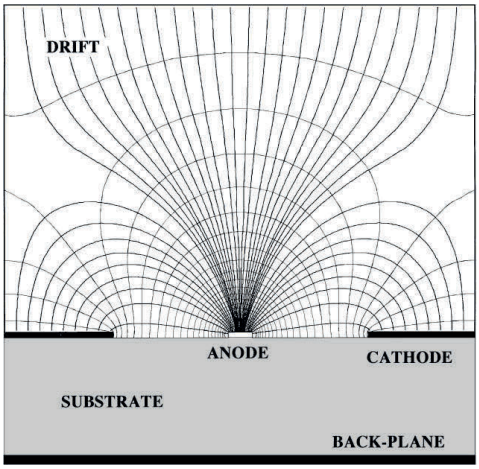

Figure 3.10: *The electric field lines and the equipotentials of a micro-strip gas chamber. Picture is taken from* [75].

In its original configuration the anode consists of strips on a printed circuit board (PCB), see figure 3.11.

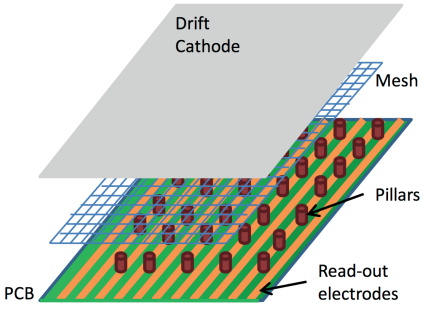

Figure 3.11: *An illustr ation of the geometry of a micro-mesh gaseous structure.*

Incident radiation in the drift region ionises the gas. Due to the applied electric field the primary electrons drift towards the mesh where they guided by the field lines through a mesh opening and eventually enter the amplification gap. The electric field in this region is much stronger and the multiplication of electrons takes place. The electrons are collected on the anode strips while the ions drift to the opposite direction and are collected at the micro-mesh.

Due to the electric field configuration shown in figure 3.12, the micro-mesh is

almost transparent to the ionisation electrons travelling from the drift region to the amplification gap. It also stops most of the ions drifting in the opposite direction minimising the back-flow. Moreover, due to the small size of the gap, the collection time of the signal for electrons and ions is fast which provides high rate capability.

The micromegas detector offers high spatial resolution thanks to the narrow amplification gap and the segmentation of the anode. Nowadays the micromegas is a well established technology with optimised production techniques which enable the construction of robust large area detectors. Under certain conditions, the micromegas appears to be vulnerable to discharges damaging the detector and readout electronics and/or lead to large dead times. In order to overcome such problems, the strips are protected with a resistive material.

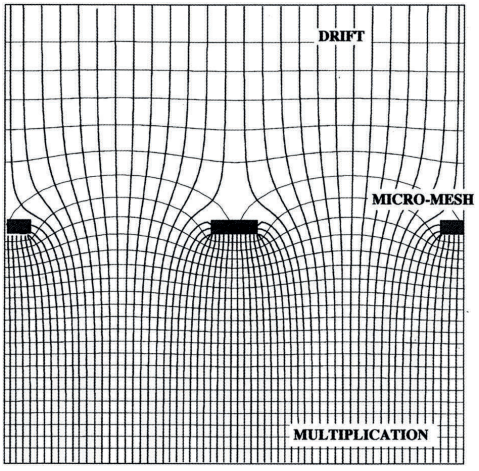

Figure 3.12: *The equipotentials and the electric field lines close to the mesh of a Micromegas. In the intermediate region between the drift and the amplification gap the field lines are focused through the mesh openings making sure that all the electrons are transmitted.*

3.3.3 The gas electron multiplier (GEM)

In 1997, F. Sauli introduced the Gas electron Multiplier [77]. Its basic element is a self-supporting layer called "GEM foil" . In its standard configuration, the GEM foil consists of a 50 μm thick copper-cladded kapton layer. The holes are etched in a triangular pattern, with a diameter of 70 μm and a spacing of 140 μm. Figure 3.13 shows a close view of a standard GEM foil.

The GEM foil is inserted between the cathode and the anode plane and divides the gas volume in three regions. The first region is a low electric field conversion gap between the cathode plane and the foil. Incident particles in the conversion gap

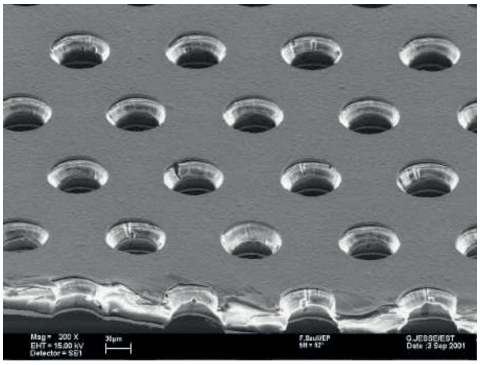

Figure 3.13: *A photograph of the hole pattern of a gas electron multiplier taken with a microscope.*

generate ionisation electrons which drift towards foil and enter the holes (the second region). Due to the potential difference in the top and bottom copper layer of the foil a high electric field is present in the holes. The electrons entering the holes are multiplied and most of them are transferred to the lower (third) region where they drift towards the anode plane segmented in strips or pads. The ions produced during the multiplication in the holes drift along the field lines and are guided towards the top metal layer of the GEM foil. Figure 3.14 shows the electric field configuration close to the holes of a standard GEM foil.

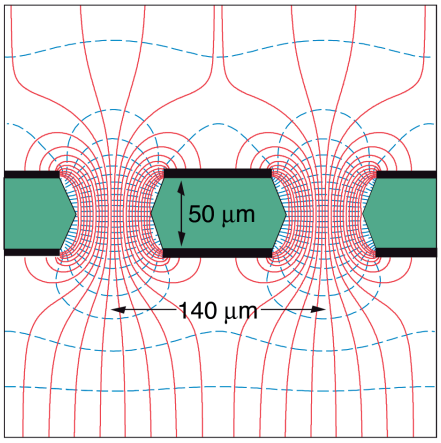

Figure 3.14: *The equipotentials and the electric field lines close to the holes of a gas electron multiplier. Picture is taken from* [39].

By stacking several foils with a thin transfer region in between, double-GEM or

triple-GEM structures can be made. The sharing of the multiplication between the foils could lead to higher multiplication. In addition, the operation of the cascaded foils at a lower voltage reduces the probability of streamer formations. Moreover, the absence of thin anodes make the GEM detectors insensitive to ageing effects up to high particle rates.

Nowadays the GEM manufacturing method is optimised and the production of large area GEM foils is possible. The techniques developed allow even the production of GEMs with a cylindrical shape. The robustness of the detector together with the high spatial and timing resolution enable the use of GEM detectors in many applications and experiments.

3.4 The GridPix

The GridPix detector is an innovative tracking detector which combines a micromegas grid with a CMOS pixel chip for the readout. The main difference with respect to the traditional micromegas grid is that in a GridPix detector the grid is integrated on top of the anode pixel array. The manufacturing of the grid is done at the wafer level by adding a few post-processing steps. Then the wafer is diced into chips which can then turned into a complete gaseous chamber.

The best feature of GridPix detectors is the ability of detecting single ionisation electrons with high efficiency. Moreover, the high segmentation of the readout chip together with the chip's functionality enable the reconstruction of a particle path in three dimensions with high accuracy. Therefore, the GridPix detector could be a powerful tool for tracking and energy loss measurements. Unfortunately without an appropriate protection the chip is vulnerable to discharges. This section gives a brief description of GridPix detectors.

3.4.1 Detector description

The basic element of the GridPix detector is the integrated grid (InGrid). An intermediate step before the chip fabrication is the deposition of a resistive thin layer as a protection against discharges. The GridPix structure under a microscope is shown in figure 3.15. Later on, the addition of a cathode plane completes the detector.

The production of the grid is done in such a way that above every pixel there is a hole with a diameter of 25-35 µm. The grid is kept at a distance of 50 µm above the chip by insulating pillars placed in between the pixels. The pillars have a diameter that is smaller than the pixel pitch. The InGrid is well aligned with respect to the pixels and minimises the dead areas.

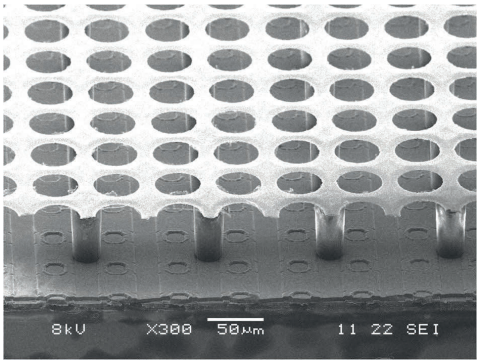

Figure 3.15: *A SEM photograph of an InGrid.*

3.4.2 Protection layer

The readout chip of a GridPix detector is vulnerable to discharges since every pixel contains sensitive electronics. The discharges occur when the transition of a avalanche to a streamer takes place with the mechanism described in chapter 2. In order to protect the chip, a thin layer of a resistive material is deposited on the chip surface. In the early GridPix years several materials where investigated [78] as well as several layers with varying thickness [79]. Nowadays 4 µm thick layers consisting of silicon-rich silicon nitride (SiRN) are used. In chapter 6 we perform a study of discharges in GridPix and investigate the use of alternative materials for the protection layer.

3.4.3 Working principle

In GridPix detectors the primary ionisation takes place in the drift gap which is defined between the cathode and the grid. In the drift region an electric field O(1 kV/cm) pushes the electrons towards the grid and they eventually enter a grid-hole. The electric field is much stronger, O(100 kV/cm), in the amplification gap due to its small size, figure 3.16. As a result the electrons gain sufficient energy to generate an avalanche.

The avalanche electrons are collected on the pixel pads while the ions drift in the opposite direction and most of them are collected by the grid. Depending on the size of the gap and the diffusion of the gas used, the full size of an avalanche is contained within a pixel area. Hence, the GridPix technology enables the detection of single ionisation electrons.

A particle traversing the drift region generates several ionisations along its path. Each one of the primary electrons drifts to the amplification gap and induces an avalanche on a pixel. The coordinate of the pixel gives the x, y position on the chip plane. Moreover, each pixel is equipped with electronics able to measure the drift

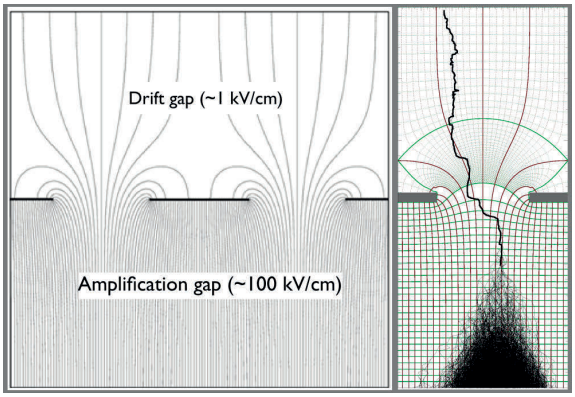

Figure 3.16: *On the left, an illustration of the electric field lines close to the grid of a GridPix detector. On the right, a primary electron enters a grid-hole, acquires enough energy and initiates the formation of an avalanche. The distances are not in scale.*

time which is used in order to reconstruct the z position along the drift direction. The reconstruction of the three-dimensional points corresponding to the creation positions of the ionisation electrons gives the 3D track segment of the incident particle.

3.4.4 Wafer post-processing

Nowadays the CMOS pixel chips used in GridPix detectors are produced in standard 8-inch silicon wafers. The fabrication of the integrated grid is done by using MEMS[1] wafer post-processing techniques. The processing steps for the production of GridPix detectors are shown in figure 3.17 and described below:

(a) A preliminary analysis of the quality of the wafer, i.e. wafer probing, takes place and the wafer surface is cleaned.

(b) The deposition of the protection layer is done by plasma-enhanced chemical vapour deposition (PECVD). The bonding pads of the chips are covered with polyamide which is then resolved.

(c) The wafer surface is covered with a 50 µm layer of SU-8 photoresist. After the deposition the SU-8 is soft baked on a hot plate to improve its mechanical properties.

[1]Microelectromechanical systems (MEMS) is the technology of very small devices

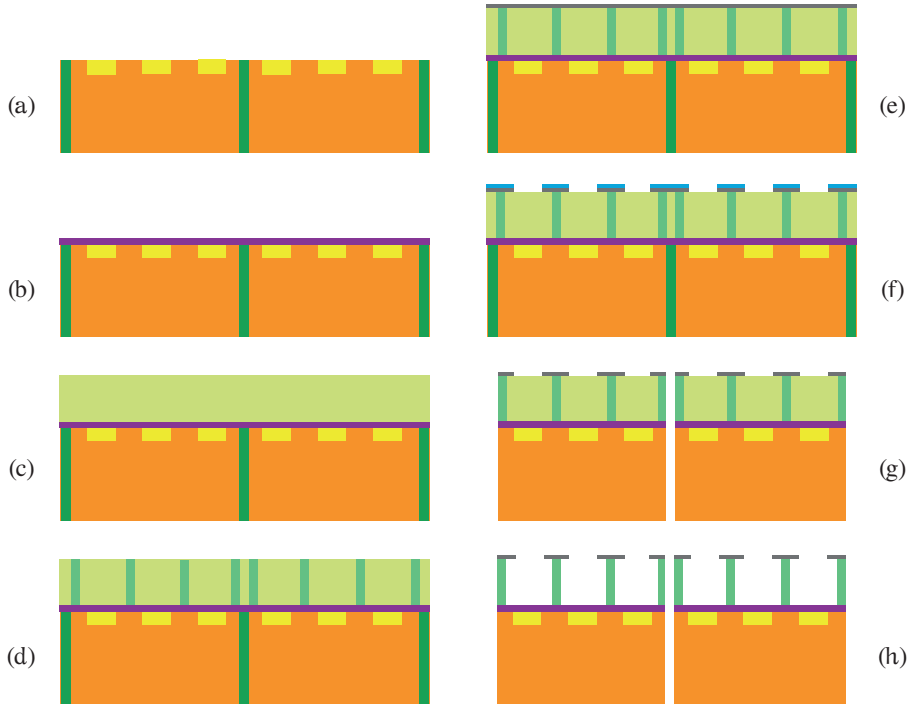

Figure 3.17: *The wafer post-processing steps for the production of an integrated grid. A brief explanation for each step is given in the text*

(d) The SU-8 is exposed to UV light. During this step the wafer is covered with a specially designed mask which collimates the UV light. The exposition creates the pillar structure.

(e) A thin (1 µm) aluminium layer is sputtered on the SU-8 by vacuum deposition.

(f) An additional thin layer (1 µm) of a photoresist is deposited on top of the aluminium. Exposition to UV light (using a mask) creates the grid-hole pattern. The photoresist is then resolved and the grid-holes are made with chemical etching techniques.

(g) The wafer is diced into separate chips.

(h) The unexposed SU-8 is resolved (wet chemical dissolution) and the GridPix-es are inspected visually and cleaned if necessary.

3.4.5 CMOS pixel readout

The use of pad-segmented anodes in gaseous detectors was introduced in order to overcome the limitations in the granularity of multi-wire chambers. However this readout scheme requires an increased amount of readout electronics. Soon enough it was realised that the readout can be done with pixelated chips made in CMOS technology. The pixel pad can be used for the collection and the recording of the charge. Nowadays, taking advantage of the modern photolithography techniques a large amount of electronic circuitry can be implemented within a pixel, enabling the basic processing of the signal collected.

Medipix family of chips

The GridPix detectors make use of pixel chips developed within the Medipix framework [80] at CERN. The Medipix2 chip [81] was the first chip of the family used in order to readout a gaseous detector using a micromegas grid for the amplification [82]. The Medipix2 chip is developed in 0.13 µm CMOS technology and consists of an array of 256 × 256 pixels. The pixel-size is 55 µm × 55 µm giving a total area of about 2 cm^2. The development aimed at photon counting and therefore the chip was suitable for time measurements.

The successful readout of gaseous detectors with the Medipix2 chip led to the realisation of the Timepix chip [83]. The pixel size remains the same, however the pixel-logic is re-designed in order to provide drift time measurements through the arrival time. The Timepix chip was a step forward and found immediate application in GridPix detectors. Nevertheless, for tracking applications, its slow front-end and the time-resolution were limiting the position resolution along the drift direction.

During the development of its successor, the Timepix3 chip [84], a series of prototype chips [85–89] known as "Gossipo chips" was developed in order to test designs for a faster front-end and different pixel topologies. The detectors used in this thesis make use of the Gossipo2 and the Timepix3 chip. A more detailed description will be given in chapters 4 and 5 respectively.

Pixel diagram

Each pixel in the CMOS chip consists of an analogue and a digital part. The analogue part typically consists of an input pad, a charge sensitive amplifier (CSA) and a discriminator. The block diagram of the analogue part is shown in figure 3.18. A signal collected at the input pad is amplified and is recorded only if it exceeds the threshold level at the discriminator. A 4-bit current adjustment circuitry is used to compensate for variations in the threshold level with respect to other pixels.

The digital part circuitry varies from chip to chip and is usually determined by the desired requirements. Depending on the pixel logic, the chip can be operated in various modes:

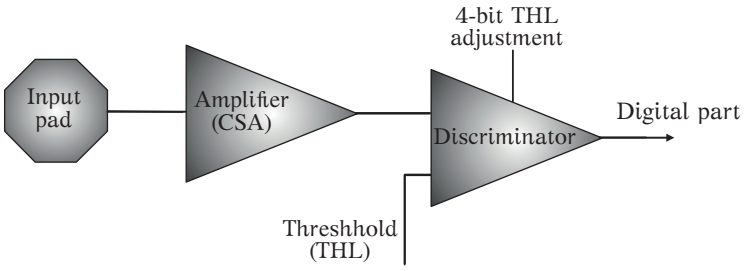

Figure 3.18: *A typical schematic of the analogue part of a single pixel for a chip of the Medipix family.*

- **Event counting mode**.
- **Time-of-arrival mode (ToA)**.
- **Time-over threshold mode (ToT)**.

A detailed description of each mode can be found in figure 3.19.

Threshold equalisation

In principle the design of each pixel is identical and as a result an identical uniform performance is expected for the pixels. However due to many reasons, variations in the performance from pixel to pixel arise. A common feature of the CMOS pixel chips after the production is the variation in the discriminator threshold of the pixels. In order to correct for this variation, the threshold equalisation procedure takes place. This procedure tunes the threshold level of each pixel by setting a specific adjustment DAC value (4-bits) aiming to reach an approximately uniform threshold value for all the pixels.

For the threshold equalisation the chip is operated in the ToT mode and in each pixel a test pulse is injected. For a given pixel, the adjustment DAC can take values from 0 to 15. Initially, the adjustment DAC is set to 0. A scan of the threshold DAC values (THL) takes place, beginning from a high value and is then lowered towards the noise. If a certain number of counts is reached for a certain value of THL, the value is added to the THL distribution. The same is done also for the case where the DAC value is set to 15. This method is know as the determination of the "noise floor". This procedure is repeated for all the pixels and the threshold is adjusted in

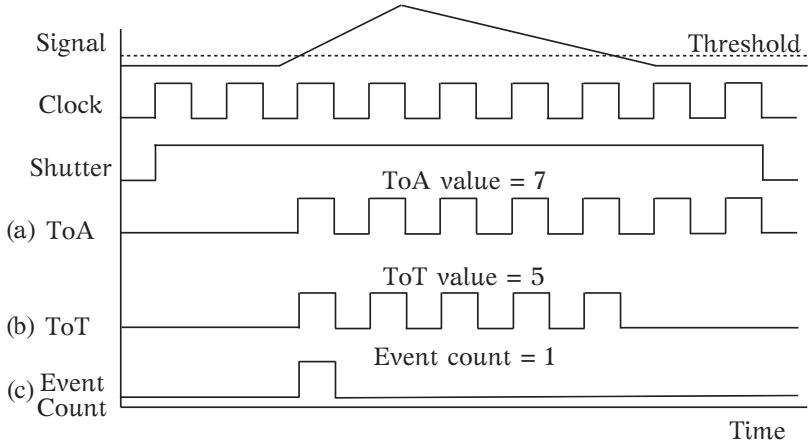

Figure 3.19: *An illustration of the various operation modes in a CMOS pixel chip of the Medipix family. An external trigger signal opens the shutter and the chip is able to record data. Depending on the chip settings at the time the signal crosses the threshold one of the following can be measured: (a) the Time of Arrival (ToA), where the signal's crossing-time of the threshold is measured (b) the Time over Threshold, where the charge of a signal is obtained by measuring the time that the signal remains above threshold, (c) the Event Counting mode where the amount of times a signal crosses the threshold level is measured.*

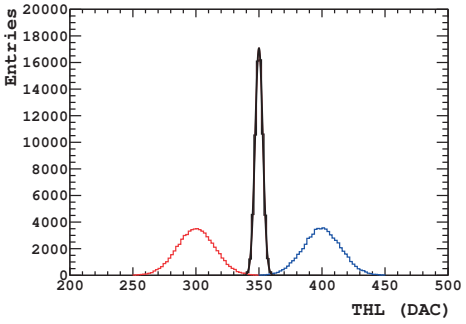

Figure 3.20: *The threshold (THL) distributions obtained from a typical equalisation procedure. The THL distributions before the equalisation are shown in red and blue for adjustment DAC equal to 0 and 15 respectively. In black, the THL distribution after the equalisation.*

order to match with the average of the THL distributions for DAC equal to 0 and 15. The result of the equalisation is shown in figure 3.20.

The black distribution in figure 3.20 corresponds to the equalised pixels after the adjustment. This distribution is centred around a mean value and fitted with a gaussian. The fitted mean of the gaussian μ_{eq} gives the common value for the threshold of equalised pixels. The fitted standard deviation σ_{eq} gives the threshold mismatch and is a characteristic of the chip.

Timewalk

Timewalk is an effect which occurs internally in the chip. It is a result of the variation in the amplitude of the induced signal on the pixels. For gaseous detectors especially, due to the gas gain fluctuations, timewalk is inevitable. Figure 3.21 illustrates the timewalk effect.

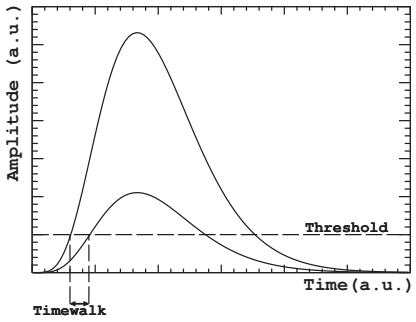

Figure 3.21: *Illustration of timewalk effect.*

The avalanche induced signals on the pixel can be coincident time-wise, they differ in pulse height though. For a low amplitude pulse it takes more time to cross the threshold level compared to a large one. As a result the low pulses appear to arrive later. A common method to correct for this effect is the used of a constant-fraction discriminator combined with a mean timer. An offline correction can be also obtained by using the information of both charge and arrival time. In chapter 5 we present such a method.

Chapter 4

High precision tracking with a miniature GridPix

"He is powerful and fast...
...but precision beats power and timing beats speed."
— Conor McGregor

4.1 Introduction

The concept of an integrated amplification grid directly on top of a CMOS pixel readout chip, exists already from the past decade. The manufacturing takes place after the micro-fabrication of the chip, by adding a few processing steps at the wafer level, [90]. This wafer post-processing technology was demonstrated for the first time in 2006, [91]. The result is a gaseous pixel detector capable of detecting single ionisation electrons. However, the chip used was offering limited functionality.

In parallel, the Medipix collaboration at CERN designed and delivered the Timepix chip, [83]. This chip provides timing information which enables the recording of the time-of-arrival (ToA) or the time-over-threshold (ToT). The Timepix chip has been used to a wide range of applications for the readout of gaseous or solid-state detectors. Despite the success, the Timepix chip features a time-to-digital Converter (TDC) with 10 ns resolution and a slow front-end ($\geq$ 100 ns rise-time) which limit the resolution along the drift direction.

The limitations of Timepix chip, led to the realisation of its successor, the Timepix3 chip, [84]. The design was aiming to a faster front-end ($\leq$ 25 ns rise-time) and a high resolution TDC per pixel. During the development for Timepix3, a series

of prototype chips, known as “Gossipo chips”, has been developed and tested. The Gossipo2 chip i.e. the second prototype, was the first chip which implements the topology of a high resolution TDC in each pixel, [86]. The Gossipo2 chip, is a small scale prototype with a 16×16 pixel array, produced in a multi-project wafer run (MPW), in 130 nm CMOS technology.

One of the Gossipo2 chips produced, was turned into a GridPix detector. The detector has been installed in a electron beam-line at DESY in order to test its performance. This chapter describes the experiment performed, the analysis and the results obtained with this miniature GridPix.

The main objective is to exploit the capabilities of the Gossipo2 chip and derive the tracking performance. Thanks to the high resolution TDC per pixel the drift time can be reconstructed with high precision. Thus, the resolution along the drift direction is expected to be improved.

The content of this chapter was published as an article with the name “Precision tracking with a single gaseous pixel detector” in Nuclear Instruments and Methods in Physics Research Section A: Accelerators, Spectrometers, Detectors and Associated Equipment, [92].

4.2 Detector description

4.2.1 Gaseous pixel detectors

As illustrated in figure 4.1, gaseous pixel detectors use a volume of gas as detection medium, with a CMOS pixel readout chip to register electrons liberated by the passage of ionising radiation. A conducting grid is built up above the chip (a gap of approximately 50 µm) using wafer post-processing techniques, with the grid holes precisely aligned to the pixel readout pads, giving uniform performance. The grid is supported on pillars situated between the pixel readout pads, avoiding dead areas. Applying a high E-field between grid and chip accelerates any electrons that enter, causing an electron avalanche with enough gas-gain for a single ionisation electron to be registered by the pixel-chip. A cathode above the grid creates a drift field with thickness from O(1 mm) (drift chambers) to O(1 m) (Time Projection Chambers).

Ionising radiation in the drift region liberates electrons in the gas, which drift down to the grid and enter the avalanche region. The position of the fired pixel combined with the measured ToA of the avalanche signal give the liberation point of the electron (“hit position") in 3D. The path of the ionising radiation can then be reconstructed by analysing all the hit positions.

4.2.2 Chip specifications

The chip was produced in a MPW run to test designs for a successor, Timepix3, to the Timepix chip. The main features implemented are a low-power and fast rise-time analog front-end (optimised to work in a gaseous detector) and a high-resolution

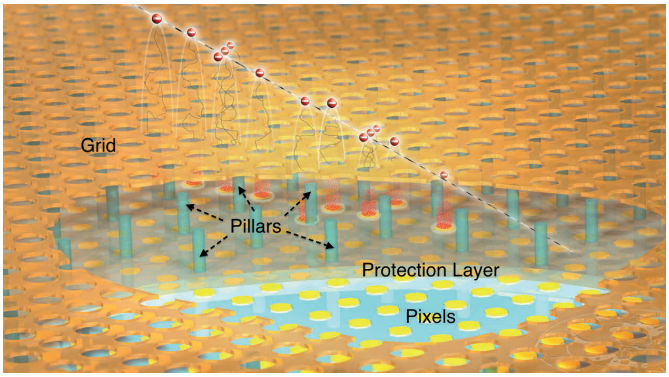

Figure 4.1: *Illustration of a Gaseous pixel detector showing the grid (orange) supported by pillars (green), the protection layer (grey) and the pixel chip (blue) with readout pads (yellow). An incident ionising particle liberates electrons along its track which drift to the grid, initiating an electron avalanche (red) in the strong E-field below the grid.*

low-power TDC in each pixel. The design performed in such a way that it is small enough to fit in the MPW run, but large enough to turn into a high-precision tracking-detector. The pixel array is a 16×16 matrix of 55 µm square pixel cells and covers a total active area of 0.88×0.88 mm^2. The total chip area is 2×3 mm^2 giving space for bond pads.

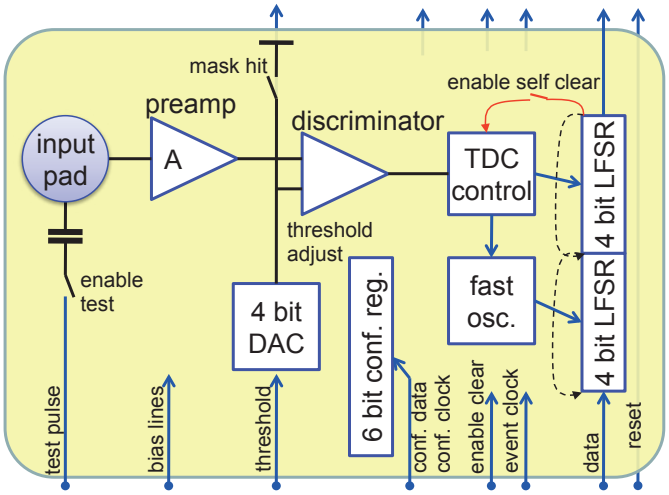

Figure 4.2: *Schematic of a pixel cell.*

As figure 4.2 shows, each pixel has a preamplifier and discriminator followed by a TDC. The preamplifier has a fast rise time (20 ns, [93]) compared to Timepix chips and low noise ($\approx 70\ e^-$). The discriminator threshold is controlled by an external level common to all pixels, and a local threshold adjustment to correct for pixel to pixel variations, controlled by a 4-bit DAC. The threshold can be set as low as $350\ e^-$ (5σ-noise) with negligible noise-hit rate.

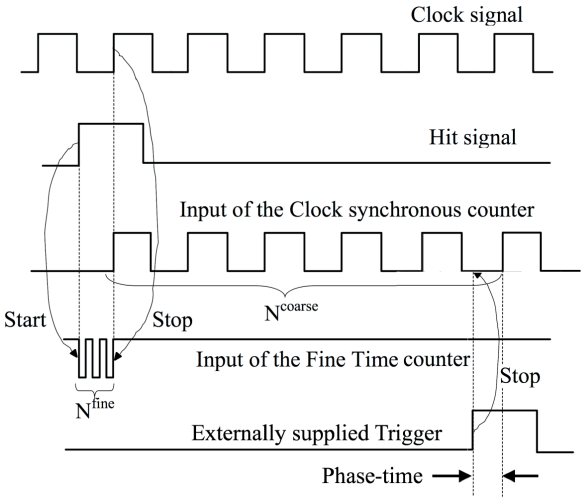

Figure 4.3: *Signal timing in the TDC circuit.*

The TDC has a 4-bit fine timestamp which counts pulses from a high-frequency (560 MHz) clock generated in the pixel, and a 4-bit coarse timestamp that counts pulses from an external 40 MHz clock. To reduce the power consumption the fast clock is dormant until a hit occurs and is stopped by the next rising-edge of the external clock, figure 4.3 (power consumption is 2 µW analogue and 0.25 µW digital, [86]). The coincidence of the hit and the rising clock-edge starts the coarse-counter, which is stopped by an externally supplied trigger acting as common-stop. For more details see [86], [93].

4.2.3 Detector fabrication

For handling purposes, the small-scale chip is glued to a standard 100 mm silicon wafer before processing it with MEMS post-processing steps. First an insulating layer of Silicon-Rich Silicon Nitride (SiRN), about 8 µm thick, is deposited everywhere except the bond pads. This protects the sensitive electronics in the chip against damage by discharges. Next a layer of SU-8 photoresist, about 50 µm thick, is applied and patterned using UV light in order to define the supporting structure. Careful alignment ensures the pillars are placed between the pixel pads. A thin layer about

1 µm of aluminium comes next, the patterning and etching of which creates the grid holes, again with precise alignment so that the holes are above the pixel pads. Development of the SU-8 follows, forming the supporting pillars.

The resulting basic detector unit is built into a complete gaseous pixel detector with cross-section shown in figure 4.4. We selected a standard chip-carrier package and made a hole in it in the active region to minimise multiple scattering of radiation. The integrated grid on its support silicon-wafer was mounted in this package and wire bonded to the carrier-pins, see figure 4.5.

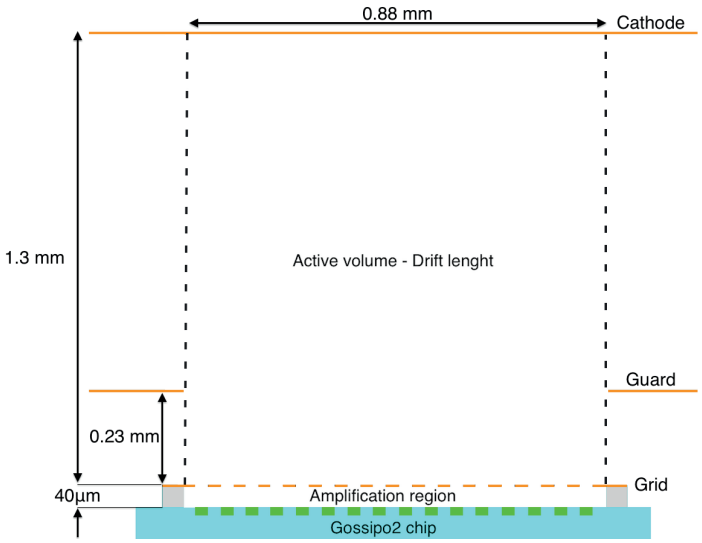

Figure 4.4: *Schematic illustrating the detector cross section.*

To minimise field-distortions at the edges of the detector a planar guard-electrode with laser-cut window above the grid was glued parallel to the chip-plane. A wall was added around the chip with two small holes for gas inlet and outlet. Finally a copper-plated mylar-sheet was glued to the top of this wall to make a gas-tight enclosure and to act as cathode. The cathode, guard-electrode, and grid potentials can be individually set via pins on the carrier, while the substrate is grounded.

During assembly, various geometrical parameters were measured with optical microscopy. The grid-height above the chip was measured by manual focusing. The guard height above the grid was measured by viewing at an angle of a high contrast picture. The cathode height was measured by an auto-focusing technique. The results are summarised in Tab 4.1.

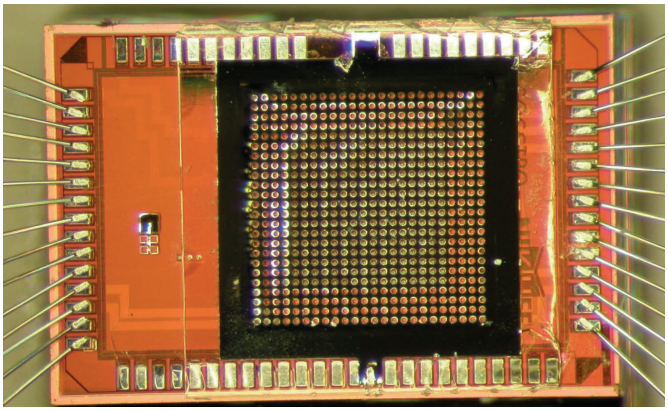

Figure 4.5: *Photograph taken during the detector construction, showing the grid and bond-pads with wire bonds going out to the carrier pins.*

Table 4.1: *Dimensions of the detector.*

Description	Units	Value
Number of pixel rows	-	16
Number of pixel columns	-	16
Row pitch	µm	55
Column pitch	µm	55
Grid-hole diameter	µm	30
Grid height above chip	µm	40 ± 3
Guard height above grid	mm	0.23 ± 0.05
Cathode height above grid	mm	1.3 ± 0.1

The detector is mounted on a custom circuit board that was developed for chip testing, and that board interfaces to a readout board with an FPGA which was programmed to load the chip registers (threshold adjustment DACs and configuration register) and read out the pixel TDCs as one long shift register of 2048 bits[1]. The FPGA board has a USB communication port connected to a computer for the DAQ system.

[1]The chip contains a 16 × 16 pixel matrix. Each pixel has a 4-bits fine counter and 4-bits coarse counter, which gives a total of 256 × (4 + 4) = 2048 bits.

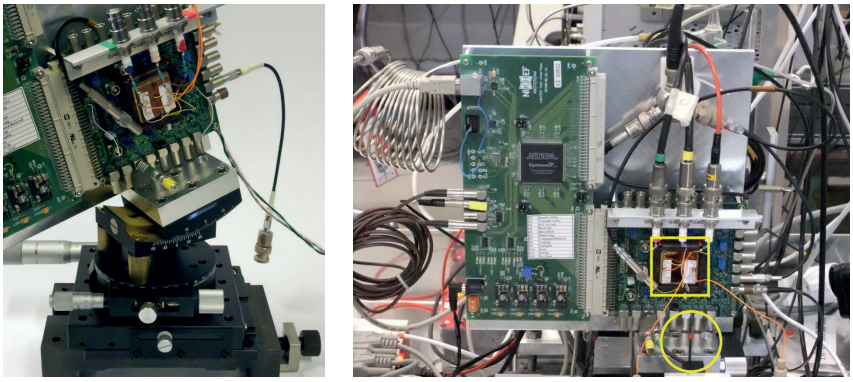

Figure 4.6: *On the left, the detector mounted on top of the precision stages. Goniometer, rotation stage, translation stage (from top to bottom). On the right, a photograph taken during the testbeam showing the detector in the bright rectangle. On the right bottom part, a bright circle highlights the vertical trigger scintillator.*

4.3 Testbeam measurements

In October 2013 the detector was placed in a DESY beam-line (T24) in order to test its performance. The beam was set to 4.4 GeV electrons at 1 kHz/cm^2, [94,95]. Our detector and associated equipment were mounted on a large remotely controlled stage provided by DESY allowing the detector to be positioned in the centre of the beam.

Table 4.2: *List of runs used. The goniometer was set to 15°. The grid voltage was -550V. Projection angle β is defined in Sec. 4.*

Run	Nominal rotation stage angle (°)	Projection angle β (°)	Triggers
1	-15	-12.54	10000
2	0	3.937	33000
3	10	11.80	10000
4	15	16.34	10000
5	20	21.32	10000
6	25	25.98	10000
7	30	30.07	10000
8	45	44.96	10000

The detector and readout boards were mounted on a series of three manually

adjustable precision stages (figure 4.6, left): a goniometer allowing a tilt angle about a horizontal axis; a rotation stage allowing rotations about a vertical axis; and a translation stage to move the detector horizontally perpendicular to the beam line. The rotation stage allows several different track-angles to be investigated (see table 4.2). The translation stage was mounted on an optical bench.

A trigger system detects the passage of a particle through the active gas volume. This consisted of two small scintillators of 1 mm diameter and 5 mm long, connected to a H10721-110 Hamamatsu photomultiplier. One scintillator was placed vertically (figure 4.6, right), in front of the detector, connected to the optical bench via a remote-controlled translation stage moving it horizontally across the beam. The other scintillator was placed horizontally, behind the detector, connected to the optical bench via a stage that moved it vertically. A coincidence of the two scintillators acted as beam trigger. The alignment of the trigger scintillators to the detector was made by scanning through different positions of the scintillator stages, optimising the trigger rate. Alignment needs to be precise given the small active length of the detector and scintillator (slightly less than 1 mm since the amount of scintillation-light for beam particles traversing the edges is below threshold).

The arrival time of a trigger relative to the nearest rising edge of the 40 MHz clock was recorded in a TDC. All drift times measured by the chip were adjusted offline by this "arrival phase-time" (see figure 4.3).

The detector was connected to a gas system which permanently flushed the active volume. We used pre-mixed CO_2 and dimethyl-ether (DME) with target mixture 50:50. Analysis at an external company[2] resulted in the gas composition given in table 4.3. Although this gas mixture is flammable and requires standard safety precautions, its very low diffusion of approximately 25 $\mu m/\sqrt{mm}$ makes it interesting for precise measurements.

Table 4.3: *Gas mixture used.*

Gas	Fractional content (v/v)
CO_2	0.48
DME	0.52
O_2	< 50 ppm
H_2O	100 ppm

The voltages of the cathode, guard-foil, and grid were set remotely. The cathode-to-grid potential difference controls the drift field and hence drift velocity. It was set to 144 V aiming at 1.1 kV/cm with a drift velocity of 4.9 µm/ns and close to a minimum in the diffusion coefficients for this gas. The grid-to-chip potential difference controls the gas gain. For the results presented here, the grid was set to

[2]Intertek Polychemlab BV, Koolwaterstofstraat 1, 6161 RA Geleen, Netherlands

-550 V giving a gain-field of 137.5 kV/cm. We have estimated the mean input signal gain, using the preamplifier gain specified by the ASIC designers, to be ~5000 (the gas gain is somewhat higher). The guard voltage was set accordingly to provide a uniform field at the active-region edges, by scaling the grid-to-cathode voltage by the ratio of the heights above the grid of the guard and cathode.

The threshold was set high (840 e^-) to avoid noise-hits, even in some noisy pixels. In retrospect, some data at a lower threshold would have been interesting – it would have had less timewalk and so better resolution, provided the noise-hits could be removed off-line.

4.4 Track reconstruction and fitting

The DAQ system records all data in an ASCII file. The header of this file contains information about environmental conditions such as temperature, pressure and voltage settings. In the main part of the file, we store the event-by-event data with the event number and the trigger-arrival phase-time, followed by 256 integers containing both coarse and fine values of the TDC of each pixel.

First these data are processed to make a zero-suppressed file: for each event the trigger-arrival phase-time, k_ϕ, is followed by a list of pixel-hits, storing the column i, row j, fine-time k_f, and coarse time k_c of the hit (all four have a range 0 - 15). The row and column are evaluated taking into account the way the pixels are connected on the chip into one long shift register. The TDC values are decoded from the pattern produced by the LFSR to a binary representation. This step considerably reduces the data to be stored and processed in further analysis.

In the next step, the pixel-hits are calibrated into positions. No attempt is made to coalesce neighbouring pixels into a cluster – each pixel-hit is treated as if it came from a separate ionisation cluster We use a local chip coordinate system with x corresponding to the column, y to the row, and z to the height above the grid. The origin of this coordinate system is in the grid, centred in the pixel array. These positions are evaluated as:

$$x = (i - 7.5)d_p\,, \tag{4.1}$$

$$y = (j - 7.5)d_p\,, \tag{4.2}$$

$$t = T_0 - [\tau_c k_c + \tau_f k_f - (\tau_\phi k_\phi - t_0)]\,, \tag{4.3}$$

$$z = v_D t\,, \tag{4.4}$$

where d_p is the pixel pitch of 55 µm. The τ constants convert the TDC's to ns. The values used are $(\tau_c, \tau_f, \tau_\phi)$ = (25.0, 1.8, 0.001) ns/count. In equation (4.3), t_0 is the smallest phase registered and T_0 is chosen to make the earliest pixel-hits get positioned at $z = 0$. No attempt has been made to give individual pixel T_0-values, since pixel to pixel variations seem to be very small. The value for τ_f depends on

the chip power supply voltage, which must be tuned so that the fine-TDC spans the full 25 ns clock period. It is measured using a test pulse and a programmable delay. More will be said about deriving the drift velocity v_D later.

Several effects contribute to errors in the hit position. The above equations place hits at the centre of a voxel, when in reality they could have been created anywhere in the voxel. This introduces an rms error of $1/\sqrt{12}$ of the appropriate voxel dimension. In addition, transverse diffusion during drift adds to the x and y position uncertainty, while longitudinal diffusion adds to the z uncertainty. Finally, there is a large stochastic gain-spread from one electron avalanche to the next. Larger pulses trigger the discriminator sooner than small ones, leading to timewalk fluctuations.This adds another error to z, in fact the dominant error. For simplicity, we treat this as a Gaussian error, while in reality it has a large tail to late trigger times. We therefore attribute the following errors to (x, y, z):

$$\sigma_x^2 = \sigma_y^2 = \frac{d_p^2}{12} + D_T^2 z, \tag{4.5}$$

$$\sigma_z^2 = \frac{(\tau_f v_D)^2}{12} + D_L^2 z + (\sigma_w v_D)^2, \tag{4.6}$$

where D_T and D_L are the transverse and longitudinal diffusion coefficients and σ_w is the time-spread contribution from timewalk, derived as described below. figure 4.7 shows a typical event, with 7 hits drawn at their estimated positions and error bars from equations (5.21) and (5.22) and the track fitted through the hits.

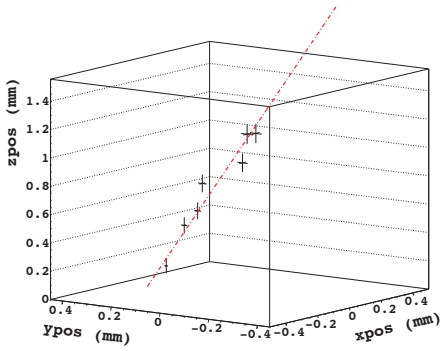

Figure 4.7: *An example event with 7 hits superimposed with the fitted track, and indicating the errors in the hit-position estimate.*

Track reconstruction follows the method used in [96]. We require 3 or more pixel-hits in an event. This is the only event-selection filter. We then fit the xz and yz projections separately,

$$x = b_x + m_x z\,,$$
$$y = b_y + m_y z\,, \tag{4.7}$$

using York's method [97]. This iterative method correctly obtains the best line in the presence of errors on both variables. It is a weighted fit, using the errors in equations (5.21) and (5.22). The fit routine returns the fitted offsets and slopes (b_x, m_x) and (b_y, m_y) as used in (4.7), their covariance matrices, and the chi-squares of the fit. The fit is carried out in a frame with z centred not at the grid but at the weighted mean of the hit z coordinates b_z:

$$b_z = \sum_{\text{Hits } i} W_i z_i \Big/ \sum_i W_i\,,$$
$$W_i = (\sigma^2_{x_i} + m_x^2 \sigma^2_{z_i})^{-1}\,. \tag{4.8}$$

In this frame, the error in the intercept is uncorrelated with the error in the slope and therefore the error matrix is diagonal, and furthermore the errors on the fit parameters are minimised.

This fitting procedure measures the slopes of the projections of tracks on the xz and yz planes of the chip frame. The projection angles corresponding to these slopes are

$$\alpha = \arctan m_x\,,$$
$$\beta = \arctan m_y\,. \tag{4.9}$$

These can be related to the rotary-stage and goniometer scale-readings (θ, ϕ) and mis-alignment offsets (θ_0, ϕ_0) using rotation matrices[3]. Reasonable care was taken to align the detector axes with the stage axes. Under the simplifying assumption that the rotation axes coincide with the x (vertical) and y (horizontal) axes of the detector, the result is

$$m_x = \sin(\phi - \phi_0)\tan(\theta - \theta_0)\,, \tag{4.10}$$
$$m_y = -\cos(\phi - \phi_0)\tan(\theta - \theta_0)\,, \tag{4.11}$$
$$m_{xy} = \tan(\phi - \phi_0)\,, \tag{4.12}$$

where in (4.12) we introduce the slope of the track projection in the xy plane. This slope is independent of the drift-time and therefore of drift velocity and timewalk errors. It allows ϕ_0 to be determined, by plotting $[-\arctan m_{xy} + \phi]$ vs θ, figure 4.8. ϕ_0

[3]For the derivation see the appendix A.

is small, −0.5° average for nominal angles between 10° and 30° (given in table 4.2). The slight systematic deviation visible could be an indication of misalignment of the detector axes to the rotation stage axes.

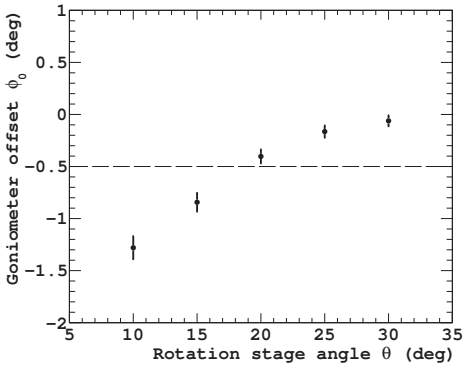

Figure 4.8: *Estimate of the offset ϕ_0 from different runs labelled by θ. The dashed line shows the the correction chosen.*

The drift velocity is then derived from runs 1 and 4, made at nominal angles of $\theta = \pm 15°$ to the beam. The difference in angle between these runs is independent of θ_0. Applying (4.11) to both runs gives

$$2\theta = \arctan\left(\frac{(m_{y+})}{\cos(\phi - \phi_0)}\right) - \arctan\left(\frac{(m_{y-})}{\cos(\phi - \phi_0)}\right). \tag{4.13}$$

Underestimating v_D would lead to too large an opening angle; overestimating v_D would give too small an opening angle. Starting from the value we obtain from a simulation with Garfield[4], v_D was adjusted to give precisely 30° in (4.13). Taking into account that the reading error in the rotation stage angle is minor, this method results in $v_D = 5.10 \pm 0.02$ µm/ns. A field of 1.2 kV/cm has this drift velocity in Garfield, giving a corresponding drift gap of 1.21 ± 0.05 mm, consistent with the optical measurement in table 4.1. At this field Garfield gives diffusion coefficients $D_L = 25.5$ µm/ $\sqrt{\text{mm}}$ and $D_T = 23.4$ µm/ $\sqrt{\text{mm}}$, which we use in eq. (5.21),(5.22).

The offset θ_0 is then derived by plotting

$$-\arctan\left[\frac{-m_y}{\cos(\phi - \phi_0)}\right] + \theta \text{ vs. } \theta,$$

which should give a horizontal line at θ_0, figure 4.9. There are some angle-dependent systematics discussed in Sec. 4.5.1 for large angles and for nominal angles close to 0°,

[4]Garfield is a computer program for the detailed simulation of two- and three-dimensional drift chambers. An interface to the Magboltz program is provided for the computation of electron transport properties (link).

but elsewhere θ_0 is constant at -2°. Table 4.2 gives the projection angles calculated from eq. 4.11, corrected for θ_0 and ϕ_0.

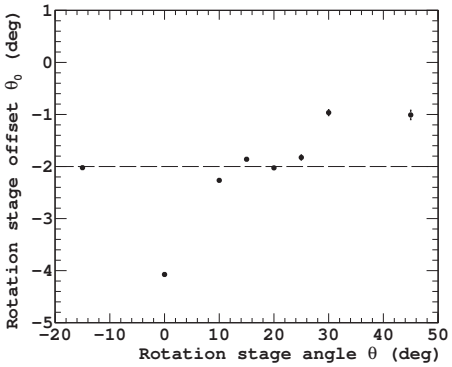

Figure 4.9: *Estimate of the rotation stage offset θ_0 for runs at different angles θ. The dashed line shows the correction chosen. At 0° and above 30° other systematics affect the result, see Sec. 4.5.1.*

The timewalk error depends on gas gain fluctuations, which are unknown, and the electronic behaviour of the chip. We estimate it as follows. From the chi-square of the York-fit and the number of degrees of freedom (number of hits minus two) we calculate the "fit probability" shown in figure 4.10. When the errors are correct, this fit probability distribution is flat over a large range. The unknown timewalk contribution was adjusted to make the fit probability flat, resulting in σ_w = 13 ns. Though still large compared to σ_x and σ_y ($\sigma_w v_D > \sigma_x$), is much less than the 21 ns in [96], using the Timepix chip. Figure 4.10 shows the resulting probability distribution. The peak at low values is due to wrong hits (noise, δ-rays, interactions causing two tracks etc.). Over the range 0.2 to 1.0, it is reasonably flat indicating that the errors are correct.

For illustration of the hit-position resolution, table 5.4 gives their values at various heights. These can be compared to [96]; the important difference is the improvement of the z-resolution, due to the timewalk reduction from 21 ns to 13 ns here.

z (mm)	σ_x (µm)	σ_y (µm)	σ_z (µm)
0.0	15.9	15.9	66.7
0.6	24.1	24.1	69.5
1.2	30.1	30.1	72.3

Table 4.4: *The hit position resolution at various heights which determine the size of the resolution voxel.*

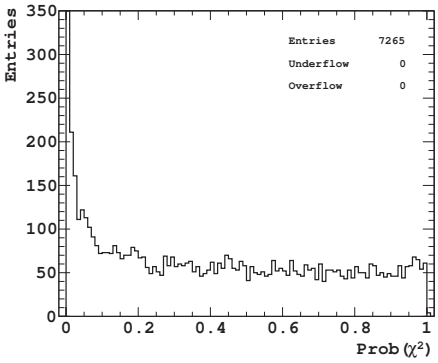

Figure 4.10: *Track χ^2 fit probability distribution of run 5.*

4.4.1 Angular resolution analysis

The angular resolution is determined in two ways, and the agreement of these gives confidence in the method. In the first, we take the rms width of the fit-angles as the angular resolution (figure 4.11). The beam divergence is much smaller than our resolution, so this method gives a robust estimate of angular resolution. The rms width was extracted by fitting a Gaussian to the central $\pm 2\sigma$ region.

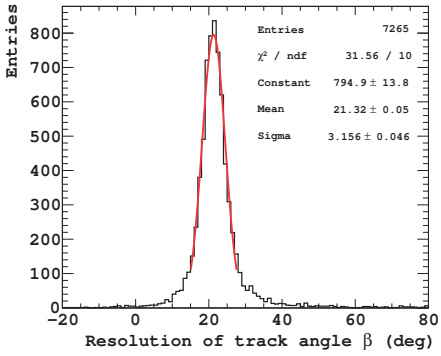

Figure 4.11: *The rms width of the angle distribution fitted with a Gaussian to the $\pm 2\sigma$ central region for run 5. The sigma is a robust measure of the angular resolution.*

In the second method, we take the error σ_{m_y} in the slope from the covariance matrix element. We use error propagation to convert this to an error σ_β in the angle

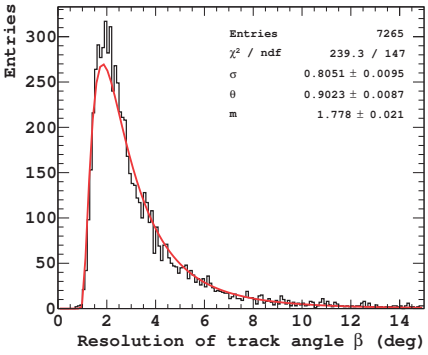

Figure 4.12: *The square root of the covariance matrix element corresponding to the angle, fitted with a lognormal distribution for run 5. From the fit parameters we calculate that the mode resolution is 1.8° and the mean resolution is 3.4°.*

β. This is histogrammed in figure 4.12 which we fit with a lognormal function[5]. We take the mean of the fit as the resolution.

4.4.2 Position resolution analysis

Since we have no beam-telescope to give an external reference for the tracks, we have only the covariance matrix of the fit to estimate the position resolution. This has been shown to work well in [96], and the agreement between the two methods for the angular resolution gives confidence in this estimate.

The point (b_x, b_y, b_z) resulting from York's method lies on the fitted track. When viewed along the z-axis, only the errors on b_x and b_y matter. However, when a detector is used with external references, and the fitted track has to be rotated to some other coordinate system, the z-uncertainty also becomes important. The detector has a more fundamental set of track-resolution parameters $(\sigma_{T_x}, \sigma_{T_y}, \sigma_{T_z})$, from which the resolutions in rotated reference frames can be derived. The fit-errors are related to these more fundamental errors by:

$$\begin{aligned} \sigma^2_{b_x} &= m_x^2 \sigma^2_{T_z} + \sigma^2_{T_x} , \\ \sigma^2_{b_y} &= m_y^2 \sigma^2_{T_z} + \sigma^2_{T_y} . \end{aligned} \tag{4.14}$$

From symmetry of the detector, $\sigma_{T_x} = \sigma_{T_y}$ so these detector resolutions can be derived from the measured resolutions at a given slope from

[5] $f(x) = \frac{e^{-[(\ln((x-\theta)/m))^2/(2\sigma^2)]}}{(x-\theta)\sigma\sqrt{2\pi}}$. The formula was taken from NIST/SEMATECH e-Handbook of Statistical Methods (link).

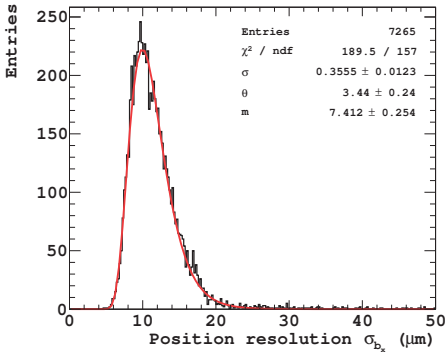

Figure 4.13: *The square root of the covariance matrix element corresponding to the position, fitted with a lognormal distribution for run 5. From the fit parameters we calculate that the mode resolution is 10* μm *and the mean resolution 11.3* μm.

$$\sigma^2_{T_z} = \frac{\sigma^2_{b_x} - \sigma^2_{b_y}}{m^2_x - m^2_y},$$
$$\sigma^2_{T_x} = \sigma^2_{T_y} = \sigma^2_{b_x} - m^2_x \sigma^2_{T_z}. \tag{4.15}$$

For further details see [96].

The position resolutions σ_{b_x} and σ_{b_y} are extracted from fits as in figure 4.13. From these we calculate the detector track resolution using eq. (4.15), by histogramming σ_{T_x} and σ_{T_z} and taking the mean. We also calculate the position-resolution dependence on the number of hits.

4.4.3 Efficiency

The number of primary ionisation clusters follows a Poisson distribution. Due to the low diffusion and the small drift gap, to a good approximation all electrons of a cluster end up in the same pixel giving only one hit. Therefore the number of pixels hit should follow a Poisson distribution. However this needs some care due to edge effects and dead pixels in the chip used. Figure 4.14 shows a 2D-histogram of the total number of hits in each pixel. The dead pixels are clearly seen, and are not evenly distributed. This produces not one Poisson distribution, but several, depending on which region a track is in. Also, many tracks do not have their full track length in the active region: some enter or leave via a side wall of the active region. To estimate the detection efficiency, we have therefore defined a fiducial region of the detector. This region limits tracks to those which enter and leave by

the top and bottom faces of the active region; and in addition project onto pixels in the bottom right quadrant of figure 4.14, where most pixels are working.

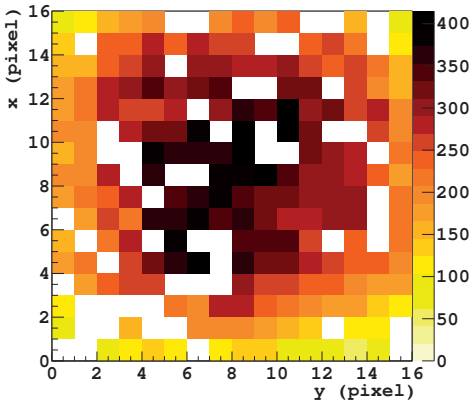

Figure 4.14: *Two-dimensionatl histogram of the total number of hits per pixel for run 5. The pixel shade corresponds to the number of hits; white bins correspond to the dead pixels.*

The number of pixels hit i is histogrammed for all tracks ($N_{hits} \geq 3$) in this fiducial region and fitted with a Poisson function (eq. 4.16) to obtain the mean number μ of pixel-hits on a track:

$$P(i;\mu) = \frac{e^{-\mu}\mu^i}{i!}\,. \tag{4.16}$$

We derive the detection efficiency from the mean. Two numbers are important here: the first one which we call Electron Detection Efficiency, ϵ_e, which is the efficiency for the detector to see at least one hit coming from the passage of a high energy electron:

$$\epsilon_e = 1 - P(0;\mu)\,. \tag{4.17}$$

This is important for knowing how many tracks can pass through totally undetected. The second, which we call Track Detection Efficiency, ϵ_T, is how often at least three pixels are registered. This is a typical requirement for fitting a local track in a detector.

$$\epsilon_T = 1 - \sum_{i=0}^{2} P(i;\mu)\,. \tag{4.18}$$

The efficiency would improve if all the pixels were working in the fiducial volume. However this effect is very small because most events have many ionisation electrons and the chance that all end up to the same dead pixel is negligible.

4.5 Results

4.5.1 Angular resolution

Figure 4.15 shows the difference between the fitted track angle (eq. 4.9) and the actual angle β obtained from eq. 4.11. The fitted angle is taken as the mean of the Gaussian fit used to extract the resolution, see figure 4.11.

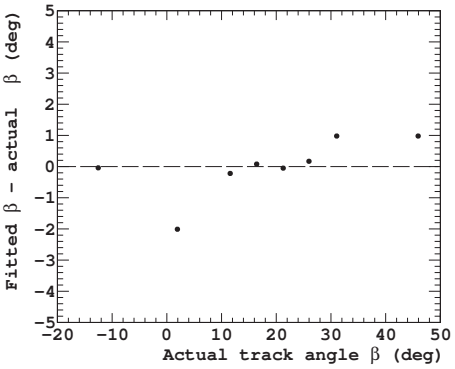

Figure 4.15: *Difference between measured and actual angle versus the actual angle. At large angles and at zero degrees there are small systematic deviations, discussed in the text.*

Above 30° the edge effects due to the small size of the chip limit the angular performance of the detector, including a small systematic bias. These effects will be much less important for full size chips, and also possibly can be reduced with better field-shaping around the chip edge.

Close to 0° there is also a local systematic bias: all electrons from perpendicular tracks tend to arrive in a single pixel. These then give low track-efficiency. A track is only fitted when some electrons undergo large diffusion to neighbouring pixels, so only events with badly measured hits get a track fitted. When one angle is non-zero, and the other is close to zero, all pixel-hits line up in a single column or row. Again, this gives either precisely zero slope, or high diffusion occurs and distorts the fit. In use in an experiment, if the radiation to be measured is highly collimated, the detector should be placed at an angle to the beam to avoid these problems. In experiments with tracks over a large range of angles, the region with distortions is a small part of the track phase space. The effects will be much reduced with a larger drift gap; also smaller pixels and possibly multi-hit electronics in each pixel would help.

Figure 4.16 shows the angular resolution versus the rotation angle of the detector for the two different methods. There is good agreement, confirming the covariance

matrix element method is reliable.

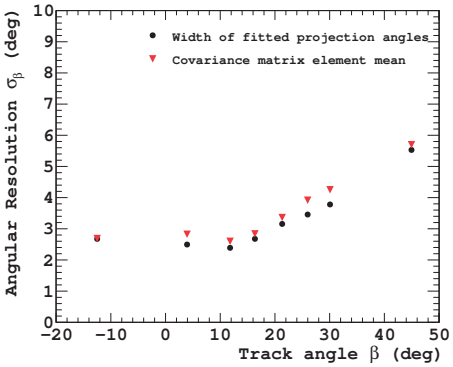

Figure 4.16: *Angular resolution versus angle from two methods.*

The angular resolution depends on the number of hits – more hits give better resolution with a $1/\sqrt{N_{\text{hits}}}$ dependence. Figure 4.17 shows this effect. For a typical track with six hits (the mean) and small angles (around 10°) the angular resolution is 2.5°. With Timepix3 chips further reducing timewalk, the resolution for larger angles will be closer to this value than the current detector. Furthermore, with a larger chip the drift gap can be increased up to around 10 mm (above this, diffusion reduces the benefits), giving a big improvement in the angular resolution (without diffusion, the resolution on the slope parameter would follow approximately (track-length)$^{-3/2}$ (increase in the number of hits gives power 1/2 and the track-length increase gives power 1).

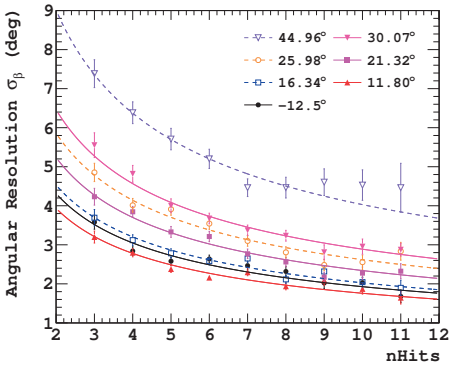

Figure 4.17: *Angular resolution versus the number of hits for different angles. The curves are fitted with a $1/\sqrt{N_{\text{hits}}}$ dependency.*

4.5.2 Position resolution

Using the eq. (4.15) for all the different runs (table 4.2), we extract the detector track position resolution dependence on the track angle. figure 4.18 shows the results. We quote the derived resolutions $\sigma_{T_{x,y}}$ and σ_{T_z} as the position resolution of the detector. Note that while σ_{b_x} and σ_{b_y} vary with angle, the detector track resolutions σ_{T_x}, σ_{T_y} and σ_{T_z} are constant over a wide range.

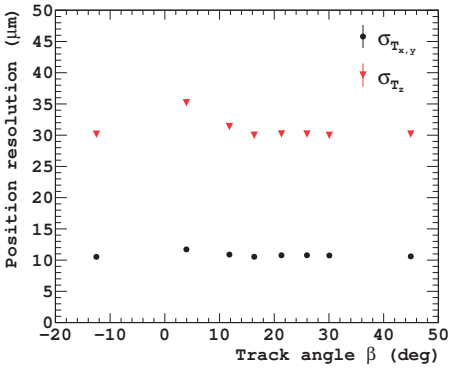

Figure 4.18: *Track position resolutions versus the track angle.*

Figure 4.19 shows the position resolution dependence on the number of hits which varies as $\sim 1/\sqrt{N_{\text{hits}}}$. The data is for run 5; other runs show similar behaviours. For a typical track consisting of 6 hits the average resolution is 10 µm for the x and y position and 29 µm for the z position.

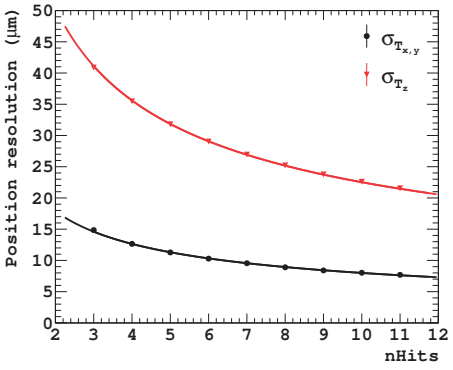

Figure 4.19: *Track position resolution dependence on the number of hits for in-plane and drift directions. The curves are fitted $1/\sqrt{N_{\text{hits}}}$ dependency.*

The worse z position resolution is due to the timewalk. In Timepix3, ToA corrections using ToT information should bring the σ_{T_z} curve much closer to the $\sigma_{T_{x/y}}$ curve. At large N_{hits} the resolution is around 8 µm; although only for a small fraction of events, this is an impressive achievement for a single gaseous detector.

4.5.3 Detection efficiency

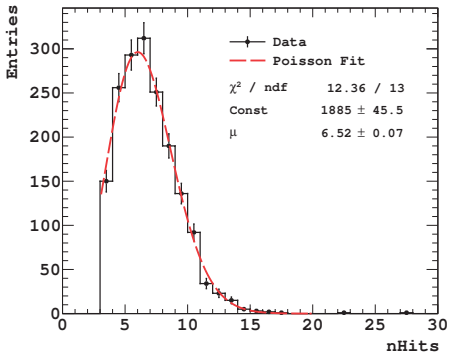

Figure 4.20: *Number of hits for tracks ($N_{\text{hits}} \geq 3$) in the fiducial region, fitted with a Poisson distribution.*

Using the mean value $\mu = 6.52$, from the Poisson fit shown in figure 4.20, the electron detection efficiency is 99.8% and the track detection efficiency is 95.5%. These efficiencies will improve further with all the pixels working and with larger drift-gap, particularly making the ability to fit tracks more robust.

4.6 Conclusions

We have demonstrated high performance in terms of efficiency, ionisation-electron position measurement, and tracking precision for a gaseous pixel detector. The efficiency to see at least one hit is 99.8%; the efficiency to record sufficient hits to fit a track is 95.5%. The hit-position resolutions given in table 5.4 are significantly improved over Timepix chip results in the drift direction, thanks to the fast front-end and high-resolution TDC in each pixel of the chip. As far as we are aware, this is the most precise gaseous detector to date for measuring the position of individual ionisation electrons. This leads to improved angular resolutions on fitted tracks, typically 2.5°, and on the drift position-resolution of track fits. The in-plane position resolution is 10 µm.

Further improvements are expected in Timepix3 which in addition has simultaneous ToT measurement, allowing corrections to the ToA to further reduce timewalk's

contribution to the z position error. With full-size chips, we can go to much larger drift distances giving in particular much better angular precision. The issues that led to almost 25% of the pixels being unusable have been addressed in Timepix3, giving a further improvement.

The performance is in line with expectations from predictions, indicating effects such as δ-rays and production of ionisation electrons far from the track are small compared to the diffusion and pixel-size limits to the hit resolution. We look forward to detectors based on the Timepix3 chip.

Chapter 5

Gaseous pixel detectors based on Timepix3 chip

" ... All we have to decide is what to do with the time that is given to us."

— Gandalf, Lord of the Rings (J.R.R. Tolkien)

The previous chapter describes the development of the first gaseous pixel detector featuring a high-resolution TDC (1.8 ns) per pixel. The performance of this prototype chip technology led to a significant improvement to the position resolution in the drift direction. Its successor, the Timepix3 chip, implements a faster front-end and a TDC per pixel with a better resolution of 1.56 ns, which reduces the timewalk. In addition, the simultaneous measurement of charge via time-over-threshold (ToT) and drift time via time-of-arrival (ToA) allows corrections to remaining timewalk effects, improving further the resolution. These facts encourage the realisation of gaseous pixel detectors based on the Timepix3 chip.

In 2015, we built two modules using Timepix3 chips. Due to a delay in the production of integrated grids (InGrids) on top of Timepix3 chips, we decided to proceed with an alternative approach, using a micromegas grid for the amplification. From the physics point of view, the working principle is similar. On the other hand, the major difference was that we had to manually place the grid on top of the chip, and the micromegas grid-hole pitch did not match the Timepix3 pixel pitch causing various problems discussed later.

The detectors were installed in the SPS/H8 beam-line at CERN and exposed to muon and hadron beams. The testbeam purpose was to exploit the capabilities of

Timepix3 chips to further improve the detector performance. This chapter describes the experiments performed and the analysis of the data obtained.

The main goal of the analysis is to take advantage of the simultaneous measurement of ToA and ToT and extract a correction for the remaining timewalk effects based on real data from a particle beam. Gaseous pixel detectors measure the creation positions of ionisation electrons in 3D. The measurement of the z-position though, is dominated by timewalk. In order to measure the timewalk, we use as an external reference a very precise track provided by a silicon telescope. The method is based on the residual of the telescope prediction with respect to the reconstructed z-position from the hit arrival time. This residual in time difference terms includes timewalk. The correlation then of timewalk and ToT enables the calculation of the corrected z-position. As a consequence, the tracking performance then benefits from the improved single hit resolution.

5.1 Detector description

5.1.1 Timepix3 chip

The Medipix consortium is active in the development of CMOS (130 nm) pixel readout chips of the so-called "Medipix family". By the end of 2013, the collaboration delivered the multi-purpose Timepix3 chip, [84]. The design was a common effort by CERN, Nikhef and Bonn University. It consists of a matrix of 256 × 256 of 55 µm square pixel cells covering a total area of about 2 cm^2.

The active area of the chip is organised in 128 double-columns. Each double column consists of 64 super-pixels or blocks of 4 × 2 pixels, figure 5.1. As a result the physical address of a pixel is defined by 3 numbers, the pixel number within a super-pixel, the super-pixel number within a double-column and the double-column number. For more details, see [98].

Every pixel contains a high resolution TDC with a resolution of 1.56 ns and a front-end with rise time less than 25 ns. Besides the improvement on the timing the main technological advance is the new acquisition mode. The chip allows the data-driven simultaneous recording of ToA and ToT. It can be operated also in frame based event counting mode. However in the context of this thesis the chip was always operated in the ToA and ToT mode. The readout can be data driven or frame based. The minimum useful threshold is ~500 e^- and the maximum readout rate is 80 MHits/s per chip.

5.1.2 Detector construction

By the end of 2014, the Timepix3 chip was already tested and the first few wafers were available. Therefore, the preparations for InGrid production runs were taking place already in the beginning of 2015. There were plans for production on a full wafer but also on a single Timepix3 chip. Unfortunately, the InGrid production was

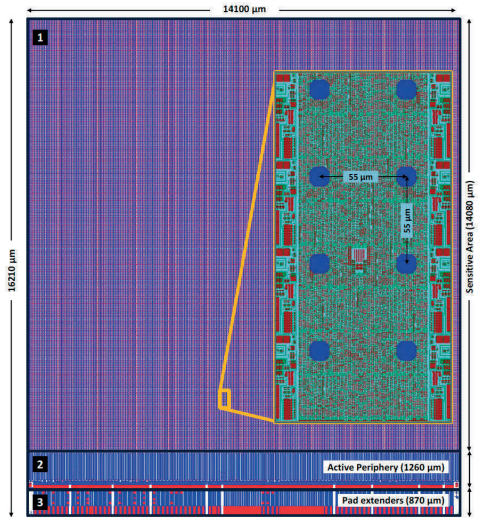

Figure 5.1: *Illustration of the Timepix3 chip indicating the dimensions. The chip is divided in three parts, 1) the sensitive area which contains the super-pixels (enlarged area), 2) the periphery of the chip and 3) the pad extenders. The picture is taken from* [98].

delayed for a few months. At that time a change of plan was made to prevent a significant deviation from the project timeline. We developed a gaseous pixel detector module using the Timepix3 chip with a micromegas grid for the amplification. In the context of this thesis we call this detector GasPix. The micromegas grid we use is loose and we have to place it manually on the grid. Figure 5.2 shows a cross section of the detector. In the following subsections we describe the steps followed during the detector assembly.

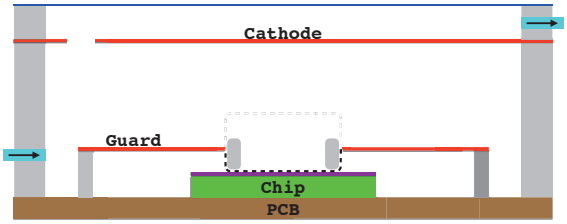

Figure 5.2: *A cross section of the detector (not in scale). The grid (dashed line) is glued to a frame and then mounted on the chip. The frame and the cage are made from the same material.*

Protection layer

Practically the detector assembly starts with a bare Timepix3 chip. As a first step the chip is covered with a protection layer against discharges. The deposition of the layer is performed in the Else Kooi Laboratory (EKL) at Delft University of Technology. The result of this procedure is a 4.3 µm thick layer of Silicon-rich silicon nitride (SiRN). Figure 5.3a shows a part of the chip plane covered with SiRN while figure 5.3b shows a cross section of the layer where the multistep deposition is clear. The resistivity of the layer is about 0.4 10^{11} $\Omega \cdot$ m. In general the quality of the deposition was very good with only a small number of defects. For more information about the measurement see the appendix.

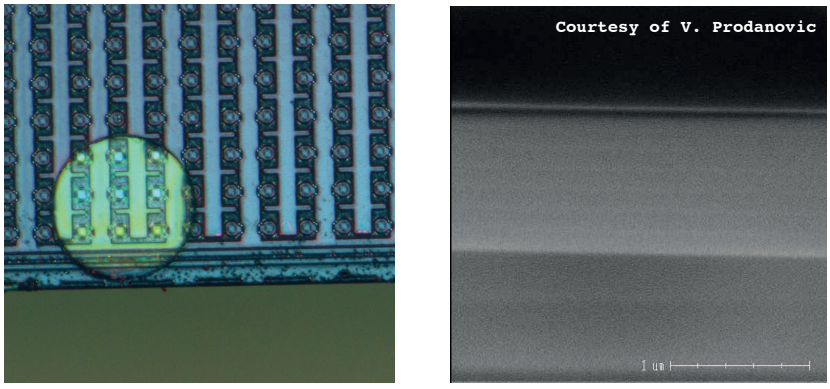

(a) (b)

Figure 5.3: *Pictures of the protection layer taken with an optical microscope on the left and SEM on the right. (a) Part of the top of the chip showing a defect in the cover: the SiRN did not cover the circular section. (b) Edge view of a sectioned chip layers of SiRN from successive depositions.*

Chip-board & wire bonding

After the deposition of the protection layer, the chip is glued with a thin double-sticky tape on a specially designed chip carrier board known as a Spidr-board. This is a mezzanine board carrying the power supply of the chip, DAC and ADC channels and Lemo connectors for trigger signals. There is also an FPGA Mezzanine Card (FMC) connector compatible with FPGA development boards used for the readout.

The Timepix3 chip is then wire bonded to the Spidr-board in the Nikhef cleanroom. Figure 5.4 shows the chip glued and wire bonded to the chip-board.

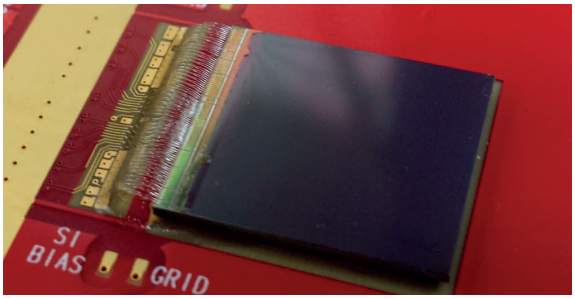

Figure 5.4: *A photograph of a Timepix3 chip mounted on the Spidr-board. The wire bonds are also visible.*

Guard electrode

In gaseous pixel detectors, the drift field is defined between the cathode and the amplification grid. In order to make sure that the electric field on the edges of the grid is uniform we make use of a guard electrode. A frame was glued onto the Spidr-board with the guard electrode, so that its laser-cut window lies above the Timepix3 chip. Figure 5.5 shows the guard electrode on the Spidr-board.

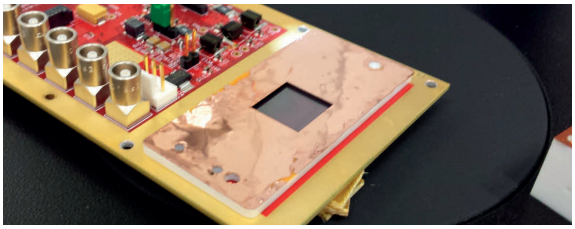

Figure 5.5: *A photograph of the guard electrode mounted on the Spidr-board.*

For the high voltage connection there is a dedicated pin on the Spidr-board. For this reason during the cutting of the guard a small hole above the pin is reserved for the connection. A thin copper wire is soldered on the pin and then attached to the guard with conductive glue. Figure 5.6 shows a photograph of the high voltage connection, taken with a microscope.

Micromegas grid

For the production of the grid a 5 µm thick copper plate on a kapton backing is used. Then, by chemical etching the plate is turned into a copper-grid supported by kapton pillars about 50 µm high. For more details, see [99]. The etching results in a structure of grid-holes with a pitch of 60 µm and a diameter of 35 µm. The pillars

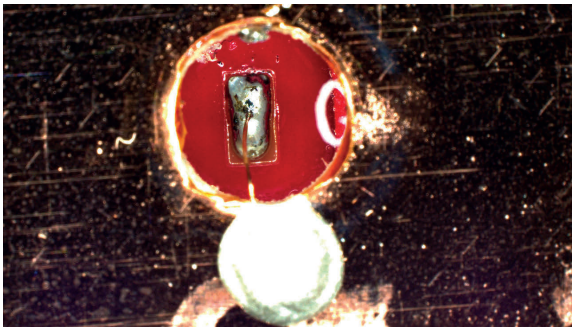

Figure 5.6: *The high voltage connection of the guard is done via a thin wire through a hole in the guard electrode.*

with a spacing of 1 mm make sure that the grid sits flat once the bias voltage is applied. A photograph can be found in figure 5.7

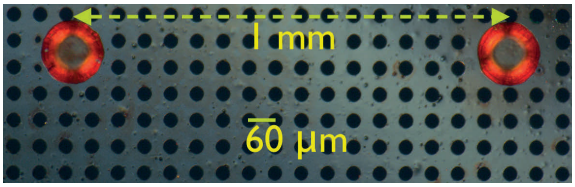

Figure 5.7: *A photograph taken with a microscope, zooming in a part of the grid at the bottom side. The bright circles are the pillars while the dark represent the grid holes.*

In order to mount the grid on the chip we used a frame made of a conductive plastic. The outer dimensions of the frame are slightly smaller than the inner dimensions of the laser-cut window of the guard electrode. The frame is glued on the top side of the grid with a tiny amount of epoxy. Then the whole structure is placed carefully on top of the chip. The grid-hole pitch is larger than the pixel pitch. Due to this mismatch the alignment of every grid-hole on top of a pixel is not possible. Care was taken to make the two grids parallel. A small amount of araldite on the outer side of every corner of the grid-frame keeps everything in place. The result is shown in figure 5.8.

The grid is biased by a direct contact with the guard. A small extension of the grid at one of its corners, is put in contact with conductive glue. We were aware that this might cause electric field deformations. However, it was decided to proceed with this solution and then correct offline for remaining effects. The telescope with its very precise measurement of the position of the track passing through the detector, enables such a correction.

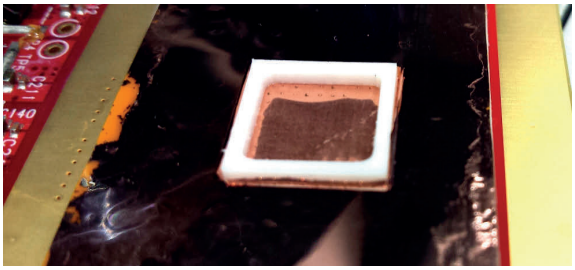

Figure 5.8: *Photograph taken after the assembly of the grid structure, bonded to the white frame, on top of the chip.*

Cathode

The cathode is a copper foil thin enough to allow the passage of low energetic incident radiation. It is supported on a flat plate of white conductive plastic apart from a circular hole above the chip. This plate sits on four precision machined walls. The base of the walls has an O-ring seal to the Spidr-board.

Gas chamber

A rectangular box with a clear mylar window is placed on top of the cathode and bolted to the Spidr-board, making a gas tight seal. A hole in the cathode support allows the supply of chamber gas, preventing the displacement of the cathode foil due to differential pressure. The gas is exchanged through a hole in the gas chamber walls. The total volume of the gas chamber is about 100 mL. Figure 5.9 gives a close overview of the chamber.

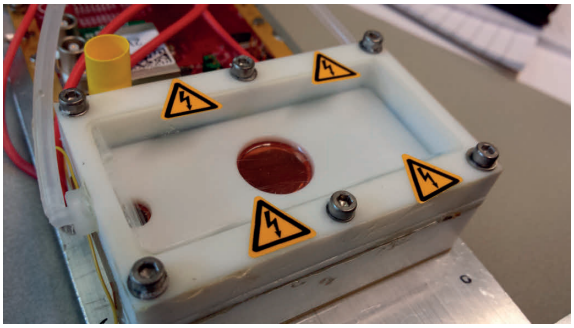

Figure 5.9: *The gas enclosure. The top lid (transparent) holds the gas. The cathode is visible in the centre.*

5.1.3 Readout

For the readout of Timepix3/Medipix3, the SPIDR readout system has been developed by Nikhef, [100]. The Spidr-board is connected through the FMC connector to a Xilinx VC707 evaluation board, see figure 5.10. This is the main board which hosts the electronics and the FPGA programmed to operate them. The presence of a 10 gigabit Ethernet link makes sure that the Timepix3 can be readout at its maximum rate i.e. 80 MHits/s per chip. An extra FMC connector enables the readout of two chips simultaneously (not used here).

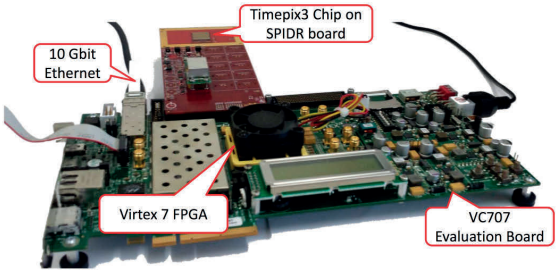

Figure 5.10: *A photograph of the Spidr readout. The picture is taken from* [84].

5.2 Experimental testbeam setup

In 2015, we built two modules using Timepix3 chips. Despite the problems of the mismatch between grid-holes and pixels, we could still investigate whether the timewalk correction based on particle beam data is feasible or not.

5.2.1 Beam

For about a week in the end of August 2015, we collected testbeam data at the H8 line of the Super Proton Synchrotron (SPS) at CERN. The H8 line delivers usually a high intensity beam of 180 GeV/c hadrons (60% protons/40% pions). Within a typical beam cycle of 36 s, two spills are present with a duration of 4.8 s each. The beam is quite focused with a maximum rate of about $1 \cdot 10^6$ particles / spill per cm^2. A muon beam is also possible, with some fine tuning of collimators and quadrupole magnets. The muon beam is broader with a rate of $5 \cdot 10^4$ particles / spill.

5.2.2 Telescope

In order to have an external track reference a Timepix3 silicon telescope was used, offered by the LHCb VELO upgrade group. The telescope consists of two arms, each of them carrying 4 stations. Between the arms there is enough space to mount the

device under test. Each telescope station is a Timepix3 hybrid pixel detector. The telescope is able to reconstruct extremely precise tracks with a pointing resolution of ~2 µm. For triggering purposes, before the first and after the last station, there are two scintillators covering an area of 1 cm^2 each. Figure 5.11 shows the experimental setup used.

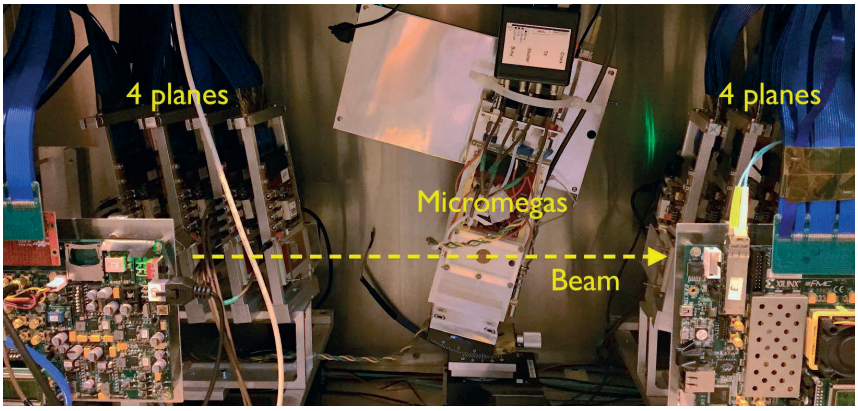

Figure 5.11: *Photograph of the experimental setup taken during the tesbeam.*

The readout of the telescope is based on the SPIDR system for the Timepix3 chip. This is extremely convenient since we integrate the device under test in the same readout. Thanks to the SPIDR's capability every track is recorded.

5.2.3 Detector Modules

For the testbeam two Timepix3 chips, W0012_H06 and W0017_I11, were converted into gaseous pixel detector modules. The mechanical structure of each module is identical. During the tests a goniometer provides a tilt angle about a horizontal axis. The goniometer sits on a rotation stage allowing rotations. The rotation stage sits on a translation stage allowing translations perpendicular to the beam. With this configuration the chip plane can be rotated to any direction allowing any desired track crossing angle to the chip. It was also possible to reconfigure the module to allow tracks parallel to the chip.

5.2.4 Gas and high voltage system

The chamber was flushed with a CO_2/DME (50/50) gas mixture. The gas mixture is premixed at Nikhef and stored in lightweight stainless steel bottles. DME is flammable, so in order to comply with the safety precautions at SPS stainless steel tubing was used, figure 5.12 left. For CO_2/DME the maximum pressure is 7.2 bar above which DME condensation could occur. With a moderate flow of 5 mL/min

the gas is sufficient for more than one week. Two mass flow controllers measure the flow at the input and output line as an extra precaution for gas leaks. A Labview program controls remotely the whole system and monitors the flow.

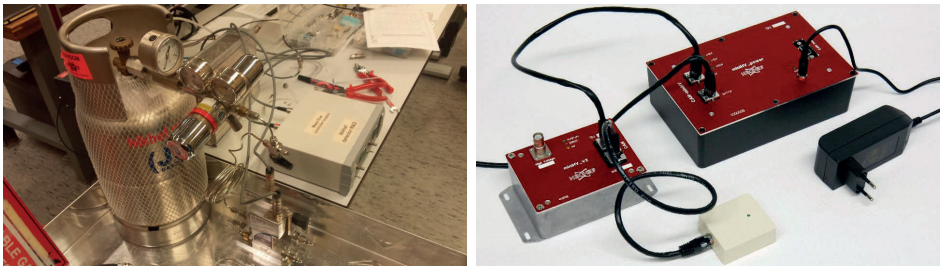

Figure 5.12: *A photograph of the gas system on the left and the miniHV power supply system on the right.*

In a gaseous pixel detector flushed with CO_2/DME, the typical values of electric fields vary from 0.5-3.0 kV/cm for drift and 100-150 kV/cm for amplification gap. A Wenzel power supply [101] provides the voltage for the cathode electrode. A miniHV V2, figure 5.12 on the right, is a compact high voltage system for low currents which supplies the voltage of the grid and the guard, [102]. Labview again is responsible for the control and monitoring of the high voltage system.

5.2.5 Trigger and DAQ

Two scintillators, before and after the telescope were used to provide external triggering. Figure 5.13 shows a simplified illustration of the trigger scheme. The DAQ system consists of four SPIDR boards for the telescope plus one for the gaseous pixel detector. As a result the functionality of a trigger logic unit (TLU) is essential. The TLU provides external clock and a "handshake" of the busy signals. In the beginning of a run the TLU synchronises the timestamps by sending a common t_0 to every board before enabling the shutter. In case of two coincident signals at the scintillators, a common external trigger signal is sent by the TLU to each Spidr-board. Each Spidr-board then records the arrival time of the trigger signal which is referred to as trigger timestamp.

Every SPIDR board is connected via an optical ethernet link to a PC which contains the DAQ software and stores the raw data. A central DAQ PC controls the whole DAQ sequence and monitors the telescope.

5.2.6 Run information

During the testbeam we have recorded plenty of data both with muon and hadron beams. We have operated the detector at various settings. In addition we have used

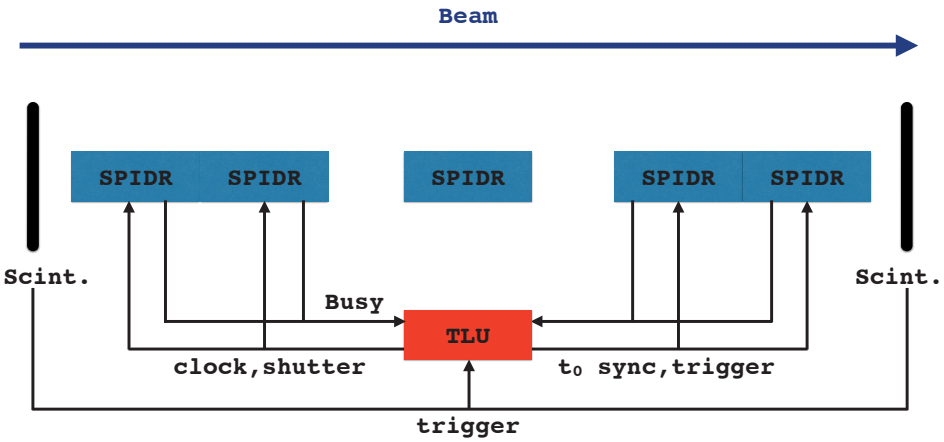

Figure 5.13: *The trigger scheme of the telescope. As an external trigger we use the coincidence of the two scintillators, before and after the telescope.*

two different configurations for the detector. In the beginning, the detector was placed in such a way in order to get inclined tracks which cross the chip. Later on, we have changed the orientation of the detector so that we get tracks parallel to the chip plane.

However, for the results presented in this chapter we are focusing on a run with inclined tracks with id 11093. The goniometer angle was set to 20°. We have collected about 100 k triggers with a hadron beam. For this run we were aiming for the following settings:

- A CO_2/DME (50/50) gas mixture.
- A drift field of E_{Drift} = 1 kV/cm.
- A grid voltage of V_{grid} = 550 V.
- A threshold of 500 e^-.

5.2.7 Sparks & chip failure

In the beginning of the testbeam the W0012_H06 module was mounted in the middle of the telescope. However, one corner of the grid was found loose after the transportation to CERN. As a result the module was replaced by the back up one, W0017_I11. The detector was running smoothly with muons at a relatively high gain for about a day. At some point, we switched to the high rate hadron beam. After 1 hour a large discharge was observed, figure 5.14 and the high voltage tripped off.

After the spark, the detector was still operational. The only effect was 2 dead double-columns, figure 5.15. For safety purposes we reduced the gain and continue running. About 12 hours later a second spark occurred which delivered lethal damage

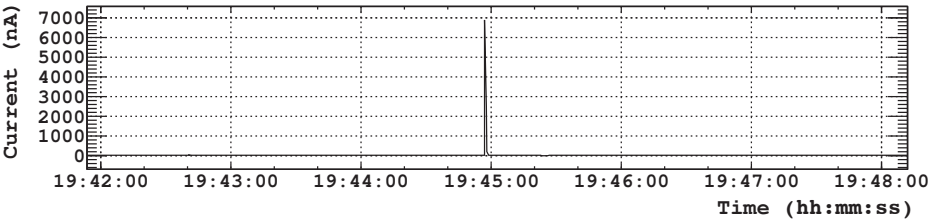

Figure 5.14: *An amplifier was coupled to the grid was used in order to monitor the sparks. This was connected via a* 1 nF *capacitor. The figure shows the monitoring of the grid current. The peak corresponds to a spark.*

to the chip. Most of the runs used for the analysis have been recorded in-between the two sparks.

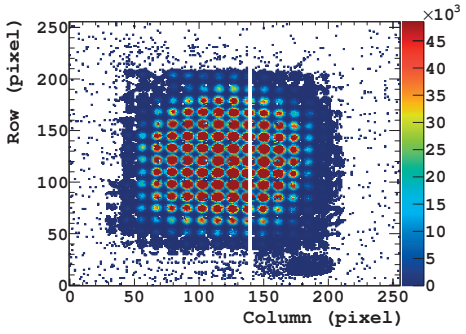

Figure 5.15: *Occuplancy histogram after the first spark showing the total number of hit in each pixel of the GasPix. The white vertical line corresponds to the dead double-columns.*

After the testbeam the grid was removed and the chip was inspected under the microscope. The damage caused by these sparks can be seen clearly in figure 5.16.

5.3 Analysis strategy

This section gives a brief description of the procedure that was followed for the analysis. Before the analysis the data reconstruction is performed in steps.

The raw telescope data is analysed using the standard LHCb software called Kepler which is a part of the Gaudi framework, [103]. This finds the trajectories of the beam particles and stores these as tracks. The signature of a track in each telescope station is a cluster of pixels hit and its cluster time. The mean cluster time

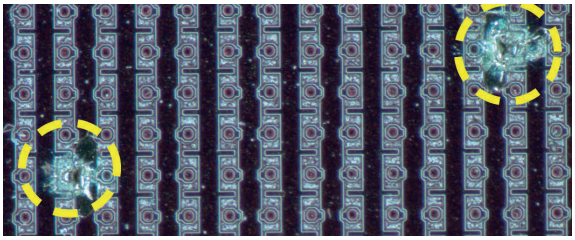

Figure 5.16: *Photograph of the chip surface taken under a microscope after the testbeam. The dashed circles highlight the area where the sparks occured.*

of all the stations is the track timestamp associated to each track. The output is a ROOT file [104] which includes all the information related to the telescope tracks.

The raw GasPix data is processed into events where each hit is associated to a scintillator trigger timestamp. All the hits within a time window around a trigger timestamp are assigned to an event. The output is an ASCII file which contains the event number, the trigger time and the associated hits. Then the data are stored in a ROOT tree. This event data is then paired with a telescope track using the two timestamps, and merged into a single file for further analysis.

An iterative alignment procedure gives corrections to hit positions and transformations of telescope tracks into the GasPix frame. Events with telescope tracks in a good fiducial volume are selected. Displacement of GasPix hit positions from the telescope tracks give residuals plots, which can be used to correct for things like drift field variations (subsection 5.7). With less distortions in hit positions, the alignment coefficients can be improved (section 5.8).

The procedure is very iterative: better alignment gives better hit position correction, which in turn gives better residuals for a better alignment. After all hit position corrections and alignment constants are stable, the residuals are plotted against ToT. This used to optimise the timewalk correction.

After applying all the corrections, including for timewalk, local track fits are made to the GasPix hit positions. The GasPix track resolution is extracted from the covariance matrix of the fit. We also compare the GasPix tracks to the telescope tracks confirming the covariance matrix method.

Figure 5.17 shows a simple sketch of the analysis steps. The procedure is presented as a linear path, however this path is not direct at all. It is a complicated iterative procedure in order to get a precise alignment which is crucial for the analysis. An improved alignment leads to improved residuals and as a result to a more precise correction. The next few sections describe in detail every step followed during the analysis beginning from the data reconstruction towards the final result.

Figure 5.17: *A block diagram of the steps followed during the analysis.*

5.4 Telescope analysis

5.4.1 Telescope hits

The telescope consists of 8 Timepix3 chips, bump bonded to 300 µm thick silicon sensors. The stations are slightly tilted aiming for the optimum resolution. A track crossing the telescope generates a cluster of hits on each station and a track segment in the GasPix. A dedicated software controls the data acquisition and provides online monitoring of basic quantities for each station and the detector under test. The so-called pixel hitmaps shown in figure 5.18 are used for the basic alignment of the GasPix with respect to the telescope stations.

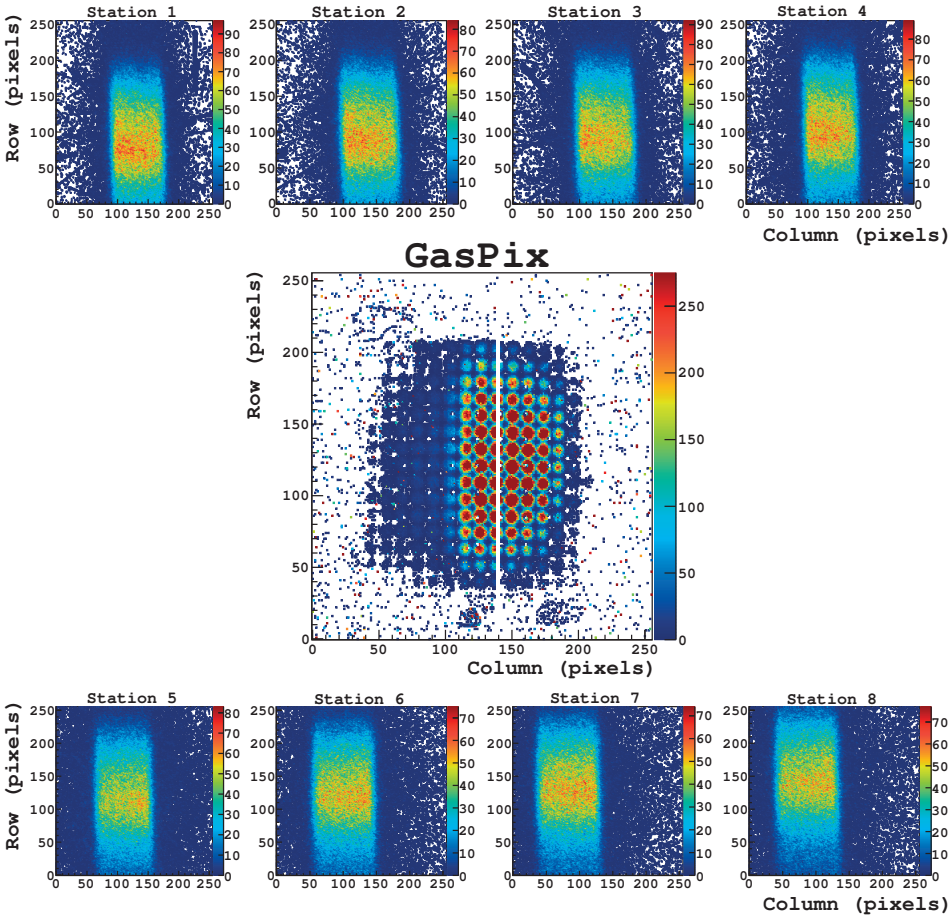

Figure 5.18: *Occupancy histograms of the telescope displaying the narrow hadron beam profile on each telescope station and the detector under test. Each histogram shows the total number of hits in each pixel. The upper four and lower four histograms correspond to the stations before and after the GasPix respectively. The middle one corresponds to the GasPix detector where the characteristic Moiré pattern is visible, and the dead columns after spark damage.*

5.4.2 Telescope frame

The telescope coordinate system is chosen in such a way that the origin corresponds to the first pixel of the first station i.e. pixel (0,0), figure 5.19. It is a right-handed coordinate system where the x-axis is pointing horizontally, the y-axis upwards and

the z-axis along the beam.

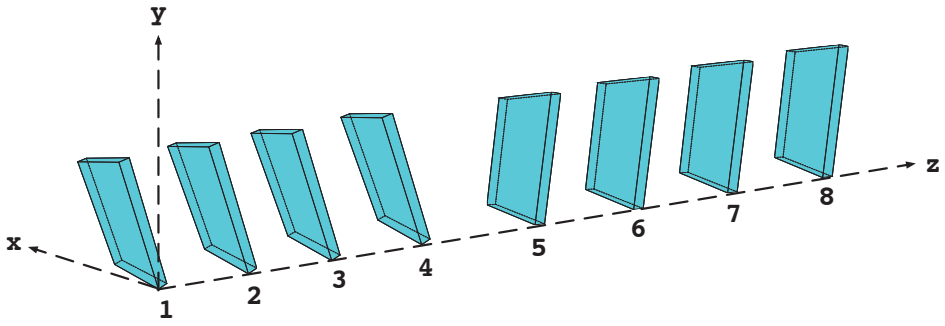

Figure 5.19: *Illustration of telescope stations and the global coordinate system. The stations of the right arm are rotated 180° with respect to the stations of the left arm.*

Each telescope station is slightly tilted about 9° around the x-axis and the y-axis. The distances between the stations within a telescope arm and the angles are always fixed. However, the distance between the arms was varied depending on the orientation of the GasPix module. After the alignment and the tracking within the Gaudi framework the output contains tracks defined in this frame.

The first station is positioned at $z = 0$. Then we measure the distance of each station accordingly. The positions are measured at the base of each module. Due to the rotation and the tilt this value is slightly different. Nevertheless, this is corrected during the alignment procedure. Table 5.1 shows the z position measured for each module, for the two orientations used during the testbeam.

5.4.3 Alignment and tracking

The Kepler program is used for the alignment and tracking for the telescope. It is based on the Gaudi framework developed by the LHCb collaboration. The input to the Kepler program is an ASCII file which contains the nominal alignment constants. We perform the alignment of each station using the Millipede method, [105]. Then, by using the updated alignment constants the tracking is performed. The typical minimum requirement for a track is the presence of a cluster in each station.

Every track is projected to the xz and the yz plane and fitted with a straight line minimising the χ^2. The final output is a ROOT file which contains all the information related to the tracks, i.e the track times, the slopes and offsets for the xz and the yz plane along with the covariance matrix and the χ^2 values. Figure 5.20 shows the distribution of χ^2 per degree of freedom on the left and the χ^2-probability on the right.

Table 5.1: *The z position of the telescope stations and the GasPix module. During the data taking two orentations for the GasPix module. We have recorded runs where inclined tracks cross the chip and runs where the beam is parallel to the chip plane.*

	Inclined tracks	Parallel tracks
Module	z_{pos} [mm]	z_{pos} [mm]
Station 1	0	0
Station 2	53	53
Station 3	95	95
Station 4	138	138
GasPix	283	327
Station 5	508	492
Station 6	546	530
Station 7	591	575
Station 8	636	620

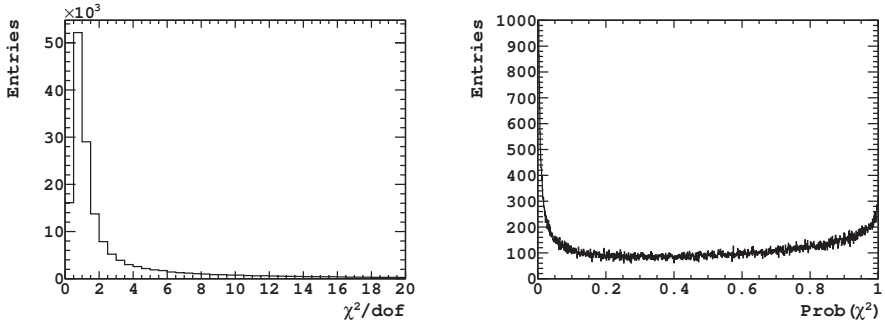

Figure 5.20: *On the left, the distribution of χ^2 per degree of freedom is peaking to 1.0 which confirms the fit quality. On the right, the χ^2 probability. For ideal detector with gaussian errors the distribution is a flat box. The peak below 0.1 is due to events where something goes wrong. Those events are typically omitted in the analyis rejecting events with a χ^2-probability lower than 0.05. The rise towards 1.0 indicates errors not fully understood or overestimated.*

5.4.4 Synchronisation with GasPix data

At this stage with the telescope data reconstructed and the GasPix data sorted into events, the next step is the synchronisation of the data. On the one hand there are hits in the GasPix detector associated to a trigger timestamp. On the other hand

there is a track with its timestamp. As a first check all time differences Δt between these two times are plotted. It is expected that telescope tracks and the GasPix events arrive close in time with a constant offset due to the cabling. Figure 5.21 shows the result for run 11093 giving a peak for the correct association.

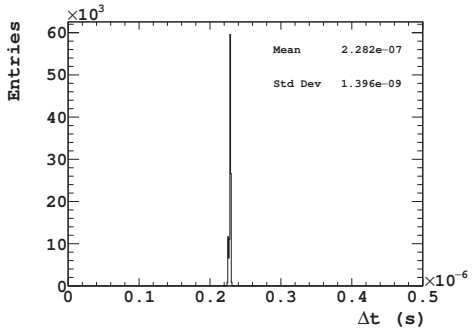

Figure 5.21: *Time difference between trigger time of the GasPix events and track time of the telescope tracks. The GasPix triggers arrive about 230 ns later with respect to the telescope track times.*

The two data sets are then merged by looping over the track timestamps looking for the a event trigger time within 230 ± 5ns. From figure 5.21 clearly random matches are extremely rare. The output is a merged ROOT file which stores telescope tracks and GasPix events.

5.5 GasPix hit analysis

5.5.1 Number of hits & Moiré pattern

Figure 5.22 shows the occupancy plots for the GasPix module in raw pixel units. The left plot corresponds to a run where inclined tracks cross the chip and the right one to a run where the tracks are parallel to the chip. The white areas on the out side are covered by the grid support frame and as a result we see only noise hits.

Instead of a uniform occupancy a Moiré pattern is observed. Such patterns occur when there is a mismatch between two overlapping grids, in this case the pixel matrix and the amplification grid. The colour varies from red which corresponds to areas where the grid-holes are well aligned to the pixels, to blue where the misalignment is maximum. In addition, there are also inefficient areas due to the supporting pillars every mm (white dots).

The natural consequence of the inefficiencies due to the Moiré pattern is that the number of hits per event drops by a significant amount. For example, a GridPix detector with the same specifications and operating in the same settings as in run

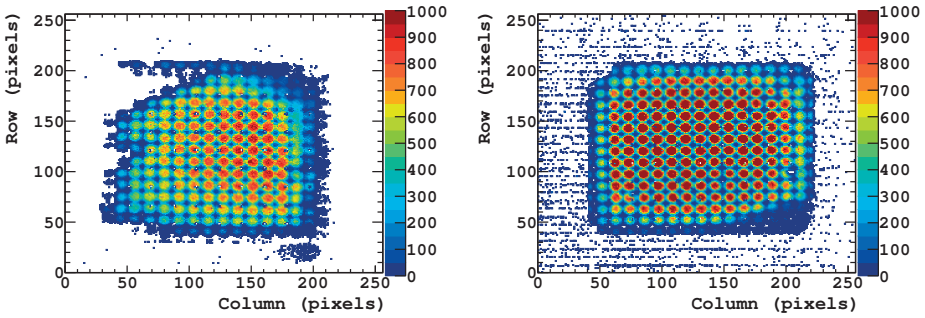

Figure 5.22: *The total number of hits in each pixel in the GasPix for inclined tracks that cross the chip (on the left) and for even illumination with tracks parallel to the chip plane (on the right).*

11093 would record on average 60 hits (ionisation electrons) per event. Figure 5.23 shows the distribution of the number of hits per event for run 11093. The expected number of hits drops to half of the expected value for a GridPix detector.

The other consequence is that the position of a hit corresponds to which grid-hole the electron drifted through rather than which pixel records the hit. This requires a mapping from pixel to grid-holes, given in the next subsection.

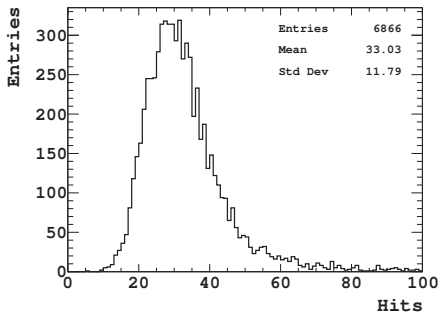

Figure 5.23: *Distribution of the number of hits per event for run 11093.*

5.5.2 Hits to position analysis

Each pixel hit of the Timepix3 chip is coded in a 48-bit word. Figure 5.24 illustrates the format of the data packet, when the chip is operated in ToA & ToT mode. The SPIDR readout adds a 12-bit coarse timestamp and sends the data packet to the

DAQ PC together with packets corresponding to triggers. The raw data is stored in a binary file as a stream of 64 bit integers. Some represent trigger timestamps and some represent hits. An event builder program reads the binary file looking for trigger words and groups related hits into events.

Figure 5.24: *The Timepix3 word which contains the physical address of the pixel hit, ToA and ToT. The word is sent to Spridr readout which adds a 12 bit coarse timestamp in the end.*

The output file of the EventBuilder is also an ASCII file where each line is an event containing the event number and the trigger timestamp followed by the associated hit-words in hexadecimal format. In the next step, event by event the information of every hit-word is decoded. A raw ROOT file is then created which stores the event number, the timestamp and the raw hit information. This consists of the column number, the row number, the hit arrival time and the time over threshold. During the analysis, the raw hit information is calibrated into a 3D hit position (x_h, y_h, z_h) in mm in the local detector frame. The following paragraphs describe the method.

In principle an ionisation electron drifts towards the grid, eventually enters a grid-hole and the pixel below registers the avalanche. When the grid and the pixel matrix, have the same pitch and are well aligned, the grid-hole position is identical to the pixel position; the pixel position would be given by the following equations:

$$x_p = d_p \cdot (n_c - x_0)\,, \tag{5.1}$$

$$y_p = d_p \cdot (n_r - y_0)\,, \tag{5.2}$$

In equations 5.1 and 5.2, n_c, n_r are the column and row numbers in pixel units which vary from 0 to 255 while $d_p = 55$ µm is the pixel pitch. These are shifted by $(x_0, y_0) = (127.5, 127.5)$ so that the origin of the local frame is the centre of the chip. In case of a mismatch though, the true hit position is the nearest grid-hole position. This is given as follows:

$$x_h = \mathrm{nint}\left(\frac{x_p - x_c}{d_g}\right) \cdot d_g\,, \tag{5.3}$$

$$y_h = \mathrm{nint}\left(\frac{y_p - y_c}{d_g}\right) \cdot d_g\,, \tag{5.4}$$

where $d_g = 60$ µm is the grid-hole pitch and (x_c, y_c) are the offsets in order to match the centre of the grid with the origin. In order to calculate these offsets

the residual of x_h, y_h with respect to the telescope track are plotted for the columns and the rows modulo 12[1]. The offset is given by the value which minimises the width of the residuals distribution. The method also allows offsets in the rotation angle. Special care was taken during the mounting of the grid so that the angle was consistent with zero. The best offset values are $(x_c, y_c) = (30, 30)$ µm

The reconstruction of z_h is based on the drift time given by

$$t_d = \left(t_{ar} - t_{tr} + t_{phase}\right) - t_0 \,, \tag{5.5}$$

$$z_h = v_d \cdot t_d \,, \tag{5.6}$$

where t_{ar} is the hit arrival time and t_{tr} is the trigger timestamp of the event. The phase shift correction t_{phase} depends on the column and is discussed later below. This value has to be shifted by t_0 so that the earliest hits are produced at $z = 0$. Then, the z_h in mm is the product of the drift velocity v_d and the drift time t_d. Later on we modify equation 5.6 to account for electric field deformations as we discuss in one of the next sections.

5.5.3 Drift time spectrum - t_0

The t_0 value is estimated from the uncorrected drift time spectrum. The estimation is done in such a way that the earliest hits are positioned at $z = 0$, corresponding to electrons created at the grid. Figure 5.25 shows the uncorrected drift time spectrum (eq. 5.5 with $t_0 = 0$) for run 11093. The sharp cut-offs at the extreme right and left edge of the spectrum reflect the time window used in the EventBuilder. Besides some background hits, the rising edge of the spectrum is clear. In order to position the earliest hits at $z = 0$, the rising edge is shifted to 0.

For even illumination with tracks with an ideal detector, the ionisation electrons are uniformly distributed in the drift volume. The main distortions in figure 5.25 are due to the narrow beam profile. Other causes of distortion include:

- Due to the track angle, particles might enter and leave through the side walls instead of cathode and chip respectively. In this case only a part of the track is registered.

- Electrons end up in the same hole. For electrons created very close to the grid, due to the low diffusion it is very likely that they end up in the same grid-hole. In this case the pixel sees only the first one.

- Electrons can attach to DME or impurities of the gas like O_2. The higher the electron is created the higher the attachment probability.

[1]Due to the mismatch we get a perfect match between a pixel and a grid hole every 12 pixels.

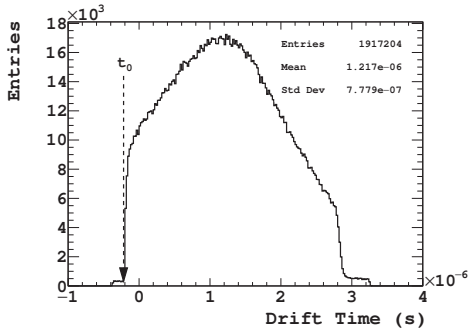

Figure 5.25: *Drift time spectrum. The distribution is shifted by t_0 in order to position the earliest hits, with the shortest drift times, at $z = 0$. The dashed line denotes the t_0 value.*

- Timewalk. Due to the gas gain fluctuations the pulse height varies. As a consequence, the time to threshold for low pulses is larger than the one for high pulses. This effect is timewalk and affects the whole spectrum and is responsible for a tail at high drift times.

5.5.4 Phase shift correction

In Timepix3 the clock is not generated synchronously for all the columns in order to reduce the peak power consumption. The clock generator was programmed to propagate 16 clocks with a uniform shift. Each one of these clocks is then sent to a group of double columns. This results in a column dependent shift in the arrival time t_{ar}. The phase group (0 - 15) corresponds to the lower 4 bits of the double column address of the hit word. In order to correct for this, we add a phase shift which is the column address times the step of the phase i.e. $1/16^{th}$ of a clock. Phase group 0 shifts $15/16^{ths}$ of a clock and phase groups 1 to 15 are respectively shifted 0 to 14 sixteens of a clock. For the bit manipulation of the hit word we use hexadecimal notation and the bit-wise operators. Equation 5.7 shows the phase shift added to the 64 bit hit-word.

$$t_{phase} = ((\text{hitWord} >> 45) - 0\text{x}100) \,\&\, 0\text{xF}00 \tag{5.7}$$

The GasPix detector, thanks to the time resolution of the Timepix3 chip, can clearly "see" this effect, which enables the correction offline. A possible way to do that, is to use tracks parallel to the chip long enough to spread over as many columns as possible, as in figure 5.22 one the right. A two dimensional histogram of the drift time against the column number is made. Figure 5.26 shows such a plot for the central part of the chip. In case of no shift or wrong shift added, jumps at the

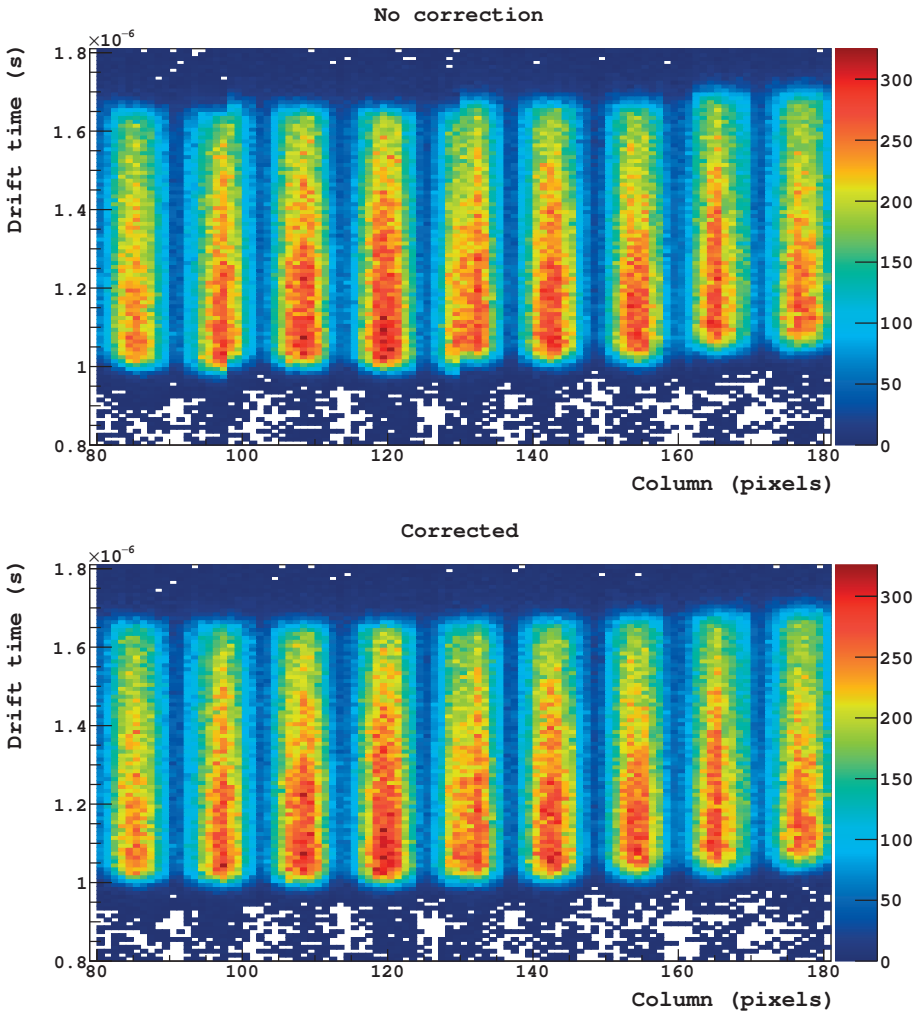

Figure 5.26: *Phase shift correction for timepix3 chip. The drift time spectrum is shown for each column on the x-axis, without (top) and with (bottom) phase shift correction. The uncorrected case shows jumps at certain columns numbers (e.g. 96, 128, 160), which dissapear by applying the correction. The vertical bands are due to the Moiré pattern. The U-shape at the bottom of each band is due to timewalk, since signals are bigger for well-aligned grid holes and so trigger earlier.*

drift time due to the phase shift are visible. By adding the correct value the jumps disappear.

5.5.5 Hit and event selection

Most events have only a single track. However a small fraction of events have other features such as noise hits, double tracks, δ-rays and nuclear interactions. Typically in such events, some hits are far away from the actual track and as a result generate tails in residual distributions. As a result these events are rejected during the analysis. In the final analysis, special care is taken so that only full tracks are taken into account.

The detector was typically operated at a threshold of $6\sigma_{\text{noise}} \approx 500\ e^-$ which is close to the minimum according to the design expectations. This was motivated as $5\sigma_{\text{noise}}$ to keep the noise hit ratio low, and an extra σ_{noise} to account for threshold mismatch after equalisation, [106]. The following subsections describe the track selection.

Noise and crosstalk hits

The threshold equalisation procedure described in subsection 3.4.5 takes care of variation in the performance from pixel to pixel. However, sometimes pixels keep firing constantly. In order to avoid that and keep the amount of data recorded at a reasonable level we had to mask about 1% of the total number of pixels.

Due to the threshold mismatch statistically quite often a noisy hit is registered. Usually noise hits possess low ToT values. By setting a lower limit at the ToT most of the noisy hits are rejected. For the analysis all the hits with ToT < 5 are rejected, figure 5.27.

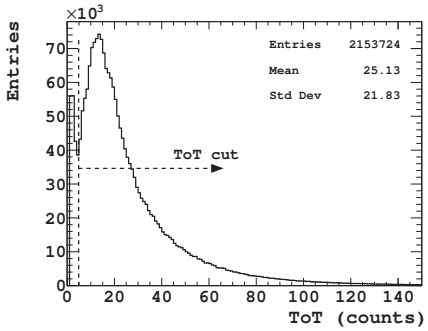

Figure 5.27: *A lower limit of 5 counts is applied on the ToT. All the hits below the limits are rejected.*

Cross-talk hits are hits occurring when the avalanche is shared by two or more

pixels. For our detector this is caused mainly by the misalignment between the grid-holes and the pixels. There are also cross-talk hits due to other reasons, like the charge spread because of the protection layer. The ToT cut mainly suppress the latter and reduces the amount of cross-talk hits due to micromegas misalignment.

Events with large number of hits

In the GasPix detector an event is considered as a track if the number of hits is larger than 3. For single track events, the mean number of hits observed (in run 11093) with the current detector settings is about 30, figure 5.23. Still, in a small fraction of the events a large number of hits is registered. This could happen for example when two or more particles cross the detector at the same time. Moreover a large number of hits is recorded in events where δ-rays are present or nuclear interactions with the surrounding material take place. Figure 5.28 shows examples of such events. An upper limit of 100 hits per track is set in order to reject events of this category.

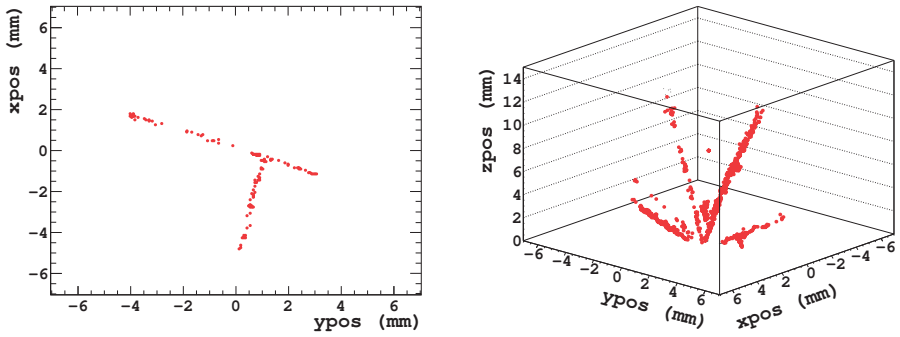

Figure 5.28: *Multi-track events are rejected with an upper limit to the number of hits per track.*

Fiducial volume

Due to the rotation of the detector with respect to the beam direction it is possible that some tracks cross only a part of the active drift volume, entering or exiting through a side wall of the active volume. This leads to short tracks which distort the drift time spectrum. In addition hits at the edges would have more distortions. In order to avoid edge effects or other systematic effects of the detector it is wise to use GasPix events which generate hits over the maximum drift distance. For the selection of the volume we use the telescope tracks. Figure 5.29 illustrates an example. The boundaries of the volume are adjusted in order to get tracks which cross the maximum drift distance or in other words GasPix events which give a

full drift time spectrum. Due to the narrow beam profile even with a significant reduction of the active volume down to 10%, we still get enough statistics for precise measurements.

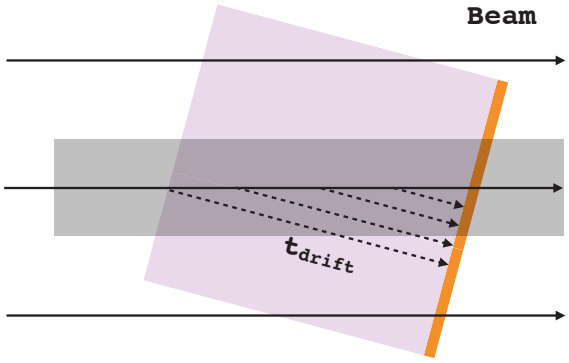

Figure 5.29: *A fiducial volume is defined in such a way that all tracks within the volume consist of hits along the full drift distance. All the tracks outside this volume are rejected.*

5.6 Telescope track transformation to GasPix frame

Telescope tracks and GasPix events are defined in different frames. We call the telescope frame the global frame and the GasPix one the local frame. We made the decision to transform the telescope tracks to the local frame of the GasPix detector.

5.6.1 GasPix frame

The GasPix detector position in the global frame is described by 6 parameters, three translations T_x, T_y, T_z and three rotations $R_x(\alpha)$, $R_y(\beta)$, $R_z(\gamma)$. For the GasPix frame the origin is the centre of the chip and not the pixel (0,0). The z axis is pointing along the drift direction, figure 5.30. These parameters are determined with an iterative procedure. This begins with the nominal values given in table 5.2 for run 11093.

The nominal values for both T_x, T_y is the value which moves the origin to the centre of the chip. For T_z this value depends on the orientation of the GasPix module. The nominal values for the rotations around the x, y axes are the reading values of the goniometer and the rotation stage respectively. The goniometer angle is always fixed at 15°. The rotation angle varies from run to run. Section 5.8 explains how more precise values are found in an iterative alignment procedure.

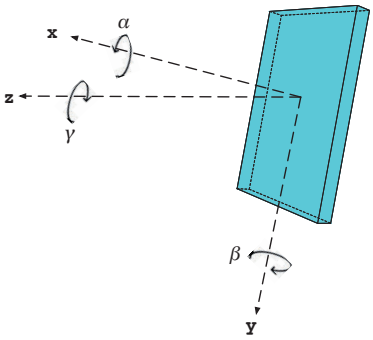

Figure 5.30: *Illustration of GasPix detector frame. The z axis is pointing to the drift direction which is the opposite of the the beam direction.*

Table 5.2: *Nominal values of the alignment constants for run 11093.*

Parameter	Units	Value
T_x	mm	7.04
T_y	mm	7.04
T_z	mm	283
α	rad	0.2618
β	rad	0.3491
γ	rad	0.

5.6.2 Transformation from global to local frame.

The beam tracks are approximately parallel to the z-axis in the telescope (global) frame. Figure 5.31 shows the slope distributions of the track projections to the xz and the yz plane of the global frame. Each track is transformed to the the local frame of the GasPix detector. In the local frame, due to the tilt angle and the rotation, in the GasPix detector the track is inclined. Figure 5.32 shows an event display. The blue line corresponds to the telescope track transformed to the local frame, and the red points to the GasPix event hits. The telescope track has been transformed to the local frame using the nominal parameters.

A telescope track in the global frame is defined as

$$\begin{aligned} x_{tr,gl}(z) &= b_X + m_X z\,, \\ y_{tr,gl}(z) &= b_Y + m_Y z\,, \end{aligned} \tag{5.8}$$

For the transformation, we pick two 3D points $P_i = (x_{tr,gl}(z), y_{tr,gl}(z), z)$ with $i = 1\,\text{or}\,2$ on the telescope track in the global frame. These are transformed to the

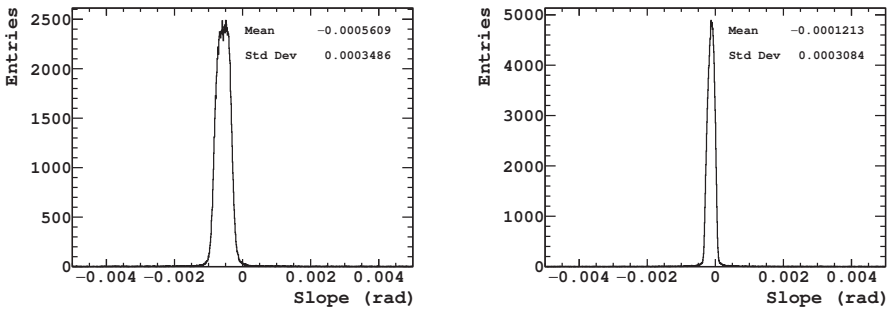

Figure 5.31: *The distribution of the slope of the telescope track projection at the xz plane (on the left) and the yz plane (on the right), in the global frame.*

local GasPix frame with

$$P_i^{'} = R_G \cdot P_i + T_G \,, \tag{5.9}$$

where $R_G = R_z(\gamma)R_x(\alpha)R_y(\beta)$ represent the rotations about z, x, y axes and the T_G the translations which complete the 3D transformation. The transformed points in the local frame are used to calculate the slope and the intercept of the track in the local frame,

$$m_X = \frac{p_{2_x}^{'} - p_{1_x}^{'}}{z_2^{'} - z_1^{'}} \,, \tag{5.10}$$

$$m_Y = \frac{p_{2_y}^{'} - p_{1_y}^{'}}{z_2^{'} - z_1^{'}} \,, \tag{5.11}$$

$$b_X = \frac{p_{1_x}^{'} z_2^{'} - p_{2_x}^{'} z_1^{'}}{z_2^{'} - z_1^{'}} \,, \tag{5.12}$$

$$b_Y = \frac{p_{1_y}^{'} z_2^{'} - p_{2_y}^{'} z_1^{'}}{z_2^{'} - z_1^{'}} \,. \tag{5.13}$$

Using the the equations above we can write the telescope track transformed in the local frame as

$$\begin{aligned} x_{tr}(z) &= b_X + m_X z \,, \\ y_{tr}(z) &= b_Y + m_Y z \,, \end{aligned} \tag{5.14}$$

For more details about the method, see [96].

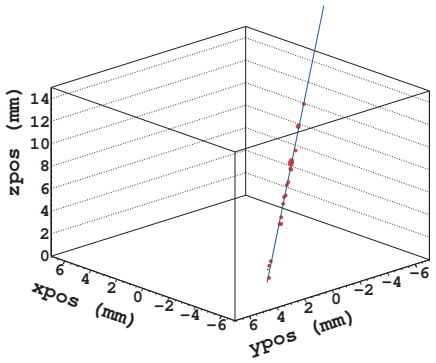

Figure 5.32: *An event display of the GasPix detector. The red points represent the GasPix hits. The blue straight line is the telescope track transformed in the local frame.*

5.7 Electric field deformations

For gaseous detectors in general, a good design of the electric field is important. For gaseous pixel detectors especially, due to the 3D reconstruction, a uniform drift field is a basic requirement. For the current detector it was well known in advance that this would not be perfect. One reason is that the grid and the guard are at different heights but the same potential which leads to deformed electric field on the edges of the grid. This is made even worse by charging up the frame above the grid. Distortions in the grid and the cathode also alter the electric field.

The central part of the chip should have an electric field which is highly uniform while the electric field on the edges is distorted. For the analysis we select tracks away from the walls in order to avoid the known distortions.

The first step before the correction is to check how significant the effect is. Each telescope track is transformed to the GasPix frame followed by the event filtering described in the previous section. Then for all the tracks within the fiducial volume a 2D dimensional plot of the residual of the hit position with respect to the telescope track versus the z coordinate z_h is made. The following equations define the residuals for the projections at the xz and yz planes.

$$r_{xz}(z_h) = \Big(x_h - x_{tr}(z_h)\Big)_{\perp}\,, \tag{5.15}$$

$$r_{yz}(z_h) = \Big(y_h - y_{tr}(z_h)\Big)_{\perp}\,. \tag{5.16}$$

The residuals in eq. 5.15, 5.16 represent the distance of a point to its projection on the line. With a uniform field one expects a horizontal band, with increasing

width as z_h increases due to diffusion. Figure 5.33 shows this histogram for run 11093.

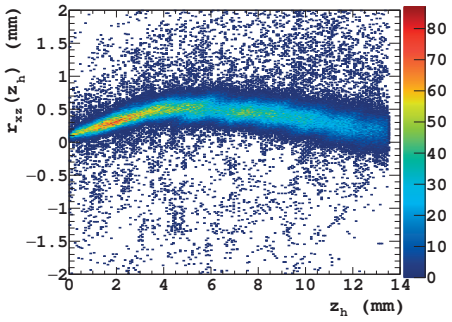

Figure 5.33: *The 2D histogram of the residual $r_{xz}(z_h)$ agains z_h using the nominal alignment constants. The banana-like shape indicates large electric field deformation.*

Instead of a horizontal distribution centred at zero, we observe large deviations (compared to the resolution) for low and high z_h. Given that these hits are far from the edges of the active volume, there must be some other cause. A close inspection of the field cage revealed a fold along the cathode directly above the grid. During the detector fabrication the fold was not present. On a later stage and in order to make the chamber gas tight, the screw keeping the chamber walls in place were adjusted. It could very well be that after the adjustment of the screws some surface tension on the cathode led to the fold.

Figure 5.34: *A photograph of the chamber component which holds the cathode. In the middle, the fold on the cathode which is responsible for the electric field deformations, is visible by eye.*

Unfortunately the presence of the fold was observed after the testbeam. This fold contributes also to the field distortion, however the major contribution is coming from the fact that grid and guard are at the same potential but different heights. As

a result the drift velocity is not constant in different areas of the detector. Therefore, the use of the drift velocity for the z-position reconstruction is not trustworthy. On the other hand, it is fortunate that there is a extremely precise track reference which does not suffer from distortions. This enables the calculation of a correction for the z_h which is independent of the drift velocity v_d.

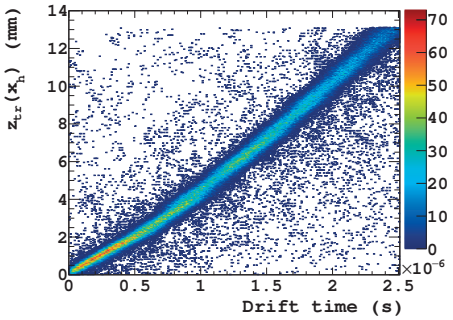

Figure 5.35: *The 2D histogram of the telescope predition against the drift time. For the ideal detector without electric field distortions the relation is linear.*

The telescope track is used to calculate z_{tr} which is the prediction for the z_h position of each hit. This is done separately for the xz and the yz projection of the telescope track (transformed in the local frame) and gives the nearest point to x_h and y_h. Then z_{tr} is plotted against the corresponding drift time of each hit. The result is shown in figure 5.35. Each slice of the drift time is projected to the y-axis and fitted with a gaussian. The profile histogram of the fitted means is fitted with a Chebyshev polynomial to give z_h' as a function of drift time:

$$z_h' = z_{tr} = \sum \mathrm{Cheb}\,(t_d)\,. \tag{5.17}$$

The slope of the distribution in figure 5.35 gives the drift velocity, which in our case is not constant. The drift velocity is given by the derivative of the eq. 5.17:

$$v_d' = \frac{\mathrm{d}}{\mathrm{d}t_d} \sum \mathrm{Cheb}\,(t_d)\,. \tag{5.18}$$

For better precision on the correction, the fiducial volume is divided in sub-volumes. This is done by the splitting the fiducial volume in blocks of (x, y) at the chip plane. Telescope tracks that cross the block of (x, y) are used in order to obtain the correction for the corresponding sub-volume. For each sub-volume the correction function is calculated and applied separately. The histogram of the residuals against the corrected z_h' is plotted. Figure 5.36 shows the result. This histogram meets the expectations for a detector without electric field deformation. Therefore the correction method is successful.

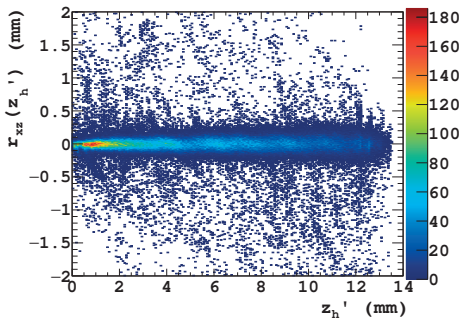

Figure 5.36: *The 2D histogram of the residual $r_{xz}(z_h^{'})$ against $z_h^{'}$ after the correction and the alignment procedure described in the next section.The shape is the expected one.*

The successful correction for the electric field distortions enables the proper alignment of the detector and the local track fitting. Without the correction the alignment would be systematically off which leads to a wrong estimate of the position. That would introduce huge systematics to the calculation of the timewalk correction and the resolution.

5.8 Alignment procedure

The alignment is based on the residuals with respect to the telescope prediction and takes into account only tracks inside the fiducial volume. Initially the nominal values of the alignment parameters are used, see table 5.2. Then with an iterative procedure, the alignment parameters are updated. A residual distribution centred at zero is an indication that the alignment is successful.

Due to the deformation of the drift field, the alignment is divided in two basic parts, the pre-alignment and the final alignment. The pre-alignment takes place before the correction for the electric field. During this part only T_x, T_y are evaluated in a few iterations in order to get a basic alignment of the GasPix module with respect to the telescope. This basic alignment shifts the fitted mean of the residuals to zero. Then the correction for the electric field takes place which gives $z_h^{'}$ according to equation 5.17. A successful correction for the electric field distortions enables the final alignment where all the alignment constants are evaluated.

The final alignment is performed in two stages. In the first stage, in a few iterations T_x, T_y are evaluated again together with γ, the rotation about the z axis as follows:

T_x The residual $r_{xz}(z_h^{'})$ distribution is histogrammed and then fitted with a gaussian. The mean parameter of the fit it used as an additive correction of T_x.

T_y The residual $r_{yz}(z_h')$ distribution is histogrammed and then fitted with a gaussian. The mean parameter of the fit it used to correct T_y.

R_z A 2D histogram of the residual $r_{xz}(z_h')$ against x_h is made. Each slice of x_h is then fitted with a gaussian. The mean of each slice is plotted against x_h and fitted with a straight line. The slope is used to perform a rotation about the z-axis.

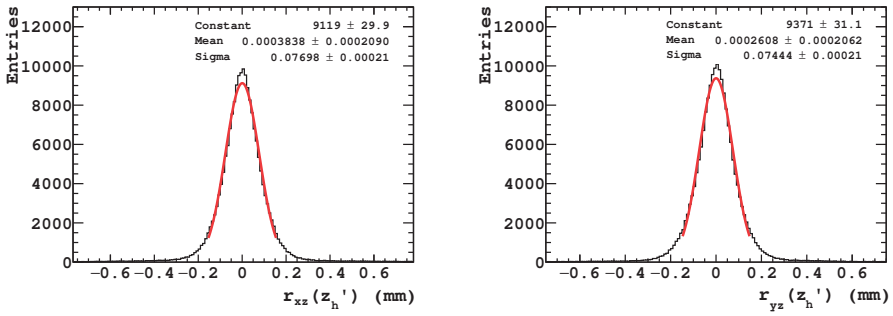

Figure 5.37: *The residuals used for the evaluation of T_x on the left and T_y on the right. The fitted mean is centred at zero indicating a successful alignment.*

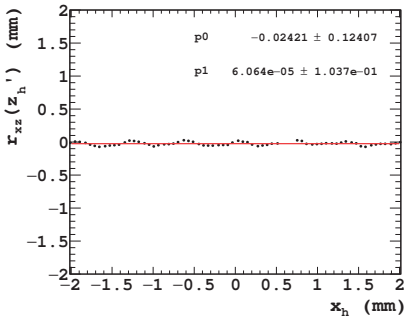

Figure 5.38: *The fitted mean of the residual $r_{xz}(z_h')$ for every slice of x_h for the central part of the detector. The histogram is fitted with a straight line. The slope is almost zero indicating a successful rotation about the z axis.*

Figure 5.37, shows the final result of the alignment for T_x on the left and for T_y on the right . Figure 5.38 shows the final result for the rotation about z axis. A successful alignment is obtained after a few iterations. Figures 5.39, 5.40 show the convergence graphs for T_x, T_y and γ respectively.

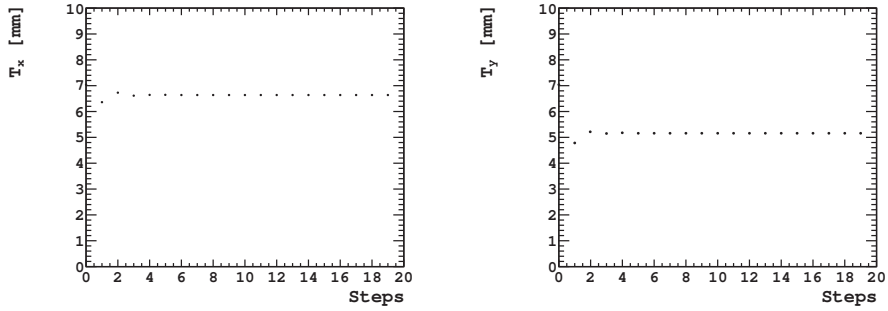

Figure 5.39: *Graph of T_x on the left and T_y on the right against the number of iterations. After a few iterations both values are converging to the final value.*

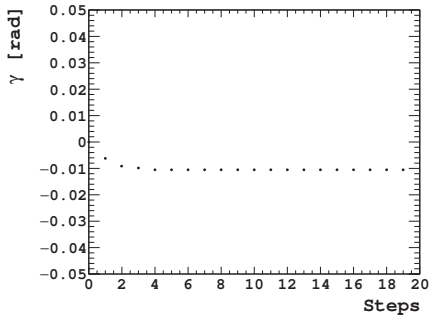

Figure 5.40: *Graph of the rotation γ against the number of iterations. After a few iterations the values are converging to the final value.*

In the second stage of the final alignment α and β are evaluated, which are the rotations about the x axis and the y axis respectively. The procedure is also iterative where:

R_x A 2D histogram of the residual $r_{xz}(z_h')$ against z_h' is made. Each slice of z_h' is then fitted with a gaussian. The mean of each slice is plotted against z_h and fitted with a straight line. The slope is used to perform a rotation about the x-axis.

R_y A 2D histogram of the residual $r_{yz}(z_h')$ against z_h' is made. Each slice of z_h' is then fitted with a gaussian. The mean of each slice is plotted against z_h and fitted with a straight line. The slope is used to perform a rotation about the y-axis.

The final results for the rotation about x and y axis are shown in figure 5.41. Figure 5.42 shows the convergence graphs for α and β.

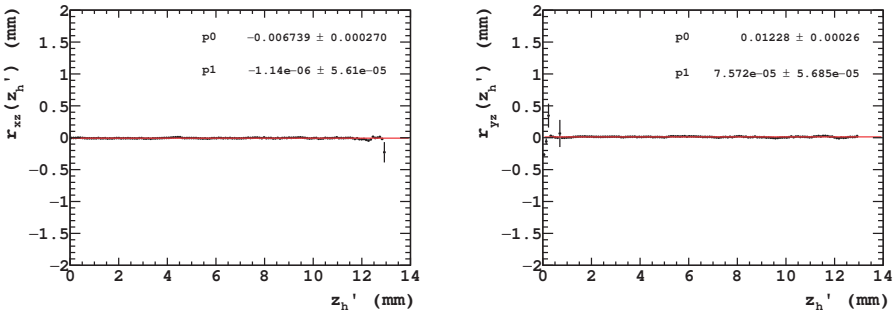

Figure 5.41: *The fitted mean of the residual $r_{xz}(z_h^{'})$ on the left and the $r_{yz}(z_h^{'})$ against $z_h^{'}$ residual on the right, for every slice of $z_h^{'}$. The flatness of the distributions indicates successful rotations about the x axis and the y axis.*

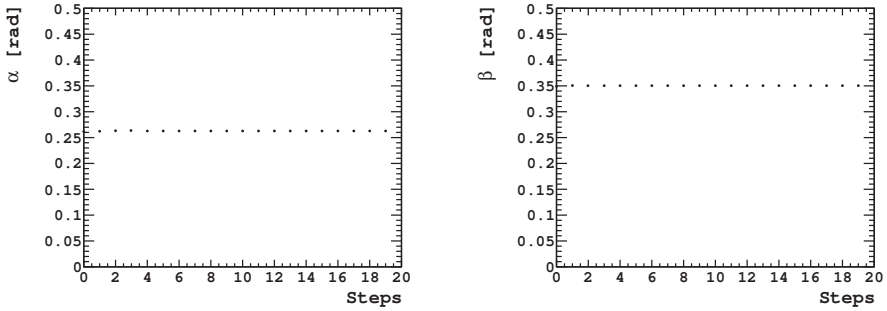

Figure 5.42: *The fitted mean of the residual $r_{xz}(z_h^{'})$ for every slice of x_h for the central part of the detector. The histogram is fitted with a straight line. The slope is almost zero indicating a successful rotation about the z axis.*

At a later stage the T_z parameter is evaluated with a trial and error method. The value of the parameter is varied until the width of the residual $x_h - x_{tr}(z_h^{'})$ is minimum. Figure 5.43 shows the result.

Table 5.3 summarises the final corrections obtained from the alignment procedure for run 11093. The corrections to the alignment constants are presented as differences from the nominal values shown Table 5.2.

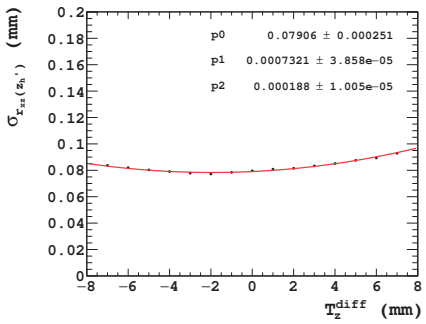

Figure 5.43: *The width of the $r_{xz}(z_h^{'})$ residual against the differential value of T_z. The minimum for the differential value is located to -1.94 mm. This value is used as an additive correction to T_z.*

Table 5.3: *Differential values of the alignment constants for run 11093.*

Parameter	Units	Value
T_x	mm	-0.402
T_y	mm	-1.881
T_z	mm	-1.94
α	rad	0.001
β	rad	0.0013
γ	rad	-0.01052

5.9 Timewalk correction

After the successful alignment of the detector the correction for the remaining timewalk effect is feasible. The correction is obtained from a 2D histogram of the residual r_{t_w}, given by eq. 5.19. This residual is plotted against ToT. Figure 5.44 shows the result,

$$r_{t_w} = \frac{r_{xz}(z_h^{'})}{v_d^{'}} \,. \tag{5.19}$$

Each ToT slice is then fitted with a gaussian. Figure 5.45 shows the fitted mean (on the left) and the fitted width (on the right) against the ToT. The mean value of each slice is the timewalk and is used to calculate $z_h^{''}$ which is the z position corrected for timewalk, eq 5.20. The correction is applied directly on the raw data i.e on the ToT and as a result there is no need to convert the ToT to charge,

$$z_h^{''} = z_h^{'} - v_d^{'} \cdot t_w(\mathrm{ToT}) \,. \tag{5.20}$$

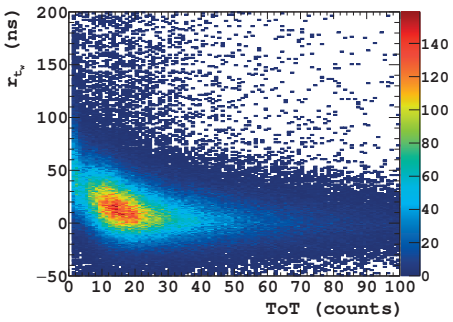

Figure 5.44: *The 2D histogram of the residual r_{t_w} against the ToT that is used for the timewalk correction. For low ToT counts, the residual distribution has a tail to the positive direction due to timewalk.*

The correction is largest at small values of ToT and asymptotic to zero at high values. Taking into account the ToT cut (described in Section 5.5.5) that we apply on all hits the timewalk range is up to 30 ns. The detector during the testbeam was flushed with a CO_2/DME (50/50) gas mixture. For the detector settings used at run 11093, the drift velocity is about 4.5-5.0 µm/ns. This results to a correction up to 135-150 µm, which in the end improves the intrinsic z position resolution.

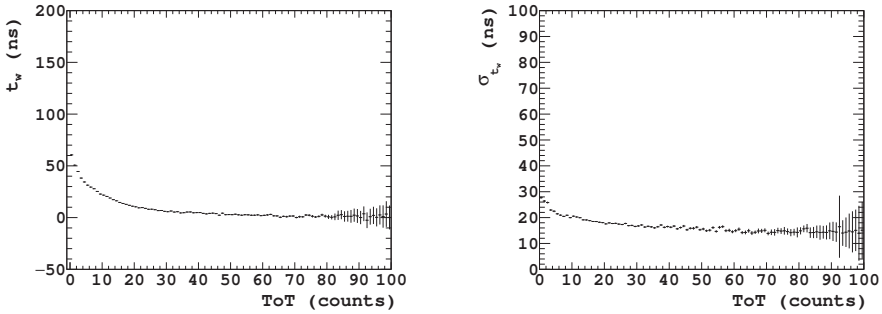

Figure 5.45: *The timewalk dependence on the ToT is plotted on the left. Each point represents the mean of the gaussian fit of each ToT slice. The width of each gaussian against the ToT is plotted on the right. The width is used as the corresponding timewalk error that is used in the analysis later on.*

The correction is in agreement with the design expectations, [106]. This is the first timewalk correction (to date) for the Timepix3 chip based on real data from a particle beam. Up to now all the previous attempts to estimate timewalk and correct for it were based on test pulse data.

5.10 Local track fitting

This section presents the results for the tracking performance of the GasPix module. In order to extract the detector resolution we fit the GasPix events at the local frame. For the fit procedure we use only events which comply with the selection criteria of section 5.5.5. Each event consists of 3D hits with coordinates given by $(x_h, y_h, z_h^{''})$ where $z_h^{''}$ is the ionisation height corrected for field deformation and timewalk, given by eq. 5.20. A straight line is fitted through the projections in xz, yz planes. For the fitting we use the same method, as in Chapter 4. The errors assigned to the hit positions are described below.

5.10.1 Hit position errors

The hit position reconstruction is described in Section 5.5. The x, y positions are given by eq. 5.3, 5.4 which place the hits at the centre of a grid hole. However the ionisation electrons are created uniformly above the grid-holes. This adds an rms error of $1/\sqrt{12}$ of the grid-hole pitch. An additional contribution to the error is coming from the transverse diffusion. Then, the error for x, y is given by eq. 5.21:

$$\sigma^2_{x_h} = \sigma^2_{y_h} = \frac{d_g^2}{12} + D_T^2\, z\,, \tag{5.21}$$

where d_g is the grid-hole pitch and D_T the transverse diffusion coefficient.

Along the drift direction, electrons are also created uniformly. For the reconstruction of the ionisation height $z_h^{''}$ of a hit we use the ToA value recorded by the pixel. The information is digitised and each hit is assigned to a time bin. The width of the time bins depends on the time resolution of the TDC. The contribution to the error is the $1/\sqrt{12}$ of this width multiplied by the drift velocity. Additional contribution to the error are coming from the longitudinal diffusion and the timewalk. Thus, the error in z is given by:

$$\sigma^2_{z_h^{''}} = \frac{(\tau_f\, v_d')^2}{12} + D_L^2\, z + (v_d'\, \sigma_{t_w}(\mathrm{ToT}))^2. \tag{5.22}$$

In eq. 5.22, τ_f = 1.56 ns which is the TDC resolution for the Timepix3 chip. The drift velocity is given by eq. 5.18. The timewalk error which depends on the ToT value is obtained from figure 5.45 (on the right). This plot includes also the contribution of diffusion which is subtracted.

The error on z is plotted against $z_h^{''}$. By fitting the data points with eq. 5.23 we extract the longitudinal diffusion coefficient. Figure 5.46 shows the result.

$$\sigma_z = \sqrt{k^2 + D_L^2\, z}\,. \tag{5.23}$$

In eq.5.23, the offset k includes the errors of the time bin and the timewalk. From the fit we obtain k = 36.18 µm and D_L = 29.55 µm/$\sqrt{\mathrm{mm}}$. For cold gases like

Table 5.4: *The hit position resolution at various ionisation heights.*

z (mm)	σ_x (µm)	σ_y (µm)	σ_z (µm)
0.0	17.3	17.3	36.2
1.0	34.3	34.3	46.7
2.0	45.2	45.2	55.3
5.0	68.3	68.3	75.4
10.0	95.0	95.0	100.2

CO_2/DME the diffusion coefficient for the transverse and the longitudinal diffusion is approximately the same. Hence, in the analysis we use $D_L = D_T = 29.55$ µm/ $\sqrt{\text{mm}}$.

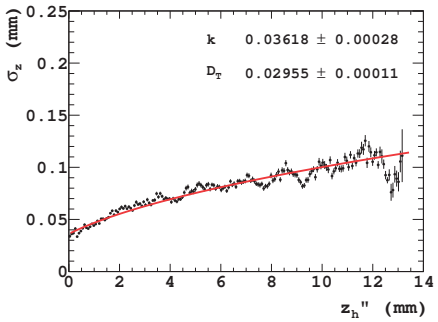

Figure 5.46: *The error on the z position as a function of the ionisation height z''_h. The data points represent the width of the residuals. The longitudinal diffusion is extracted by fitting the data point with eq. 5.23.*

The single hit position resolution in 3D is defined in terms of a voxel. The electron could have been created anywhere within the voxel. Table 5.4 shows the size of the voxel at various ionisation heights. The results can be compared to the ones from Chapter 4. The major difference is the improvement of the z resolution thanks to the timewalk correction.

5.10.2 Track position & angular resolution

The straight line fit is performed with York's method to the track projections at the xz and the yz plane. The fitting routine returns slope and intercept for both planes, (b_x, m_x) and (b_y, m_y), their covariance matrix and the x^2, as described in [96]. Figure 5.47 shows the positional and angular errors obtained from the covariance matrices for run 11093. The average error on the position for the xz and the yz planes is about 12.6 µm and 11.5 µm respectively, similar to what have been observed in

Chapter 4. For the angular error the average error is about 4.4 mrad and 4.3 mrad. This is a factor 10 improvement thanks to the larger drift gap and the time-resolution of the Timepix3 chip.

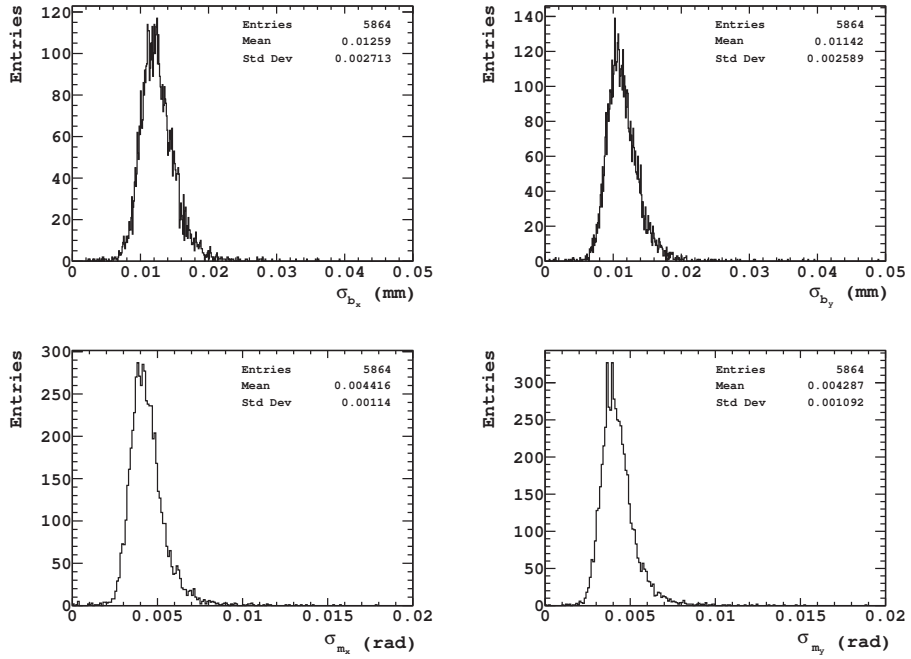

Figure 5.47: *From to top to bottom, the positional and angular errors obtained from the covariance matrices of the straight line fit for the xz plane and the yz plane, from left to right.*

By using the positional and angular errors obtained, the set of the fundamental track-resolution parameters of the detector can be derived as in Chapter 4. Due to the symmetry of the detector for x and y direction the track resolution is expected to be the same. Figure 5.48 shows the result.

The fundamental resolution for x and y is about 10 µm which is similar to what has been observed before in [92]. However more intriguing is the result for the resolution along the drift direction. Figure 5.49 shows the result obtained without the timewalk correction on the left and after the correction on the right. Before the correction the resolution averages to 32 µm. Thanks to the timewalk correction the fundamental resolution for z drops for to 19 µm. The fundamental set of track resolutions obtained is given by eq. 5.24:

$$(\sigma_{T_x}, \sigma_{T_y}, \sigma_{T_z}) = (10, 10, 19)\ \mu\text{m}. \tag{5.24}$$

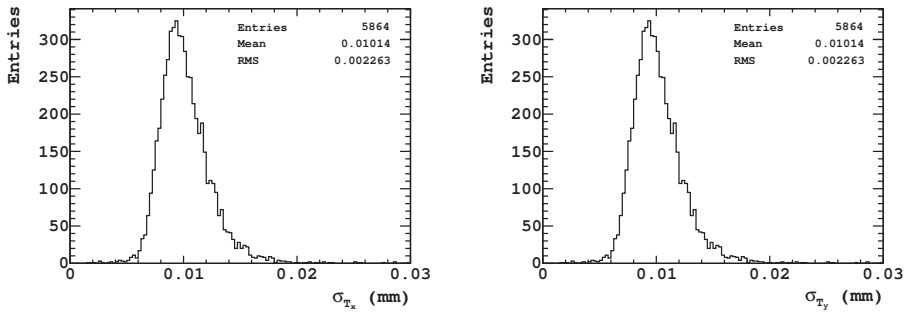

Figure 5.48: *The fundamental track position resolution for x on the left and y on the right. The resolution is exactly the same due to the symmetry of the detector.*

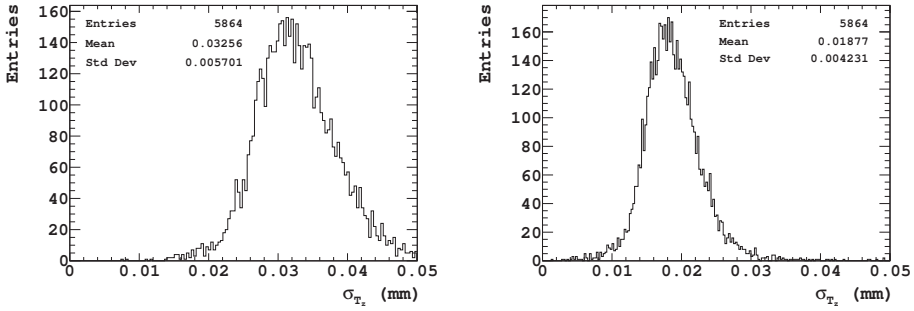

Figure 5.49: *The fundamental track position resolution along the drift direction before the timewalk correction on the left and after the timewlk correction on the right.*

Thanks to the Timepix3 chip which enables the timewalk correction, the improvement with respect to detectors based in Timepix and Gossipo2 chips is significant. Figure 5.50 shows the confidence levels and the x^2 per degree of freedom. The flatness of the confidence levels and the peak around one, confirm the quality of the fit.

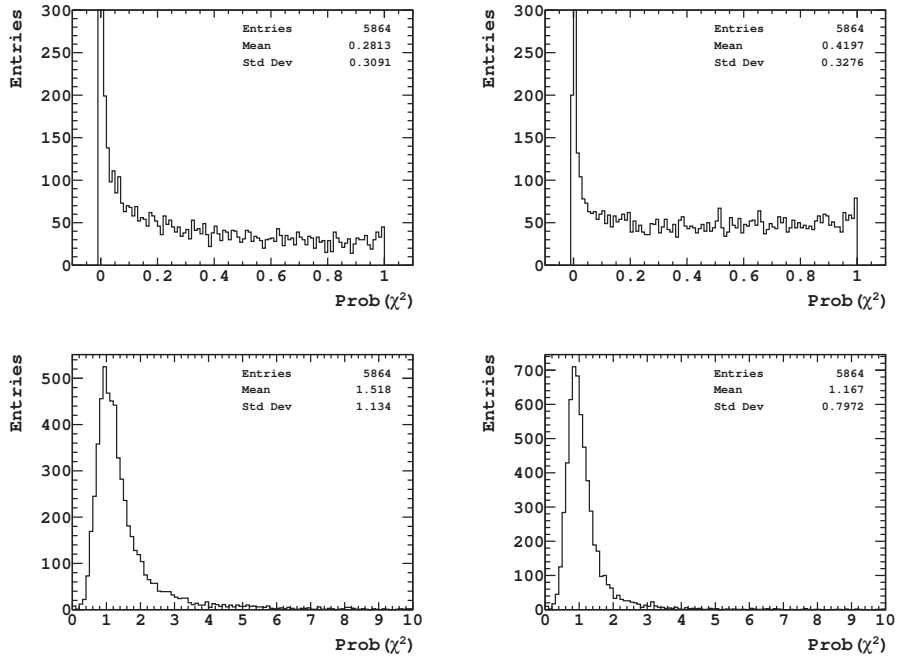

Figure 5.50: *On the top the confidence levels for the xz plane (left) and the yz plane (right). On the bottom the distribution of the χ^2 for xz,yz on left and right accordingly. Both confirm the quality of the fit.*

5.11 Resolution check using the telescope

After analysis procedure that was described in the previous sections, including the corrections for field distortions and timewalk, gives the track resolution using the covariance matrix. However the track resolution can be derived also using the telescope tracks transformed in the local GasPix frame. This is done by plotting the residuals of the telescope track offset and slope with respect to the offset and slope of the fitted track in the GasPix detector. The resolution obtained with this method is the total track resolution and includes the GasPix resolution, the telescope pointing resolution and the multiple scattering. Figures 5.51, 5.52 show the results obtained.

These plots clearly show that there are some remaining systematic errors. The experiment and the analysis performed with a very difficult detector mainly due to the electric field deformations. Even with the correction applied, the remaining systematic effects show up in these track residual plots. Both plots are not centred at zero and have a width larger than the resolution obtained with the covariance matrix method. Therefore, the resolution that we achieved in the previous section, is

the resolution that can be achieved with a constant, parallel electric field. What we have done is to correct the worst of the distortions, and find the random error limit to the track resolution.

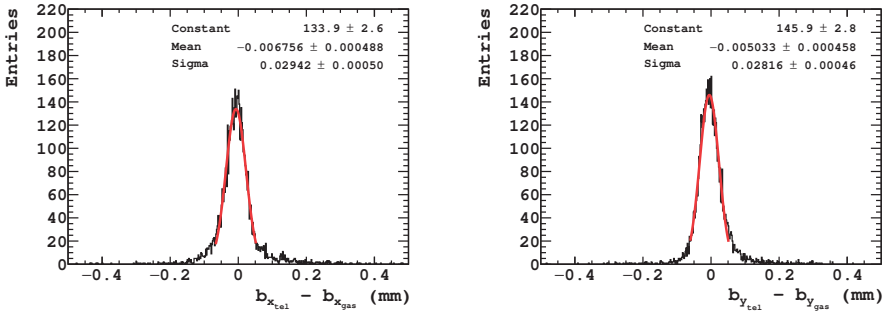

Figure 5.51: *The distribution of the residuals of the telescope track offset (at the centre of gravity) with respect to the offset obtained from the fitted track in the GasPix detector.*

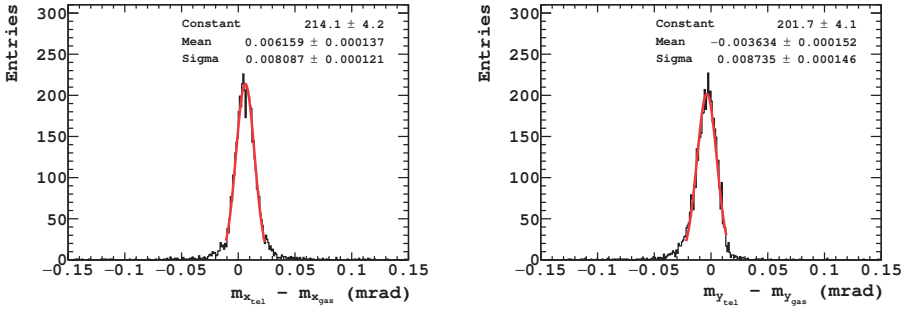

Figure 5.52: *The distribution of the residuals of the telescope track slope with respect to the slope obtained from the fitted track in the GasPix detector.*

5.12 Conclusions

We have developed gaseous pixel detectors by mounting a micromegas amplification grid on top of the Timepix3 chip. The detectors were tested in partible beams at SPS/CERN. As an external reference we have used a silicon telescope. During the testbeam period we have successfully demonstrated the capabilities of the chip and the readout system by recording all tracks.

The Timepix3 chips thanks to its fast front-end and the simultaneous measurement of ToA and ToT allows the correction for the timewalk effect. We present the timewalk correction for the Timepix3 chip obtained with the detector operating at the minimum threshold $\sim 500\ e^-$. Several attempts were made in the past in order to correct timewalk with test pulses, for example in [107]. However, this is the first correction based on real data recorded in particle beams.

By applying the timewalk correction on the data, we achieve significant improvement to the position resolution along the drift direction with respect to Chapter 4. We present an in-plane position resolution of 10 µm and 19 µm for the drift direction. We also present an improved angular resolution, about 4.5 mrad thanks to larger drift gap. Table 5.4 shows the single hit position resolution for various drift heights. However these results are the resolution that can be achieved with a parallel electric field. Due to the remaining systematics, the results obtained find the random error limit to the resolution.

The performance of a GridPix detector with a proper guard and a parallel electric field would be improved. The distortions would be very much reduced and only the timewalk correction would be needed. In addition, a high quality InGrid with no mismatch between grid-holes and pixels would improve further the performance. There would be twice as many hits, improving position and angular track resolution by $1/\sqrt{2}$ as it was demonstrated in [108]. The dependance of the resolution on the number of hits was demonstrated also in chapter 4.

In the future, special care has to be taken for the protection of the chip against discharges. The SiRN layer that was deposited on the chip did not offer sufficient protection to the chip. The main objective for the future would be the development of spark-proof gaseous pixel detectors. This is the research topic of the next chapter.

Chapter 6

Towards spark-proof GridPix detectors

"From a tiny spark may burst a mighty flame."
— Dante Alighieri

By its nature the GridPix detector has to cope with discharges produced by highly ionising phenomena like delta electrons (δ-rays) and by the stochastic nature of the gas gain. Already from the very early tests on GridPix detectors it was perceived that the discharges may create lethal damage on the chip. A readout chip without any protection becomes non-functional within a few hours of operation. Hence the sensitive electronics of the chip have to be protected.

A common way to protect the anode and the readout electronics of micromegas-like gaseous detectors is to deposit a thin highly ohmic layer directly on top of the readout plane. Depending on the readout scheme used, the patterning of the layer is also possible in order to form resistive strips or pads [109–111].

For GridPix detectors due to the high segmentation of the pixel chip the patterning is not straightforward and therefore the whole chip surface is covered by the protection layer. Studies that were performed in the past [78,79] show that a 4 µm thick protection layer made of silicon-rich silicon nitride (SiRN) would be sufficient to protect the chip.

Despite the excellent tracking performance, the current technology is not sufficient in protecting the chip from discharges especially in high rate hadron beams (see chapter 5). The protection offered by the layer strongly depends on its uniformity. Defects in the layer evolving during the deposition are the weak point of the current technology. Discharges occurring through a defect release a large amount of electrical energy ending up on the chip.

This chapter presents a systematic study of the performance of spark protection layers on dummy and real chips. For this purpose a dedicated spark-setup has been developed. The first part of the chapter presents studies on dummy chips focusing

on the investigation of new candidate materials for the protection layer. The second part presents results from real InGrids that where exposed in a hadron beam at SPS at CERN.

6.1 Discharge quenching

Section 2.6.3 describes the formation of a streamer which leads to discharges in gaseous detectors when the size of the avalanche exceeds the Raether's limit [65]. The discharges occur naturally in the gas and cannot be fully avoided. The role of the protection layer is to prevent that the large amount of charge damages the pixel electronics. Therefore it has to contribute to the quenching of the discharge.

The successful quenching of a discharge by using a resistive layer is based on the same mechanism which provides sufficient spark-proofing in the resistive plate chamber (RPC), [112]. The RPC is a parallel plate gaseous chamber where both electrodes are made of a material with high resistivity. In case of a spark, a large amount of charge is released on the layer which in turn is charging-up. As a result there is a local potential drop across the layer and hence a drop to the amplification field strength. Therefore the gas gain is reduced which leads to quenching of the discharge.

The performance of the protection layer depends on its specific resistivity. The proper value for the resistivity is a compromise between good discharge quenching and a rapid drain of the charge and hence the recovery of the electric field. A too high resistivity would lead to increased charge-up effects limiting the rate capability and the efficiency of the detector. For GridPix detectors used in high rate applications $\mathcal{O}(1\ \text{MHz cm}^{-2}\text{s}^{-1})$ a rough estimation for the desired resistivity value is $10^9\ \Omega \cdot \text{cm}$. For a detailed discussion on signal induction on resistive planes see references [113–115].

6.2 Dedicated setup for spark-testing

The previous experience within the context of this thesis and [79,96] from lab-measurements and testbeams with GridPix detectors shows that the spark protection layer needs further improvement in order to make reliable detectors for a long term use. This led to the realisation of a dedicated setup where we can produce sparks and test the performance of the protection layer on dummy or real chips.

The design of the setup was done is such a way that up to four chips without InGrid can be installed (or uninstalled) easily. The setup is based on a printed circuit board (PCB). The chips are kept into place with a double sticky tape on the PCB. For the amplification, a micromegas grid is pressed on top of each chip by silicon rubber wires. Hence the grid is not attached to the chip which enables the rapid exchange of chips. For each micromegas there is a separate channel providing the high voltage.

A frame with gas inlet and outlet supporting a common cathode provides an enclosed gas volume. The frame is fastened directly on top of the PCB with 6 screws, while an o-ring in-between makes sure that the chamber is gas-tight. A schematic of the design of the spark test-chamber is shown in figure 6.1.

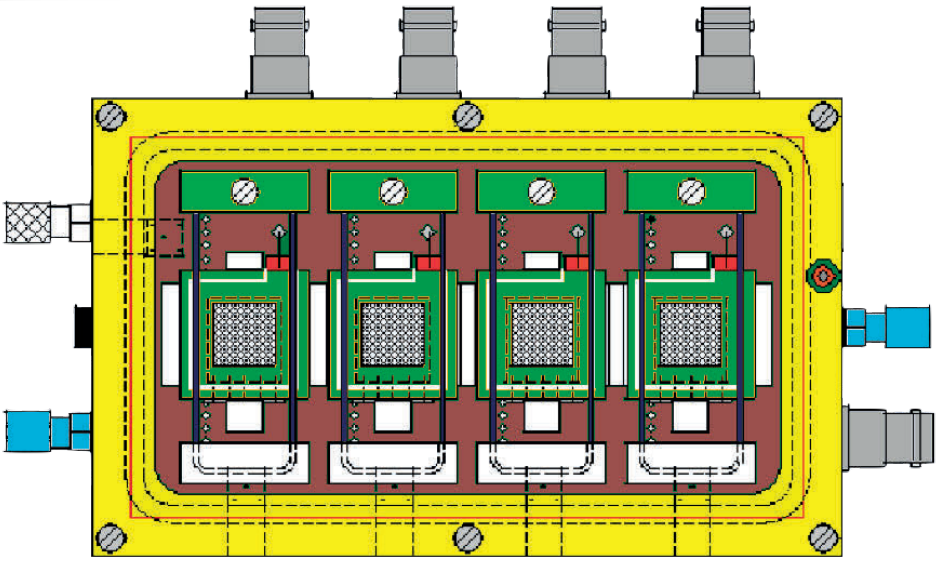

Figure 6.1: *An illustration of the spark test-chamber. The PCB (brown) hosts up to four chips. A frame (green) which contains a micromegas grid is held on top of each chip by two silicon rubber wires (blue). The high voltage for each micromegas is provided through SHV connectors (grey) to a dedicated pin on the PCB. A thin gold-plated tungsten wire makes a spring contact to the grid (red). A frame (yellow) which contains the gas inlet and outlet (cyan) and the cathode, encloses everything in a gas-tight chamber.*

The PCB is mounted on a metal frame hosting high voltage (SHV) connectors for each grid and for the cathode. The design of the PCB allows inserting of a honeycomb strip pre-amplifier [116] on each channel to monitor the induced grid current. The cross sections of the chamber is shown in figure 6.2.

Note that if the pre-amplifier is inserted, the micromegas grid is capacitively coupled to the honeycomb strip amplifier. Consequently, the grid capacitance is increased from its own capacity of 30 pF to 1 nF. As a result, the electrical energy that is stored in the grid is about 30 times larger greatly increasing the risk on damage. Figure 6.3 shows the equivalent circuit.

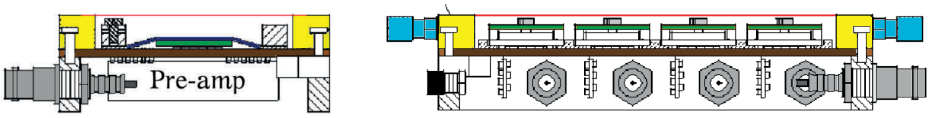

Figure 6.2: *Cross sections of the detector, along (on the left) and perpendicular (on the right) to the silicon rubber wires. The honeycomb strip pre-amplifier is inserted at the bottom side of the PCB, below the chip. This allows the exchange of the pre-amplifier while the chamber remains under gas. The colors follow the same convention as in figure* 6.1.

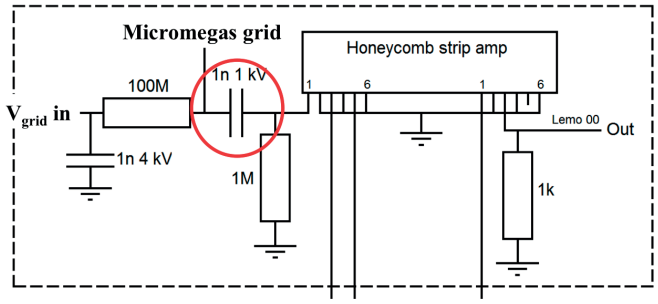

Figure 6.3: *A schematic of the equivalent circuit of the detector when the honeycomb strip pre-amplifier is connected. Due to the capacitor (in the red circle) the grid capacitance (*30 pF*) is increased to the order of* 1 nF*.*

6.3 Spark tests on dummy chips

The spark setup was initially designed for use in the lab for measurements with dummy chips. Later on we used it for real Timepix3 (or Timepix) chips as well. A dummy chip is an imitation model of a real Timepix3 chip consisting of a plain silicon substrate. Dummy chips with the desired geometry can be easily produced. In addition, the absence of sensitive electronics makes them suitable for extensive spark tests.

The fabrication of the dummy chips was performed in the Else Kooi Laboratory (EKL) at Delft [117] and is based on standard 4-inch silicon wafers. A thin metal layer $O(1\ \mu m)$, acting as anode electrode is sputtered on top of the silicon wafer. The next step is the deposition of the protection layer directly on top of the metal substrate. Subsequently the wafer is diced to single chips with the same dimensions of a Timepix3 chip. An illustration of a dummy chip is shown in figure 6.4.

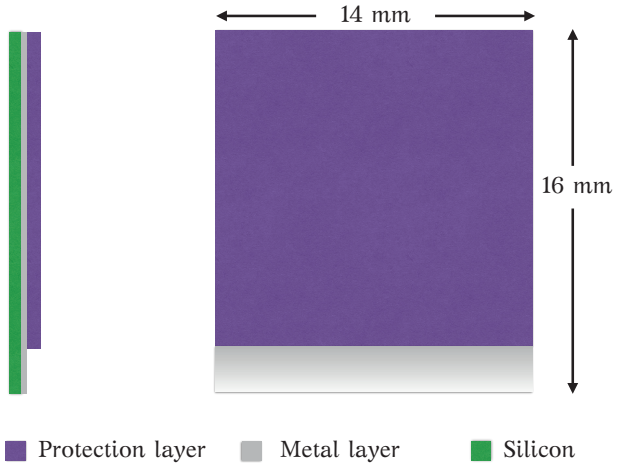

Figure 6.4: *The geometry of a dummy Timepix3 chip. The silicon substrate is covered by a thin metal layer followed by the deposition of the protection layer. One side of the metal layer is reserved for electrical connections and hence is not covered by the protection layer.*

6.3.1 Micromegas grid

The micromegas grids for the spark setup were fabricated at the Micro-Pattern Technologies workshop at CERN, with the same procedure described in subsection 5.1.2. A 2.5 × 2.5 cm copper sheet (5 µm thick) on a kapton backing (50 µm thick) is used. Grid-holes with a pitch of 80 µm are etched in the central area of the copper sheet covering a total area of about 1.4 cm^2. The copper sheet is mounted on a glass fibre epoxy frame with the same outer dimensions. An extension of the copper sheet is reserved for the connection of the grid high voltage. Pillars spaced every 650 µm keep the grid flat when it is pressed on top a chip, see figure 6.5.

6.3.2 Working principle

We aimed to generate large numbers of sparks in the active area of the spark test-chamber. To get into this condition, we directed the incoming gas through a thorium maze. Thorium (^{232}Th) weakly decays under emission of alphas to a number of isotopes thereunder radon (^{222}Rn), a gas decaying in 55 s under the emission of an alpha particle.

By this method we create a multitude of heavily ionizing alpha particles in the active area of the detector. Frequently, the avalanches that are generated by the alpha particles exceed Raether's limit, leading to a discharge. By monitoring the grid

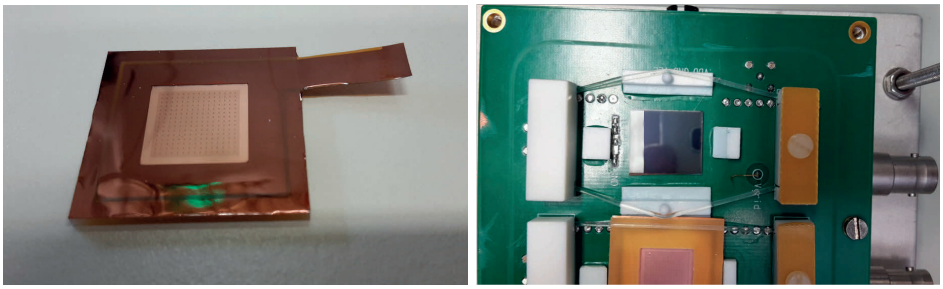

Figure 6.5: *On the left, an overview of the bottom side of the frame which holds the micromegas grid. The hole patter is covering the cental area. The extension for the high voltage is also visible. On the right, a dummy chip placed in the setup, ready for the micromegas. The silicon rubber wires that will push the micromegas down have been placed aside. At the neighboring channel, the top side of a micromegas frame in place is also visible.*

current we check for the presence of a spark.

6.3.3 Protection layer samples

In the past SiRN occasionally has given discharge problems. Therefore, we decided to investigate alternative materials and study their performance. A promising material for use as protection layer is Silicon Carbide (SiC), which suffers less from defects during deposition. In addition, the process-parameters can be tuned in order to get the the desired resistivity.

We started with layers of SiC, 4 µm or 8 µm thick, that were deposited on top of a thin aluminium layer (1 µm). A metal layer is needed to get a well conducting anode. The choice of the metal substrate is based on the fact that the top level of Timepix3 pixel pads is made of aluminium. As an alternative, we also investigated the behaviour of SiC deposited on another metal substrate, 0.5 µm titanium. Figure 6.6 shows the surface structure of the SiC layers used.

6.3.4 Experimental setup

For the tests with the dummy chips the chamber was flushed with CO_2/DME (50/50) with a typical flow of 10 mL/min. The O_2 levels were measured by an oxygen meter. To measure the gas gain an ^{55}Fe radioactive source can be placed on top of one of the channels. Subsequently,the grid-signal is readout via the pre-amplifier and a shaping ORTEC spectroscopy amplifier [118].

The high voltage for the micromegas grids was provided by miniHV power supplies [102]. A dual MWPC Modular power supply (model 5900) [119] provides the negative voltage for the cathode. The high voltage system is controlled by LabView,

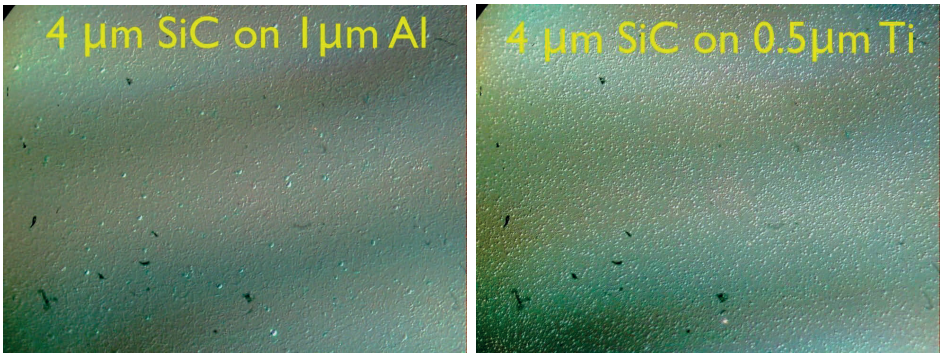

Figure 6.6: *The surface structure of a* 4 µm *thick SiC layer on top of* 1 µm *of aluminium (on the left) and* 0.5 µm *of titanium (on the right). The magnification and the illumination are the same. The surface structure is different due to the difference in the roughness of both layers.*

monitoring the voltage and the current values for each channel to an ASCII file with a sampling rate of 4 Hz. Figure 6.7 shows an overview of the setup during operation.

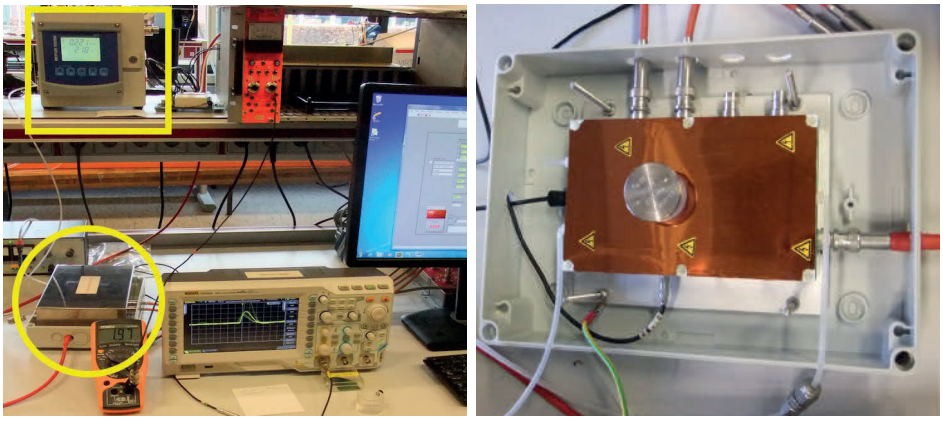

Figure 6.7: *On the left: The experimental setup during the operation with the source. The chamber (in the bright circle) was covered with a stainless steel box acting as a Faraday cage. The avalanche signals induced on the grid were displayed on an oscilloscope. On the right: A closer view of the spark test-chamber without the stainless steel box. The* ^{55}Fe *source on top of the chamber is visible.*

6.3.5 Performance of the setup

During operation the grid-current of all the channels was usually a fraction of a nA, depending on the baseline current of the power supply. In case of a spark discharge peaks of several µA during less than a second were visible. Note that the discharge current peak is greatly smeared out in time by the limited bandwidth of the high voltage system. The discharge is arrested by the drop of the electrical amplification field after which the electric field is restored in about 300 ms. With a sampling rate of 4 Hz we were able to record all discharges. Figure 6.8 shows a rare example with four consecutive sparks.

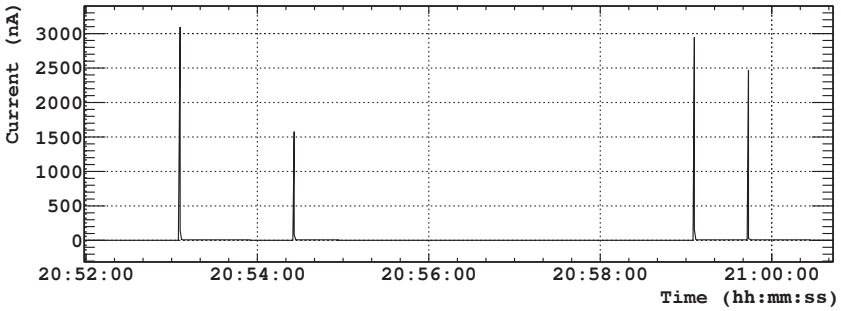

Figure 6.8: *The grid current for a run with a dummy chip covered with a* SiC *protection layer and an aluminium metal substrate. The chamber was operated with a* CO_2/DME (50/50) *gas mixture, the corresponding grid voltage was* -600 V. *Each peak corresponds to a spark.*

The ASCII file which contains the data was processed offline. If the current exceeds a certain threshold value, typically 0.5-1 nA above the baseline current of the miniHV, we consider the event as a spark. We counted the total number of sparks and the frequency and calculated properties like the time difference between two consecutive sparks, the total charge of each spark and the peak current. The information was stored in a separate ROOT-file. Figure 6.9 shows basic histograms of some spark properties.

We divide the sparks depending on their properties (peak current, total charge) in two basic categories. The first category contains discharges that are successfully quenched with the mechanism that was described in section 6.1. The second category contains occasional discharges, sufficiently high to damage the chip. We consider discharges that belong to this category as "killer sparks". For the present analysis we have put the threshold for these discharges at 400 nA, subfigure 6.9c. Subfigure 6.9d shows the histogram of the charge of a spark. On values below 300 nC) we observe a peak. We treat the entries contributing to this peak as successfully quenched discharges. Higher charges may be lethal to the chip.

After the end of the measurement, each dummy chip each was visually inspected

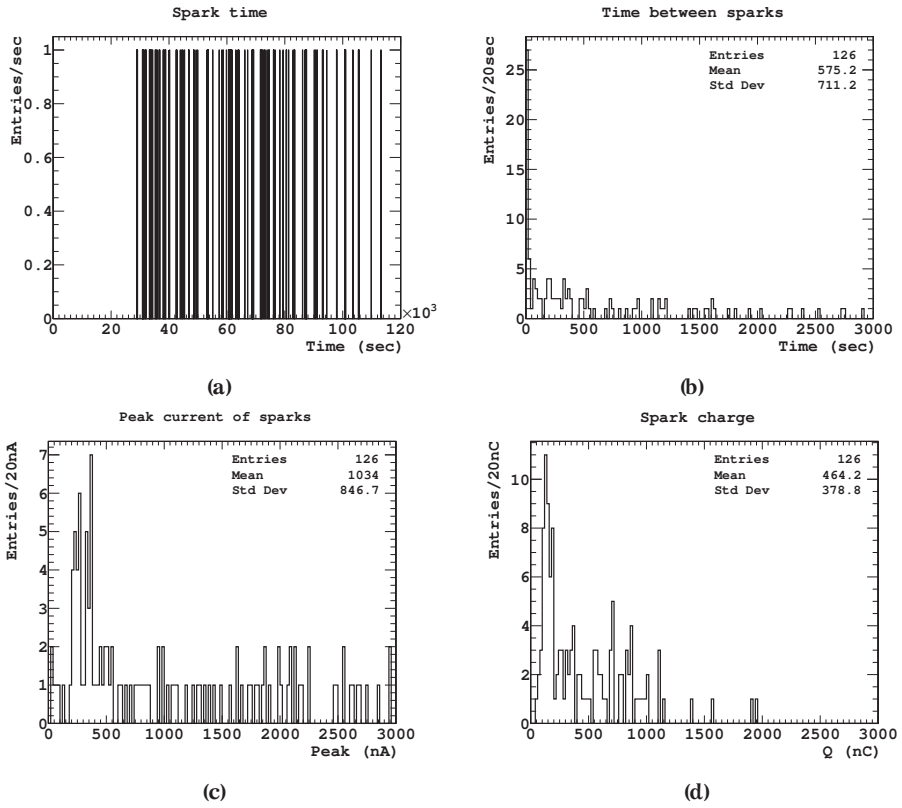

Figure 6.9: *Spark properties for a run recorded with a dummy chip with a* SiC *protection layer and an aluminium metal substrate. The run duration is about 33* h*. The chamber was operated with a* CO_2/DME (50/50) *gas mixture, the grid voltage was* -600 V*. The histograms show:* **(a)** *the occurrence of the sparking,* **(b)** *the time between two consecutive sparks,* **(c)** *the peak current of the spark as measured by the miniHV and* **(d)** *the total charge of the spark.*

under the microscope to track potential damage on the protection layer. Figure 6.10 shows a typical example of spark-damage on the SiC protection layer of a dummy chip. The damage is similar to what we have seen on real chips in chapter 5. The peak current of the discharge that damaged the chip in the testbeam of chapter 5 was about 7 µA (see figure 5.14) while with the spark test-chamber we observe discharges with a maximum peak current of 3 µA, see figure 6.8. The spark is bursting the layer, exposing the aluminium metal substrate. This is the effect of "killer" sparks on the protection layer. Note that the size of the damage is comparable to the pixel pitch of 55 µm. The full size of a spark is contained within a pixel. Such damage is expected

to be caused by the big coupling capacitor between the grid and the pre-amplifier.

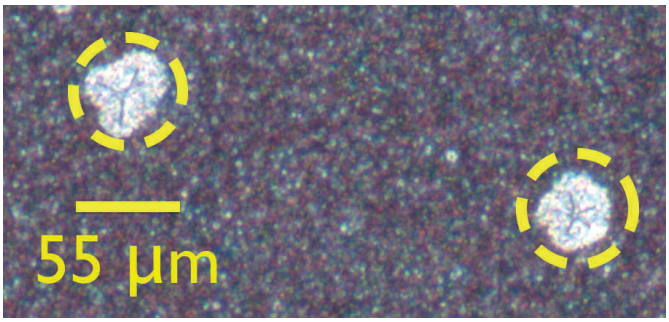

Figure 6.10: *Photograph of the damage on the SiC protection layer of a dummy chip with an aluminium metal substrate. The damage is similar to the one observed to the chip damaged in the tesbeam, see figure* 5.14.

The gas gain in the CO_2/DME (50/50) mixture has been measured with an ^{55}Fe source. The source was placed on top of one of the four channels of the setup. Figure 6.11 shows the characteristic gas gain curve for the CO_2/DME mixture, calculated as described in appendix C.

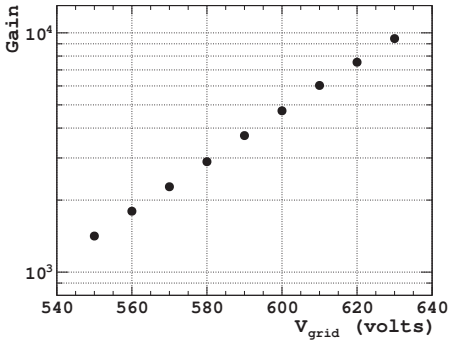

Figure 6.11: *Gas gain measurement performed for the* CO_2/DME (50/50) *gas mixture.*

6.4 Results with dummy chips

6.4.1 Spark tests

We examined of layers of SiC on top of an aluminium or a titanium anode on their sensitivity for sparking. In the offline analysis we traced potential "killer" sparks getting information about the quality of the protection layer. Table 6.1 summarises the results[1] obtained.

Table 6.1: *Summary of the results obtained with* SiC *protection layers*

Layer thick. (µm)	Metal substr.	Metal thick. (µm)	Layers tested	Comments
4.0	Al	1.0	3	Heavily sparking at 600 V. More than 10 killer sparks over a week at 550 V.
8.0	Al	1.0	2	Less than 5 killer sparks over a week at 550 V.
4.0	Ti	0.5	1	Not a single killer spark over the whole voltage range for 3 weeks.

The table shows that aluminium anodes covered with 4 µm do not protect the chip from sparks at moderate gain (~1000), while for high gain values, we get constant sparking. The protection improves with 8 µm thick layers, but still is not sufficient to quench all sparks. On the other hand, SiC layers deposited on titanium substrates, successfully quench all sparks for weeks even at a gain of about 10000. For future GridPix detectors, adding titanium on the pixel pad, combined with SiC layers might tackle the spark problem successfully.

A possible explanation is that the titanium surface is not as rough as that of the aluminium, see figure 6.12. The increased roughness of the aluminium thin films leads to defects resulting in breakdown. We tested a possible dependence on the sputtering temperature, [121]. By comparing samples sputtered at 350°C and 25°C, no significant difference was observed between the protection of both methods.

6.4.2 Ageing test

To investigate possible ageing effects in the detector we have used a ^{90}Sr source of 75 MBq. The source was centred above a channel providing even illumination up

[1]The results presented in this section were presented at the International Workshop of Radiation Imaging Detectors (iWoRiD2016). The proceeding was published in the Journal of Instrumentation as an article under the title "Towards spark-proof gaseous pixel detectors" [120].

Figure 6.12: *A photograph taken under microscope showing the surface structure of a thin aluminium film* (1 µm) *on the right and a thin titanium film* (0.5 µm) *on the right. Both films were sputtered at a temperature of* 350°C. *The titanium surface is much smoother compared to the aluminium's one.*

to a good approximation. The detector was flushed with a CO_2/DME (50/50) gas mixture and the voltage of the corresponding grid was set at -600 V. The total dose collected was about 2 µC/cm^2, see figure 6.13.

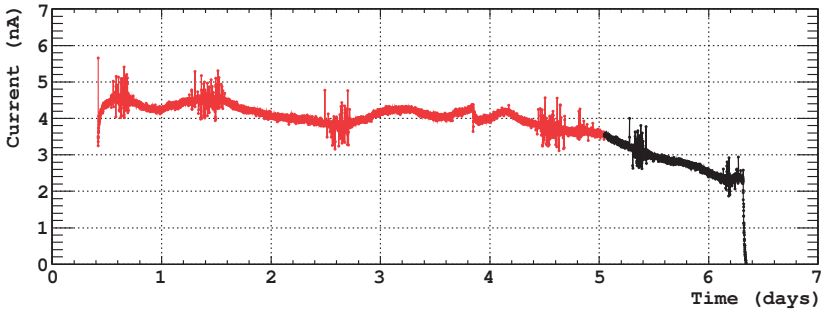

Figure 6.13: *Monitoring of the grid current during the irradiation with the* ^{90}Sr source. *Except some variations due to the enviromental conditions, there is no significant decay observed to the current due to ageing effects up to the* 5th *day (red points). Beyond this point the bottle was running out of gas and therefore we obsereve a decay to the current (black points).*

After a visual inspection of the protection layer under a microscope we observed a pattern of blacks spots, figure 6.14 matching exactly the pattern of the micromegas grid-holes. The effect is more intense on the edges of the grid. The black spots are presumably due to polymerisation debris produced during the avalanche. The dot like

structure of the deposition of the debris corresponds to the locus of the avalanches.

Due to their nature those fragments show excellent adhesion to the surfaces and consequently are attached to the grid and the protection layer. The debris at the grid is forming of a layer which becomes positively charged. This produces a large dipole electric field exceeding the threshold for field emission and causing electron emission from the grid that may led to additional avalanches. This effect is known as the Malter effect [122] and could lead to an increase of the discharge rate. Also, the debris that is attached to the protection layer will deteriorate the detector performance.

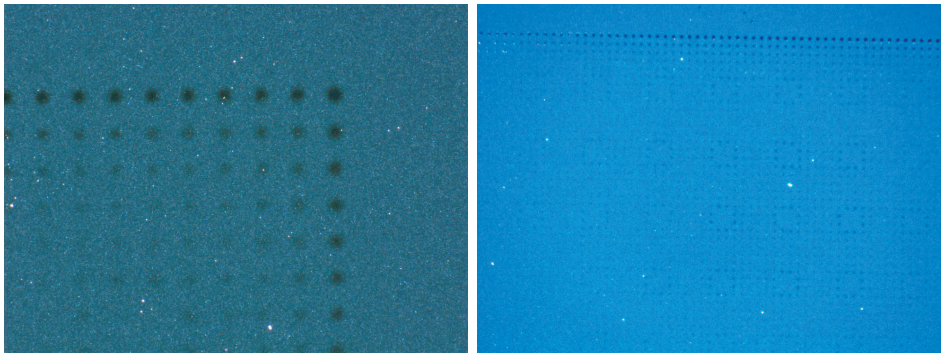

Figure 6.14: *Effects of ageing after having collected* 2 $\mu C/cm^2$. *The left picture shows the pattern on a corner of the grid. The right picure (taken under different illumination) shows an edge of the grid and circular patterns on the place of the pillars.*

6.4.3 Summary

In this study, the possibility to use SiC for the protection layers of GridPix has been investigated. The tests performed on dummy chips covered with SiC layers show promising results for the case where titanium is used for the metal layer of the anode. In the future it would be interesting to make use of titanium for enlargement of the original aluminium pixel pads of the Timepix3 chip by post-processing. Apart from the improvement in the charge collection efficiency that can be achieved according to this [123], the pad enlargement in combination with a SiC protection layer might offer a solution to the problem of discharges in GridPix detectors

Ageing effects should thoroughly be tested in the future. For a GridPix detector equipped with an aluminium grid and a careful selection of the surrounding materials the ageing effects are expected to be less than what we observed with the current setup (coppered kapton micromegas grid, silicon rubber straps, pollutants in the gas, etc.). In any case the reliable long term operation with successful quenching of all the discharges still remains to be demonstrated.

6.5 Tests in a hadron beam

The production of Timepix3 InGrids took place in July 2016 at the Fraunhofer Institute for Reliability and Microintegration (IZM) in Berlin. The fabrication was based on a standard 8-inch silicon wafer with the procedure described in subsection 3.4.4. The material used for the protection layer of the InGrids was silicon-rich silicon nitride (SiRN).

The deposition of the protection layer was done for the first time using a machine specialised in silicon nitride (SiN) processing, that is able to deliver thin films of SiRN with a high homogeneity. Therefore, the performance of the layer against discharges is of paramount importance for the reliability of the GridPix detectors in the future.

For about a week in November 2016 we have exposed two spark test-chambers, containing in total 8 InGrids, in a high rate hadron beam (for a description see chapter 5). The testbeam took place at the H8 beam line of the Super Proton Synchrotron (SPS) at CERN. Besides the high intensity of the hadron beam, high ionisation events also occur due to nuclear interactions with the chamber's material which could lead to excessive sparking. In the past several chip failures occurred in hadronic testbeams, which motivates such a test. This section describes the experiment performed along with the results obtained.

6.5.1 Experimental testbeam setup

For the testbeam we built a second spark test-chamber enabling the simultaneous testing of 8 chips in total. The InGrids were mounted on the PCB by a double sticky tape. The wire springs have been replaced by 80 µm thick copper wires glued onto grid. Reasonable care was taken for the grounding of the chips, see figure 6.15.

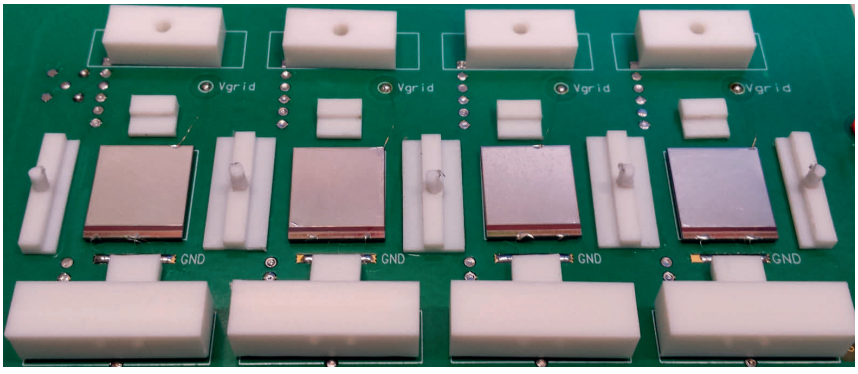

Figure 6.15: *A close view of four Timepix3 InGrids mounted on the PCB of one of the chambers used during the testbeam. The ground contacts were made with conductive glue to a ground bar on the PCB.*

Since the design of the spark test-chamber does not allow the readout of the chips, we only used non-functional ones. But we selected high quality InGrids to avoid discharges due to imperfections of the grid. During the testbeam we have installed the following chips on the two chambers,

- 4 Timepix3 InGrids covered with a 4 µm thick SiRN layer.
- 2 dummy chips covered with a 4 µm thick SiRN layer.
- 1 Timepix InGrid, covered with a 4 µm thick SiRN layer.
- 1 Timepix InGrid, covered with a 8 µm thick SiRN layer.

The Timepix3 InGrids were installed in one chamber and the rest of the samples in the other one. Although we were mainly interested in the performance of the Timepix3 chips, we liked to use chips with other pad geometry as a reference.

During the testbeam the whole setup was mounted on a leak tray to comply with the CERN safety precautions for gaseous detectors, see figure 6.16. The leak tray was attached to a remotely controlled movable XCSA table to enable the alignment to the beam.

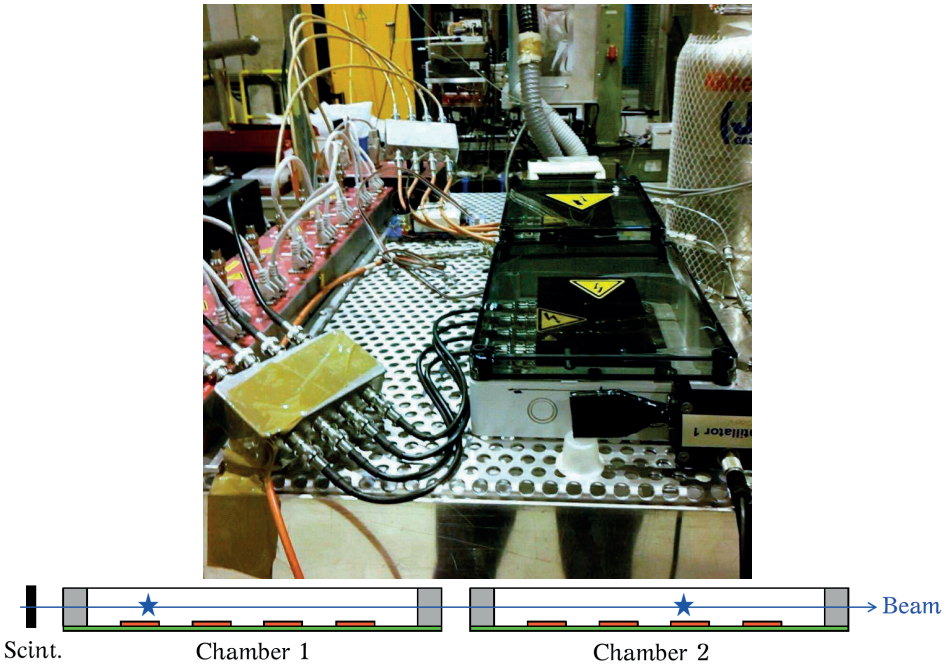

Figure 6.16: *The experimental setup during the testbeam. A small size scintillator in front of the chambers has been used for alignment puproses and to get an estimate of the beam rate.*

The setup was remotely controlled by LabView. We registered the high voltage and the current of each grid, the cathode high voltage, the gas flow, the oxygen level and the absolute pressure. All monitoring information was also written out to an ASCII text file.

For the tests we have used the same high voltage systems that were described in chapter 5. For the gas flow regulation of the input flow and registration of the exhaust flow we used a Bronkhorst InFlow mass flow controller/meter [124]. The chambers were put in series. Two different pre-mixed gas bottles were used, containing a CO_2/DME (50/50) and a Ar/CF_4/iC_4H_{10} (95/3/2) gas mixture. The gain of both mixture was measured before the testbeam using an ^{55}Fe source. Figure 6.17 shows the gain curves for both gas mixtures.

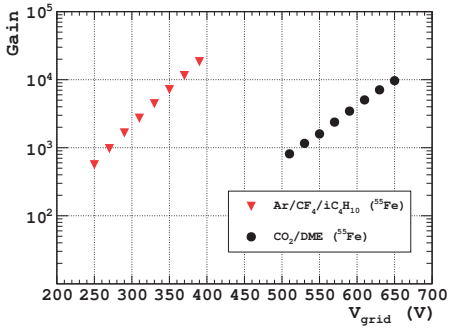

Figure 6.17: *Comparison of the gas gain measured for a* CO_2/DME (50/50) *and a* Ar/CF_4/iC_4H_{10} (95/3/2) *gas mixture. For the measurement we read out the signals induced at a Timepix3 InGrid by an* ^{55}Fe *source. In order to reach the same amount of gas gain, the* Ar/CF_4/iC_4H_{10} *requires the half of the voltage needed for the* CO_2/DME *gas mixture.*

6.5.2 Alignment to the beam

The chambers were placed in such a way that the particle tracks ran parallel to the InGrids, passing the full active surface of all chips. We pre-aligned the chambers to the beam by an alignment laser. The alignment was completed by adjusting the chambers to a maximum of the current during the spill. As a crosscheck we observed the particle rate of the upstream scintillator.

6.5.3 Monitoring

In the first test period the chambers were filled with the Ar/CF_4/iC_4H_{10} (95/3/2) gas mixture. The electric field at the drift area was constant and was set to 1 kV/cm. We performed a high-voltage scan of the Timepix3 InGrids to measure the gain and

investigate charging-up effects of the layer. The Timepix3 InGrids were operated at extremely high voltages for this gas mixture like 450V over a long period to generate possible discharges.

The beam had a spill duration of 5 s and a period of 30 s. The particle rate during the was about 200 kHz/cm^2. At the start of the spill the grid current was proportional to the particle rate, the active area of the InGrid and the gas gain. After that we observed a decay caused by the voltage drop across the protection layer and the spill structure.

The current was sampled with a rate of 4 Hz. Its curve shows the spill structure of the beam. Figures 6.18, 6.19 show the grid current over short periods of a few spills for various voltages in the Ar/CF_4/iC_4H_{10} gas mixture. At -310 V and -350 V all the channels were "quiet" for a typical run duration of 1-2 h, with a small probability on discharge . At -390 V and -410 V we recorded longer runs (typical duration of a few hours) where the discharge rate increases and more prominent discharges occur. The discharge rates are given in a following section.

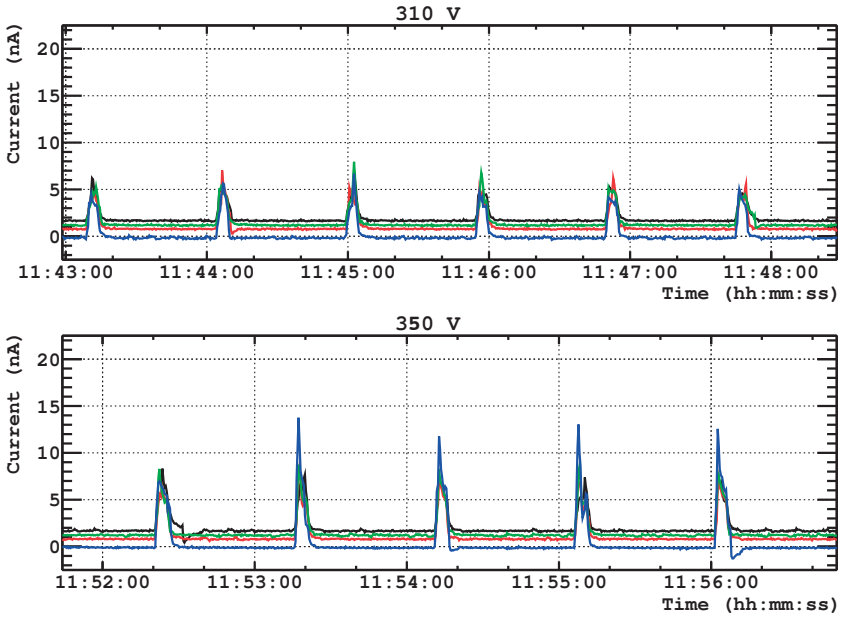

Figure 6.18: *The grid current of the four Timepix3 InGrids operated at -310* V *and -350* V *in the* Ar/CF_4/iC_4H_{10} *gas mixture.*

At -450 V, discharges up to 40 nA occur almost in every spill. More prominent discharges up to a few hundred nA occur approximately every 10 min, figure 6.20. If the discharge occurs close to a defect of the protection layer, might reach the chip.

Connecting the pre-amplifier to one of the Timepix3 InGrids the grid capacitance

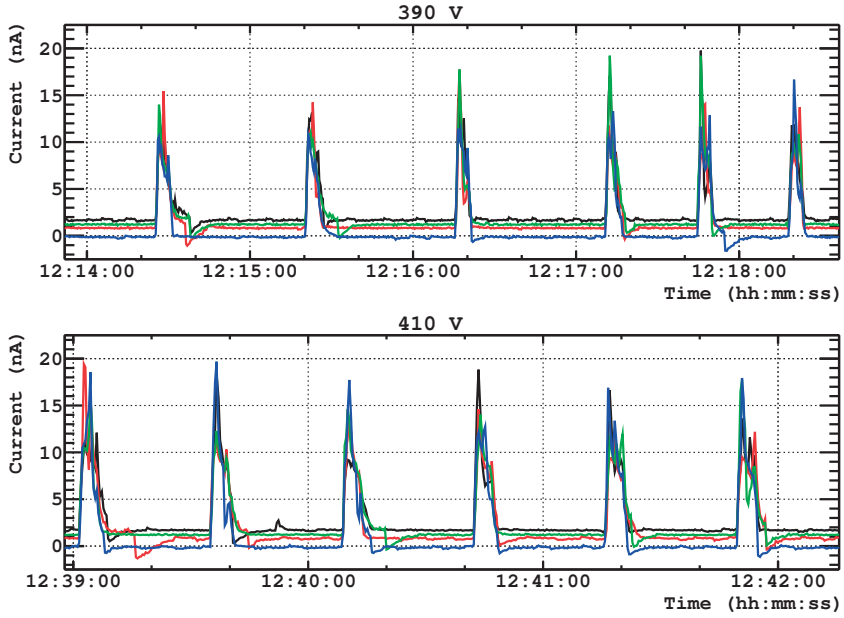

Figure 6.19: *The grid current of the four Timepix3 InGrids operated at -390* V *and -410* V *in the* $Ar/CF_4/iC_4H_{10}$ *gas mixture.*

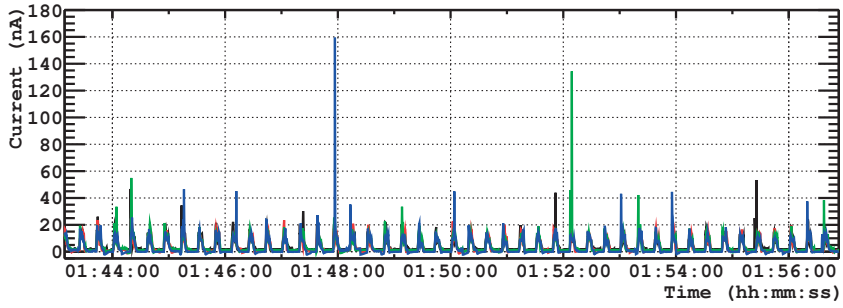

Figure 6.20: *The grid current at the Timepix3 InGrids operated at* 450 V *in the* $Ar/CF_4/iC_4H_{10}$ *gas mixture when the pre-amplifier is not inserted.*

is increased from 30 pF to 1 nF. leading to discharges up to thousands of nA. Such discharges can deliver severe damage to the protection layer and release large amounts of electrical energy to the chip.

During the last days of the testbeam period we switched to the CO_2/DME (50/50) gas mixture. For the spark test of this gas we used only one Timepix3 InGrid

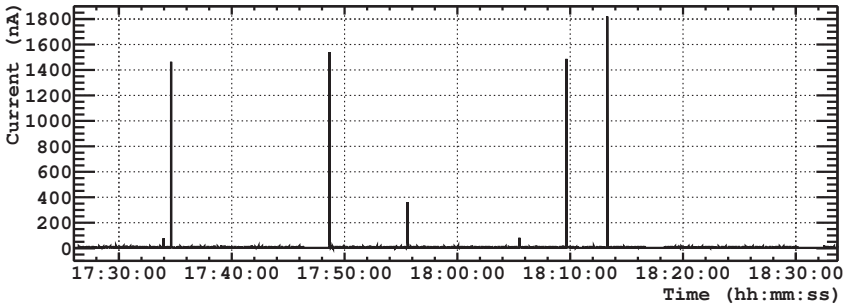

Figure 6.21: *The grid current at one Timepix3 InGrid operated at* 400 V *in the* $Ar/CF_4/iC_4H_{10}$ *gas mixture when the pre-amplifier is inserted.*

preserving the others for offline investigation. For the data taking we kept working method as in the first test period. Beginning from low values we gradually increased the high voltage, recording data in the voltage range of 550-700V. .

6.6 Results with Timepix3 chips

6.6.1 Gain drop due to charging-up effects

The gas gain during a spill was different from the one measured in the lab with the ^{55}Fe source at the same grid voltage since the integrated signal current of the beam charges up the protection layer. As a result there is a potential drop across the layer which leads to a drop in the electric field in the amplification area.

For the measurement of the actual gas gain during the testbeam we use the averaged value of the current I_{grid} that is induced to an InGrid during a spill. The expected grid current is given by eq. 6.1,

$$I_{grid} = R_{\text{beam}} \cdot A \cdot l_g \cdot N_{e^-} \cdot G \cdot q_{e^-}, \tag{6.1}$$

where R_{beam} is the beam rate, A is the active area of the InGrid (i.e the area of the Timepix3 chip), l_g is the length of the grid in beam direction, G is the gas gain and $q_e = 1.6 \cdot 10^{-19}$ C is the electric charge of the electron.

By re-writing eq. 6.1 we obtain the gas gain as a function of the grid current,

$$G = \frac{I_{grid}}{R \cdot A \cdot l_d \cdot N_{e^-} \cdot q_{e^-}}. \tag{6.2}$$

We applied expression 6.2 to calculate the gain during the testbeam experiment using R = 200 kHz/cm^2, A = 2 cm^2 and l_g = 1.4 cm. Using [125,126] we get for N_{e^-} = 96 e$^-$/cm for the $Ar/CF_4/iC_4H_{10}$ mixture. The calculation is obtained for

normal temperature and pressure conditions[2] (NTP), approximately the same to the environmental conditions in the testbeam area.

Figure 6.22 shows the measurement of the gain obtained by using eq. 6.2 in comparison with the measurement obtained with the ^{55}Fe source.

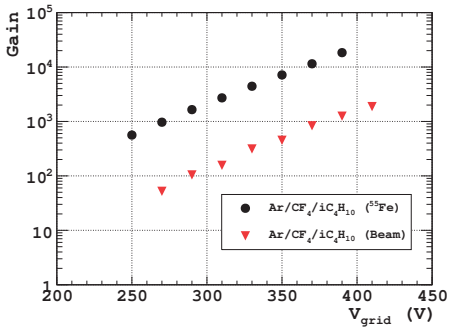

Figure 6.22: *Comparison of the gas gain of the* $Ar/CF_4/iC_4H_{10}$ (95/3/2) *gas mixture measured in the lab with an* ^{55}Fe *source and by using the average current induced at a Timepix3 InGrid during a spill. The latter is reduced due to the rapid charging-up of the protection layer.*

In the high intensity beam we observe a drop in the gain of about one order of magnitude compared to the low rate ^{55}Fe source.

In 1956, W. Diethorn in [127] assuming a linear relation of the first Townsend coefficient α with the amplification electric field E derived a formula for the gas gain in wire chambers which depends on the high voltage applied on the wire. Under the assumption the can write eq. 2.23 as follows,

$$G = e^{\alpha l_d} = e^{\kappa E l_d} = e^{\kappa V_{\text{grid}}}, \tag{6.3}$$

where κ is a constant depending on the applied gas mixture that can be obtained by fitting the gain curve with an exponential function. Due to the charging-up effects the reduced gas gain G' is given by,

$$G' = e^{\kappa\left(V_{\text{grid}} - \Delta V\right)}. \tag{6.4}$$

By combining eq. 6.3 and 6.4 we get an estimate of the voltage drop ΔV across the protection layer,

$$\ln \frac{G}{G'} = \frac{e^{\kappa V_{\text{grid}}}}{e^{\kappa\left(V_{\text{grid}} - \Delta V\right)}} = e^{\kappa \Delta V}. \tag{6.5}$$

[2]Normal Temperature and pressure (NTP) is defined as air at at 20 °C and 1 atm.

In figure 6.22 we see that with the ^{55}Fe source at 370 V we reach a gain of 10^4, an order of magnitude higher than in the beam. By using eq. 6.5 we calculate a drop of 100 V across the protection layer, much larger than the tolerated voltage drop for high rate application of less than 5 V to maintain an acceptable efficiency.

In Appendix B we describe a method to calculate the volume resistivity ρ of the protection layer, based on the voltage drop across the layer. By using this method, we obtain an estimate of the resistivity of the protection layer of the Timepix3 InGrids,

$$\rho = \frac{\Delta V \cdot A}{I_{\text{grid}} \cdot d_l} \approx 0.5 \cdot 10^{13}\ (\Omega \cdot \text{m})\,. \tag{6.6}$$

This method gives an overestimate of the resistivity of about a factor 10 due to the small pad size of the Timepix3 chip. In eq. 6.6, $A = 2$ cm^2 is the area of the Timepix3 chip and $d_l = 4$ µm is the thickness of the protection layer. We observed during the testbeam that above 400 V the grid current practically remains constant as the grid voltage increases. Therefore this specific layer sets a limitation to the gas gain value that can achieved with a Timepix3 InGrid. In addition, the resistivity of the layer does not allow the use of a GridPix detector in high rate applications. For future applications a recipe for SiRN with a lower resistivity should be realised.

Figure 6.23 shows the comparison of the gain measurement performed with the ^{55}Fe source in comparison with the measurement performed with the beam. For the CO_2/DME (50/50) gas mixture, the number of clusters over 1.3 mm was measured in chapter 4. Taking into account that we get 1.5 e$^-$ per cluster, for the gain calculation in eq. 6.2 we use $N_{e^-} = 75$ e$^-$/cm of a CO_2/DME (50/50) gas mixture at NTP.

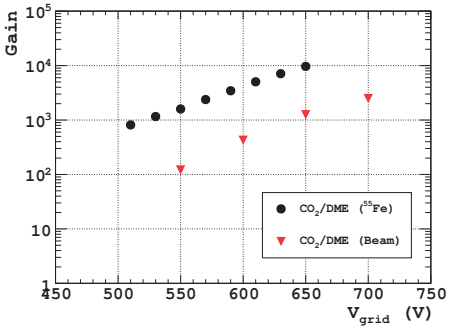

Figure 6.23: *Comparison of the gas gain of the* CO_2/DME (50/50) *gas mixture measured in the lab with an* ^{55}Fe *source with the gain calculated from the average current induced at a Timepix3 InGrid during a spill.*

The figure shows that for the CO_2/DME (50/50) gas mixture the high rate behaviour is more or less comparable to that for the Ar/CF_4/iC_4H_{10} (95/3/2) mixture. Here the drop of the gas gain is 9-10 while it is about 13 for the Ar/CF_4/iC_4H_{10}

(95/3/2) mixture in figure 6.22. The difference can be explained by the difference in the slope of the gain curves for both gases figure 6.17.

After the testbeam we have measured the surface resistivity of the protection layer using a Mercury probe. The working principle is based on the probing of a surface with liquid mercury. A vacuum pump pushes the mercury against the sample, making contact to a well-defined area on the tested surface.

We tested a bare Timepix3 and dummy chips covered with a protection layer. The interface of the mercury and the protection layer form a non-permanent contact. The device can be used to perform Capacitance-Voltage (CV) and Current-Voltage (IV) measurements. The surface resistivity ρ_s of the protection layer can be extracted from IV measurements. By multiplying with the thickness of the protection layer d_l we obtain the volume resistivity ρ given by eq. 6.7,

$$\rho\,(\Omega \cdot \mathrm{m}) = \rho_s\,(\Omega/\square) \cdot d_l\,(\mathrm{m})\,. \tag{6.7}$$

In the context of this thesis, we discuss only the volume resistivity ρ. Figure 6.24 shows the volume resistivity obtained from the measurement against the voltage applied on the protection layer of a Timepix3 and a dummy chip.

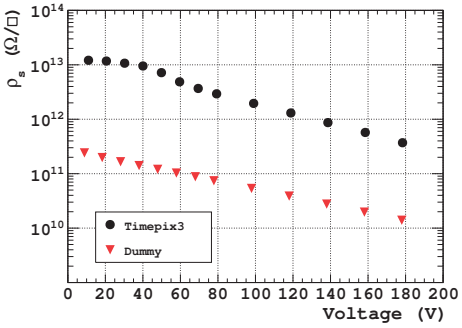

Figure 6.24: *Measurement of the surface resistivity ρ_s of the protection layer against the applied voltage for a Timepix3 and a dummy chip covered with a* SiRN layer. *The measurement performed with a mercury probe.*

The volume resistivity that can be obtained by eq. 6.7 is in agreement with the approximate value that we obtain from eq. 6.6. Nevertheless, the surface resistivity value is not constant for the whole voltage range. While on a dummy chip, the full anode is conducting, for a Timepix3 chip about 95% of the top layer is passivated with SiO_2, leaving only 5% of the pixel pads for the contact to the protection layer. This property is responsible for the difference of the measured resistivity between the dummy chip and the Timepix3.

Therefore, for future GridPix detectors based on the Timepix3 chip this effect should be taken into account. A GridPix with the current protection layer and

without enlarged pads is not suited for use in high rate applications. The apparent resistivity at Timepix3 can be lowered by increasing the pad size in the chip design or by post processing.

6.6.2 Sparking behaviour

During the testbeam described in section 6.5 we recorded a multitude of discharges with the Timepix3 InGrids in the two different gas mixtures. We noticed that the probability of a spark to occur only weakly depends on the presence of a beam spill while sparking may also occur in-between the spills, for example see figure 6.25.

The dataset is split in two parts, one containing the data recorded within the beam spills and the other containing the data recorded in-between. We choose a threshold value (dashed line) to make sure that we take into account entries which correspond to sparks. Because of the induced current within a spill we had to take a larger threshold value in this case. Sparks with a peak current of a few tens of nA are observed in both cases.

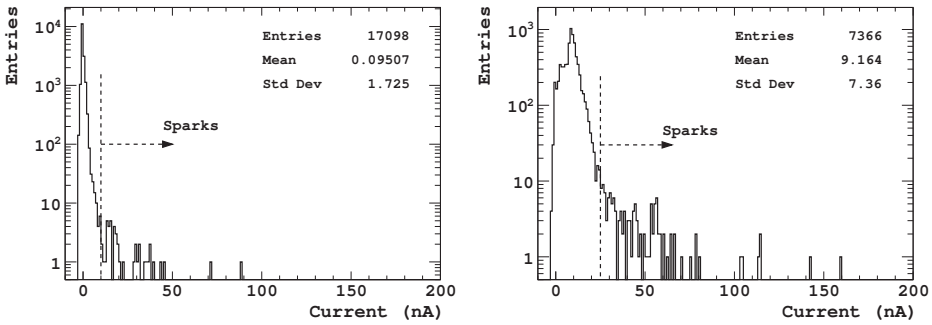

Figure 6.25: *Histograms of the grid current for of a Timepix3 InGrids operated at* 450 V *in* $Ar/CF_4/iC_4H_{10}$ *gas mixture. The left histogram shows the current in-between the spills and the right the current within the spills.*

Figure 6.25 confirms the presence of sparks in-between the beam spills with all the Timepix3 InGrids. It is very important to realise that sparks may occur at any time during operation. The protection layer should be capable of quenching them successfully.

For the analysis we processed the monitoring data and calculated the spark frequency by counting the total number of sparks at different voltages. For the calculation in the $Ar/CF_4/iC_4H_{10}$ gas mixture we considered all four Timepix3 InGrids. For the CO_2/DME gas mixture we cosidered only one Timepix3 InGrid. Figure 6.26 shows the spark frequency against the grid voltage for the two gas mixtures.

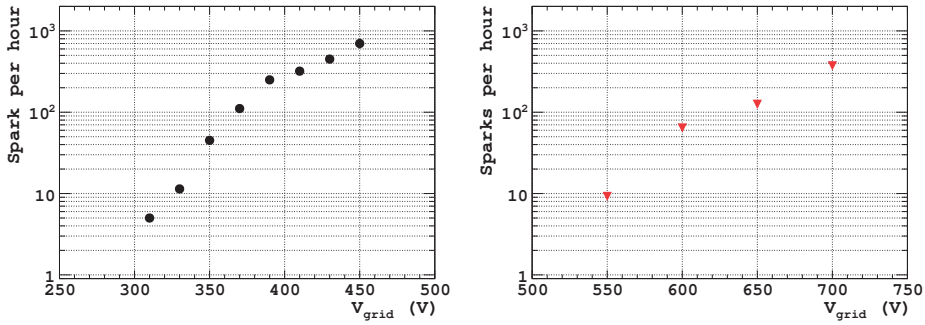

Figure 6.26: *The spark frequency versus the grid voltage of a Timepix3 InGrid measured in the* $Ar/CF_4/iC_4H_{10}$ *gas mixture on the left and in the* CO_2/DME *gas mixture on the right.*

Figure 6.27 shows a comparison of the spark frequency for the two gas mixtures that we have used during the testbeam. As expected the spark frequency increases with the gain since at higher gain the probability of a streamer formation and the transition to a discharge is larger.

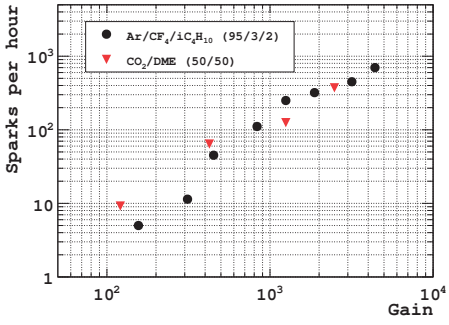

Figure 6.27: *A comparison of the spark frequency versus the gas gain of the* $Ar/CF_4/iC_4H_{10}$ *and the* CO_2/DME *gas mixture. The gas gain was calculated from the averaged grid current induced at a Timepix3 InGrid during the spill.*

The figure shows that the spark frequency curves are almost identical for both gas mixtures. However, in practise operating the CO_2/DME mixture is more risky since here it requires twice the grid voltage than that of the $Ar/CF_4/iC_4H_{10}$ mixture, increasing the chance on a lethal damage.

6.7 Visual inspection

During the testbeam we have operated the Timepix3 InGrids for long periods at large high voltages for both gas mixtures. Especially in the case where the discharge energy is large because of a connected pre-amplifier, large sparks were observed with peak currents of a few thousand nA (see figure 6.21). One of the main objectives of the testbeam experiment was to investigate if the protection layer was capable of quenching such large discharges.

After the testbeam the Timepix3 InGrids were inspected in the cleanroom under the microscope. We removed carefully the InGrids scanning for damage on the protection layer similar to what we observed in chapter 5.

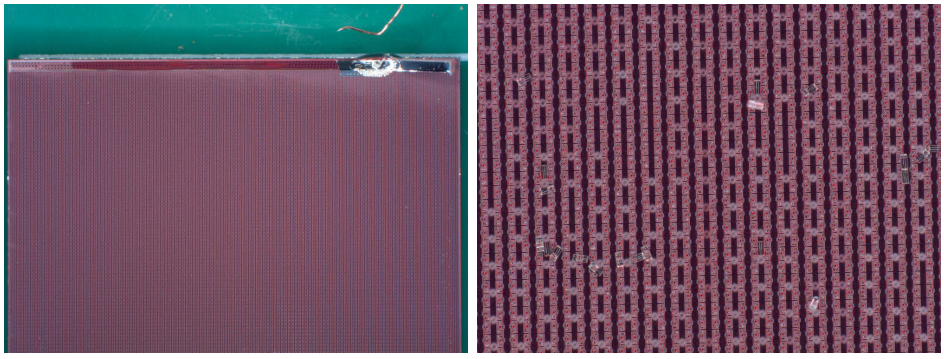

Figure 6.28: *Photographs taken during the visual inspection of the protection layer on a Timepix3 chip after the removal of its InGrid. On the left, an overview of a large fraction of the chip area. On the right, a close overview of the Timepix3 chip where the pixels are visible. The pillars are quite robust and most of them remain in place in-between the pixels after the removal of the grid. A few pillars that have been detached from their position are also visible.*

During the thorough inspection no damage was observed on the protection layer of the Timepix3 chips. A first conclusion would be that the SiRN layer is quite robust without defects. Additional to that, the 33 Ω resistor before the protection diodes that was limiting the peak current, might have contributed to the absence of damage.

Consequently all the discharges during the testbeam were successfully quenched by the protection layer. Since we used electrically defective chips, we could not verify a possible impact of the discharges on the electrical functioning. Therefore, to draw conclusions on the adequate quenching of the protection layer the test has to be repeated with electrically functioning chips.

6.8 Conclusion

To test the sparking tolerance of several protection layers, we devised a dedicated test setup. We used Timepix3 chips and dummy chips for the test.

The setup has been used in the lab to test SiC as an alternative material to SiRN for the protection of pixel chips used in GridPix detectors. We used dummy chips covered with a SiC, using aluminium and titanium as an anode surface. The results show that the deposition of a SiC layer combined with the enlargement of the pixel pads with titanium could be a promising technology for the discharge quenching in GridPix detectors. However this has to be investigated also for real chips.

We also used the setup to investigate the sparking tolerance of the protection of Timepix3 InGrids covered with a SiRN layer. The setup was installed for about a week at SPS/CERN in a high rate hadron beam. For the tests we have used an $Ar/CF_4/iC_4H_{10}$ (95/3/2) and a CO_2/DME (50/50) gas mixture to compare the sparking tolerance. We found no clear indication of a difference in sparking frequency for the same gain between both gas mixtures. Nonetheless, the use of the $Ar/CF_4/iC_4H_{10}$ is a less risky option since it requires half the grid voltage in order to achieve the same amount of gain.

The decrease of the gas gain that was observed at the high rate beam at CERN obtained shows that the current recipe for the deposition SiRN delivers a layer with too high resistivity. We also observed a frequent sparking for a wide range of grid voltages initiated by the highly ionising events induced by the beam.

The protection layers under test were inspected under the microscope after the testbeam. The SiRN layer seems to be quite robust without defects. In contrast to experience in an earlier testbeam no damage was found on the layers after the extensive sparking with a high grid capacity. Obviously the current limiting resistor in the high voltage circuitry of the grid is capable of preventing damage to the protection layer. But whether this protection is sufficient to avoid damage to the chip electronics has to be investigated.

Appendix A

Derivation of expected angles using rotation matrices

In Chapter 4, due to the absence of an external reference track, we use as a reference the beam direction which we assume that is constant. Figure A.1 illustrates the beam coordinate system (X, Y, Z).

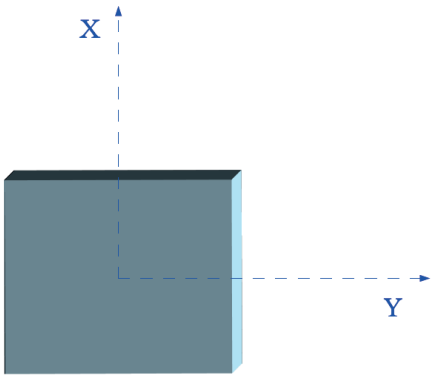

Figure A.1: *The coordinate system of the beam. The Z axis is pointing into the page.*

The detector is sitting on a goniometer which allows rotations (angle ϕ) about the Z ("beam") axis and a rotation stage which allows rotations (angle θ) about the X axis. In the ideal case, the detector coordinate system (x, y, z) matches perfectly with the beam one. Though, in case of a mis-alignment, we define ϕ_0 as goniometer offset

and θ_0 as rotation stage offset. The origin of these offsets could be the mis-alignment of the chip or reading errors of the goniometer and the rotation stage. By setting the rotation-stage and the goniometer at $(-\theta_0, -\phi_0)$, we make the tracks appear along the z axis which in this case is approximately equal to the Z axis.

By using direction cosines in the beam coordinate system, we define the beam direction vector where (d_X, d_Y, d_Z) are the coordinates of the end-point of a unit vector which starts at the origin and is parallel to the beam.

In the detector coordinate system (x, y, z) the direction of the track is given by the vector $(d_{x''}, d_{y''}, d_{z''})$. From the straight line fit, we obtain the slope for the track projections at the xz, yz and xy planes. These parameters are

$$m_{xz} = d_{x''}/d_{z''}\,, \tag{A.1}$$

$$m_{yz} = d_{y''}/d_{z''}\,, \tag{A.2}$$

$$m_{xy} = d_{x''}/d_{y''}\,. \tag{A.3}$$

At stage settings (θ_0, ϕ_0) the beam direction vector is (0, 0, 1).

For a hypothetical track we reconstruct the expected angle if we make the simplifying assumption that the the goniometer rotates about z and the rotation stage rotates about x. This means that we do extrinsic rotations of the local coordinate system of the detector while the original coordinate system of the beam is fixed.

Rotation matrices can be used to represent a sequence of extrinsic rotations. For instance, $R = R_X(\phi)R_Y(\psi)R_X(\theta)$ represents a composition of extrinsic rotations about the axes X, Y and Z if used to pre-multiply column vectors. Multiplying the rotation matrices following this sequence we can determine the actual direction of the track.

Suppose that we start at (θ_0, ϕ_0), then rotate by ϕ about the Z axis followed by a rotation by θ about the X axis. We end at $(\theta - \theta_0, \phi - \phi_0)$, figure A.2.

The total rotation matrix is $R = R_Z(\phi - \phi_0) \cdot R_X(\theta - \theta_0)$

The rotation matrices are defined as follows:

$$R_x(\alpha) = \begin{bmatrix} 1 & 0 & 0 \\ 0 & \cos\alpha & -\sin\alpha \\ 0 & \sin\alpha & \cos\alpha \end{bmatrix}, \tag{A.4}$$

$$R_y(\alpha) = \begin{bmatrix} \cos\alpha & 0 & \sin\alpha \\ 0 & 1 & 0 \\ -\sin\alpha & 0 & \cos\alpha \end{bmatrix}, \tag{A.5}$$

$$R_z(\alpha) = \begin{bmatrix} \cos\alpha & -\sin\alpha & 0 \\ \sin\alpha & \cos\alpha & 0 \\ 0 & 0 & 1 \end{bmatrix}. \tag{A.6}$$

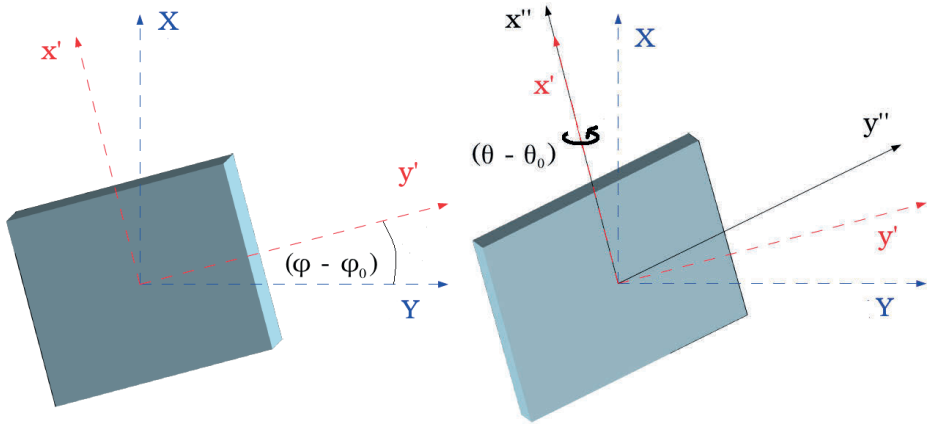

Figure A.2: *Illustration of the extrinsic rotation of the local coordinate system of the detector. The original coordinate system of the beam is fixed.*

In our case we have the following:

$$\begin{bmatrix} d_{x''} \\ d_{y''} \\ d_{z''} \end{bmatrix} = R_Z(\phi - \phi_0) R_X(\theta - \theta_0) \begin{bmatrix} d_X \\ d_Y \\ d_Z \end{bmatrix} \tag{A.7}$$

$$= \begin{bmatrix} \cos(\phi - \phi_0) & -\sin(\phi - \phi_0) & 0 \\ \sin(\phi - \phi_0) & \cos(\phi - \phi_0) & 0 \\ 0 & 0 & 1 \end{bmatrix} \begin{bmatrix} 1 & 0 & 0 \\ 0 & \cos(\theta - \theta_0) & -\sin(\theta - \theta_0) \\ 0 & \sin(\theta - \theta_0) & \cos(\theta - \theta_0) \end{bmatrix} \begin{bmatrix} d_X \\ d_Y \\ d_Z \end{bmatrix} \tag{A.8}$$

$$= \begin{bmatrix} \cos(\phi - \phi_0) & -\sin(\phi - \phi_0)\cos(\theta - \theta_0) & \sin(\phi - \phi_0)\sin(\theta - \theta_0) \\ \sin(\phi - \phi_0) & \cos(\phi - \phi_0)\cos(\theta - \theta_0) & -\cos(\phi - \phi_0)\sin(\theta - \theta_0) \\ 0 & \sin(\theta - \theta_0) & \cos(\theta - \theta_0) \end{bmatrix} \begin{bmatrix} 0 \\ 0 \\ 1 \end{bmatrix} \tag{A.9}$$

$$= \begin{bmatrix} \sin(\phi - \phi_0)\sin(\theta - \theta_0) \\ -\cos(\phi - \phi_0)\sin(\theta - \theta_0) \\ \cos(\theta - \theta_0) \end{bmatrix} \tag{A.10}$$

Using equations A.1, A.2, A.3 and equation A.10, we derive the expected slopes:

$$m_{xz} = \sin(\phi - \phi_0)\tan(\theta - \theta_0), \tag{A.11}$$

$$m_{yz} = -\cos(\phi - \phi_0)\tan(\theta - \theta_0), \tag{A.12}$$

$$m_{xy} = -\tan(\phi - \phi_0). \tag{A.13}$$

From the above equations we are able to extract the offsets ϕ_0 and θ_0.

Appendix B

Resistivity measurement of the protection layer using a source

Method

The method is based on the irradiation of the detector with a ^{90}Sr source (β^-) with an activity of 740 MBq. By using a highly active source, we simulate a situation equivalent to the high irradiation by an intense particle beam during a testbeam. This dense irradiation charges-up the the surface of the protection layer, reducing the electric field in the amplification region. The voltage across the layer creates a current which flows through the SiN layer, which at stable conditions equals to the grid current. By monitoring the behaviour of the current to grid we can estimate the voltage-drop. For simplicity, we treat the SiN layer as being "sandwiched" between two conductors[1].Subsequently the resistivity ρ is given by the following formula,

$$\rho = R\frac{A}{l} = \frac{V_{\text{drop}}}{I_{\text{grid}}} \cdot \frac{A}{l}\,, \tag{B.1}$$

where

R is resistance of the layer.

A is the irradiated area of the layer.

l is the thickness of the layer.

[1]This gives a over-estimate of the resistivity (possibly a factor 10).

Measurement

The detector was flushed with CO_2/DME gas mixture with a flow of 10 ml/min and the grid-voltage was set to 600 V. The corresponding gain was about 5000. We used a 5 mm thick glass plate to "block" the source. By suddenly removing the glass plate, we exposed the active volume of the detector to the ^{90}Sr-source. As a result we observed an increased current on the grid, which immediately dropped down to almost half of the initial value, see figure B.1. This means that also the gain is dropping roughly the same amount. From the measurements in figure 6.17 we learn that the gain halves with a voltage-drop of 30 V. Note that the actual grid voltage is a few volts lower due to the voltage drop across the 100 MΩ resistor to the grid. The following graph shows the drop on the current which follows the voltage-drop.

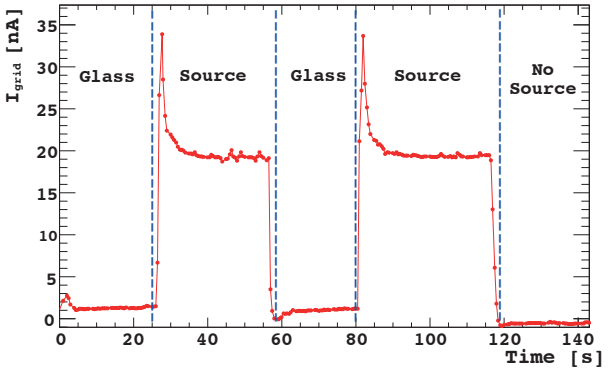

Figure B.1: *The grid current during the rradiation with a* ^{9}0Sr *source. We used a glass plate in order to block the source. When removing the plate the initially induced current drops down rapidly because of the charging up of the protection layer.*

By inserting the values of the initial current and the saturation current into eq. (B.1) we can extract an estimate of the resistivity ρ of the layer,

$$\rho \simeq 0.34 \cdot 10^{11}\ [\Omega \cdot \mathrm{m}]\,. \tag{B.2}$$

Appendix C

Gain measurement using a source

For the measurement of the gas gain in the lab we use an ^{55}Fe radioactive source. The ^{55}Fe isotope disintegrates into ^{55}Mn (by capture of a K-shell electron which becomes excited). The electrons of the higher shells in the excited atoms fill the vacancies at the K-shell and fluorescence photons with an energy of 5.9 keV (K_α) 6.49 keV (K_β) are emitted.

The source is placed on top of one channel of the spark setup, letting the fluorescence photons enter the gas and interact with the atoms. Due to the low energy of the photons the photoelectric effect mostly occurs. The photoelectrons that are produced ionise the gas across a short path and lose their energy by ionisation. For an argon based mixture the photoelectron produces a short ionisation track of about 230 electrons/ion pairs. We couple the grid-signal to a honeycomb strip pre-amplifier and feed it in a multichannel analyser to record an energy spectrum. Figure C.1 shows an example spectrum recorded with an Ar/CF_4/iC_4H_10 (95/3/2) gas mixture.

The energy spectrum shown is a distribution around the photon energy broadened by the statistical nature of the energy loss and the gas multiplication. The high peak corresponds to both fluorescence photons of the ^{55}Fe source. However, the energy resolution of the detector was not sufficient to distinguish between these photons. Since an Argon based mixture is used, a second peak at lower energy is visible, known as the argon-escape peak. Quite often, the K-shell fluorescence photons emitted by the excited argon atoms, escape the active are of the detector. The resulting argon-escape peak has an energy of 3 keV.

Using a 10 bit analog-to-digital converter (ADC) the digitised signal is stored in a multichannel analyser (MCA). Subsequently the collected histogram is stored into a PC.

The spectrum is fitted with the function given by eq. C.1 which is the sum of

three gaussians, one for the escape peak and two for the fluorescence peaks,

$$f(x) = p_0 \cdot exp\left(-\frac{(x-p_1)^2}{2p_2^2}\right) + p_3 \cdot exp\left(-\frac{(x-p_4)^2}{2p_5^2}\right) + p_6 \cdot exp\left(-\frac{(x-p_7)^2}{2p_8^2}\right). \quad \text{(C.1)}$$

The fit (see figure C.1) returns 3 parameters for each gaussian. The parameters $p_0 - p_2$ correspond to the argon-escape peak, $p_3 - p_5$ to the K_α and $p_6 - p_8$ to the K_β peak. For the calculation of the gain we use the fitted mean of the gaussian which corresponds to the K_α peak i.e. the parameter p_5.

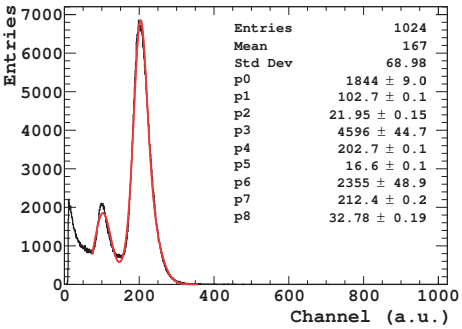

Figure C.1: *A* ^{55}Fe *spectrum recorded with the spark setup. The chamber was flushed with a* $Ar/CF_4/iC_4H_10$ (95/3/2) *gas mixture and the grid voltage was set at* -330 V.

The MCA had a dynamic range of 10V over 1024 channels. Taking into account this we convert the value of the parameter p_5 into mV. Subsequently by using the preamplifier gain (620 mV/pC) we can calculate Q_t, the average value of the total number of electrons created by a 5.9 keV photon. To calculate the gas gain we divide this by Q_0 which is average number of primary electrons created by a 5.9 keV photon in argon,

$$G = \frac{Q_t}{Q_0}. \quad \text{(C.2)}$$

Bibliography

[1] L. D. Broglie, Recherches sur la théorie des Quanta, Ann. Phys. 10 (3) (1925) 22–128.

[2] J. J. Thomson, XL. Cathode Rays, Philosophical Magazine Series 5 44 (269) (1897) 293–316.

[3] S. L. Glashow, Partial-symmetries of weak interactions, Nuclear Physics 22 (4) (1961) 579 – 588.

[4] A. Salam, J. Ward, Electromagnetic and weak interactions, Physics Letters 13 (2) (1964) 168 – 171.

[5] S. Weinberg, A Model of Leptons, Phys. Rev. Lett. 19 (21) (1967) 1264–1266.

[6] D. J. Gross, F. Wilczek, Ultraviolet Behavior of Non-Abelian Gauge Theories, Phys. Rev. Lett. 30 (26) (1973) 1343–1346.

[7] P. W. Higgs, Broken symmetries, massless particles and gauge fields, Physics Letters 12 (2) (1964) 132 – 133.

[8] F. Englert, R. Brout, Broken Symmetry and the Mass of Gauge Vector Mesons, Phys. Rev. Lett. 13 (9) (1964) 321–323.

[9] P. W. Higgs, Spontaneous Symmetry Breakdown without Massless Bosons, Phys. Rev. 145 (4) (1966) 1156–1163.

[10] The ATLAS collaboration, G. Aad, et al., Observation of a new particle in the search for the Standard Model Higgs boson with the ATLAS detector at the LHC, Physics Letters B 716 (1) (2012) 1–29.

[11] The CMS collaboration, S. Chatrchyan, et al., Observation of a new boson at a mass of 125 GeV with the CMS experiment at the LHC, Physics Letters B 716 (1) (2012) 30–61.

[12] J. D. Cockcroft, E. T. S. Walton, Experiments with High Velocity Positive Ions. (I) Further Developments in the Method of Obtaining High Velocity Positive

Ions, Proceedings of the Royal Society of London A: Mathematical, Physical and Engineering Sciences 136 (830) (1932) 619–630.

[13] R. J. van de Graaff, K. T. Compton, L. C. van Atta, The Electrostatic Production of High Voltage for Nuclear Investigations, Phys. Rev. 43 (3) (1933) 149–157.

[14] R. Wideröe, Über ein neues Prinzip zur Herstellung hoher Spannungen, Archiv für Elektrotechnik 21 (4) (1928) 387–406.

[15] L. W. Alvarez, et al., Berkeley Proton Linear Accelerator, Review of Scientific Instruments 26 (2) (1955) 111–133.

[16] E. O. Lawrence, M. S. Livingston, The Production of High Speed Light Ions Without the Use of High Voltages, Phys. Rev. 40 (1) (1932) 19–35.

[17] O. S. Brüning, et al., LHC Design Report, CERN Yellow Reports: Monographs, CERN, Geneva, 2004.

[18] The ALICE Collaboration, K. Aamodt, et al., The ALICE experiment at the CERN LHC, Journal of Instrumentation 3 (08) (2008) S08002.

[19] The ATLAS Collaboration, G. Aad, et al., The ATLAS Experiment at the CERN Large Hadron Collider, Journal of Instrumentation 3 (08) (2008) S08003.

[20] The CMS Collaboration, S. Chatrchyan and et al., The CMS experiment at the CERN LHC, Journal of Instrumentation 3 (08) (2008) S08004.

[21] The LHCb Collaboration, A. A. Alves Jr., et al., The LHCb Detector at the LHC, Journal of Instrumentation 3 (08) (2008) S08005.

[22] G. Apollinari, et al., High-Luminosity Large Hadron Collider (HL-LHC): Preliminary Design Report, CERN Yellow Reports: Monographs, CERN, Geneva, 2015.

[23] https://fcc.web.cern.ch/pages/default.aspx.

[24] http://cepc.ihep.ac.cn/intro.html.

[25] https://www.linearcollider.org/ilc.

[26] http://clic-study.web.cern.ch/.

[27] H. van der Graaf, Gaseous detectors, Nucl. Instr. and Meth. A 628 (1) (2011) 27–30, VCI 2010: Proceedings of the 12th International Vienna Conference on Instrumentation.

[28] K. Potamianos on the behalf of ATLAS collaboration, The upgraded Pixel detector and the commissioning of the Inner Detector tracking of the ATLAS experiment for Run-2 at the Large Hadron Collider, PoS EPS-HEP2015 (2015) 261. arXiv:1608.07850.

[29] ATLAS Phase-II Upgrade Scoping Document, Tech. Rep. CERN-LHCC-2015-020. LHCC-G-166, CERN, Geneva (2015).

[30] V. Gromov, N. Hessey, J. Vermeulen, Front-end intelligence for triggering and local track measurement in gaseous pixel detectors, Journal of Instrumentation 7 (11) (2012) C11003.

[31] F. Hartjes, et al., Test beam studies of the GasPixel transition radiation detectorprototype, Nucl. Instr. and Meth. A 706 (2013) 59 – 64.

[32] T. Behnke, et al., The International Linear Collider Technical Design Report, Volume 4: Detectors (2013). arXiv:1306.6329.

[33] M. Lupberger, The Pixel-TPC: A feasibility study, Ph.D. thesis, University of Bonn (2015).

[34] A. K. Biegun, et al., Proton Radiography With Timepix Based Time Projection Chambers, IEEE Transactions on Medical Imaging 35 (4) (2016) 1099–1105.

[35] W. Blum, W. Riegler, L. Rolandi, Particle Detection with Drift Chambers, Springer, Berlin, 2008.

[36] W. R. Leo, Techniques for Nuclear and Particle Physics Experiments, Springer, Berlin, 1994.

[37] H. Bethe, Zur Theorie des Durchgangs schneller Korpuskularstrahlen durch Materie, Annalen der Physik 397 (3) (1930) 325–400.

[38] F. Bloch, Zur Bremsung rasch bewegter Teilchen beim Durchgang durch Materie, Annalen der Physik 408 (3) (1933) 285–320.

[39] K. A. Olive, et al., Review of Particle Physics, Chin. Phys. C38 (2014) 090001.

[40] S. M. Seltzer, M. J. Berger, Evaluation of the collision stopping power of elements and compounds for electrons and positrons, The International Journal of Applied Radiation and Isotopes 33 (11) (1982) 1189 – 1218.

[41] Stopping Powers and Ranges for Protons and Alpha Particles, International commission on radiation units and measurements, ICRU report 49, 1993.

[42] Stopping powers for electrons and positrons, International commission on radiation units and measurements, ICRU report 37, 1984.

[43] C. Leroy, Principles of Radiation Interaction in Matter and Detection, 2nd Edition, WORLD SCIENTIFIC, 2012.

[44] J. Lindhard, On the properties of a gas of charged particles, Kgl. Danske Videnskab. Selskab, Mat.-Fys. Medd. 28 (8) (1954) 57 pp.

[45] R. M. Sternheimer, S. M. Seltzer, M. J. Berger, Density effect for the ionization loss of charged particles in various substances, Phys. Rev. B 26 (1982) 6067–6076.

[46] http://pdg.lbl.gov/2016/atomicnuclearproperties/.

[47] http://physics.nist.gov/physrefdata/star/text/estar.html.

[48] L. Landau, On the energy loss of fast particles by ionization, J. Phys.(USSR) 8 (1944) 201–205.

[49] P. V. Vavilov, Ionization losses of high-energy heavy particles, Sov. Phys. JETP 5 (1957) 749–751.

[50] H. Bichsel, Straggling in thin silicon detectors, Rev. Mod. Phys. 60 (1988) 663–699.

[51] H. A. Bethe, Molière's Theory of Multiple Scattering, Phys. Rev. 89 (1953) 1256–1266.

[52] P. Auger, Sur les rayons β secondaires produits dans un gaz par des rayons X, C.R.A.S. 177 (1923) 169–171.

[53] http://physics.nist.gov/physrefdata/xcom/html/xcom1.html.

[54] http://magboltz.web.cern.ch/magboltz/.

[55] https://fr.lxcat.net/data/set_databases.php.

[56] F. M. Penning, Über Ionisation durch metastabile Atome, Naturwissenschaften 15 (40) (1927) pp. 818.

[57] C. Ramsauer, Über den Wirkungsquerschnitt der Gasmoleküle gegenüber langsamen Elektronen, Annalen der Physik 369 (6) (1921) 513–540.

[58] D. S. Lemons, A. Gythiel, Paul Langevin's 1908 paper "On the Theory of Brownian Motion" [Sur la théorie du mouvement brownien, C. R. Acad. Sci. (Paris) 146, 530-533 (1908)], American Journal of Physics 65 (11) (1997) 1079–1081.

[59] K. Kleinknecht, Detectors for particle radiation, 2nd Edition, Cambridge University Press, 1998.

[60] http://magboltz.web.cern.ch/magboltz/.

[61] M. A. Chefdeville, Development of Micromegas-like Gaseous Detectors Using a Pixel Readout Chip as Collecting Anode, Ph.D. thesis, University of Amsterdam (2009).

[62] F. Sauli, Gaseous Radiation Detectors: Fundamentals and Applications, Cambridge University Press, 2014.

[63] W. H. Furry, On Fluctuation Phenomena in the Passage of High Energy Electrons through Lead, Phys. Rev. 52 (1937) 569–581.

[64] J. Byrne, Statistics of electron avalanches in the proportional counter, Nucl. Instr. and Meth. 74 (2) (1969) 291 – 296.

[65] H. Raether, Electron Avalanches and Breakdown in Gases, Butterworths, London, 1964.

[66] C. T. R. Wilson, On an Expansion Apparatus for Making Visible the Tracks of Ionising Particles in Gases and Some Results Obtained by Its Use, Proceedings of the Royal Society of London A: Mathematical, Physical and Engineering Sciences 87 (595) (1912) 277–292.

[67] H. Geiger, W. Müller, Elektronenzählrohr zur Messung schwächster Aktivitäten, Naturwissenschaften 16 (31) (1928) 617–618.

[68] D. A. Glaser, Some Effects of Ionizing Radiation on the Formation of Bubbles in Liquids, Physical. Review Letter. 87 (1952) 665–665.

[69] G. Charpak, et al., The use of multiwire proportional counters to select and localize charged particles, Nucl. Instr. and Meth. 62 (3) (1968) 262 – 268.

[70] A. Walenta, J. Heintze, B. Sch The multiwire drift chamber a new type of proportional wire chamber, Nucl. Instr. and Meth. 92 (3) (1971) 373 – 380.

[71] D. Nygren, J. Marx, The Time Projection Chamber, Physics Today 31 (10) (1978) 46.

[72] S. Tavernier, Experimental Techniques in Nuclear and Particle Physics, Springer-Verlag, Berlin, 2010.

[73] http://rd51-public.web.cern.ch/rd51-public/welcome.html.

[74] A. Oed, Position-sensitive detector with microstrip anode for electron multiplication with gases, Nucl. Instr. and Meth. A 263 (2) (1988) 351 – 359.

[75] F. Sauli, A. Sharma, MICROPATTERN GASEOUS DETECTORS, Annual Review of Nuclear and Particle Science 49 (1) (1999) 341–388.

[76] Y. Giomataris, P. Rebourgeard, J. Robert, G. Charpak, MICROMEGAS: a high-granularity position-sensitive gaseous detector for high particle-flux environments, Nucl. Instr. and Meth. A 376 (1) (1996) 29 – 35.

[77] F. Sauli, GEM: A new concept for electron amplification in gas detectors, Nucl. Instr. and Meth. A 386 (2) (1997) 531 – 534.

[78] V. M. B. Carballo, Radiation Imaging Detectors Made by Wafer Post-processing of CMOS Chips, Ph.D. thesis, University of Twente (2009).

[79] M. Fransen, Gridpix: TPC development on the right track, Ph.D. thesis, University of Amsterdam (2012).

[80] http://medipix.web.cern.ch/medipix/.

[81] X. Llopart, M. Campbell, First test measurements of a 64k pixel readout chip working in single photon counting mode, Nucl. Instr. and Meth. A 509 (1-3) (2003) 157 – 163, proceedings of the 4th Internatonal Workshop on Radiation Imaging Detectors.

[82] M. Campbell, et al., Detection of single electrons by means of a Micromegas-covered MediPix2 pixel CMOS readout circuit, Nucl. Instr. and Meth. A 540 (2-3) (2005) 295 – 304.

[83] X. Llopart, et al., Timepix, a 65k programmable pixel readout chip for arrival time, energy and/or photon counting measurement, Nucl. Instr. and Meth. A 581 (1-2) (2007) 485 – 494.

[84] T. Poikela, et al., Timepix3: a 65K channel hybrid pixel readout chip with simultaneous ToA/ToT and sparse readout, Journal of Instrumentation 9 (2014) C05013.

[85] V. Gromov, et al., Prototype of the front-end circuit for the GOSSIP (Gas On Slimmed Silicon Pixel) chip in 0.13 µm CMOS technology, Proceedings of the Workshop on Electronics for LHC and Future Experiments (2006) 253–257.

[86] R. Kluit, et al., Development of a small-scale protope of the GOSSIPO-2 chip in 0.13 µm CMOS technology, Proceedings, Topical Workshop on Electronics for Particle Physics, TWEPP-07, Prague (2007) pp. 277–281.

[87] A. Kruth, et al., GOSSIPO-3: measurements on the prototype of a read-out pixel chip for Micro-Pattern Gaseous Detectors, Journal of Instrumentation 5 (12) (2010) C12005.

[88] F. Zappon, et al., GOSSIPO-4: An array of high resolution TDCs with a PLL control, JINST 7 (2012) C01081.

[89] F. Zappon, It is about time: Design and test of a per-pixel high-resolution TDC, Ph.D. thesis, University of Amsterdam (2015).

[90] J. Schmitz, Adding functionality to microchips by wafer post-processing, Nucl. Inst. and Meth. A 576 (1) (2007) 142 – 149, proceedings of the 8th International Workshop on Radiation Imaging Detectors.

[91] M. Chefdeville, et al., An electron-multiplying "Micromegas" grid made in silicon wafer post-processing technology, Nucl. Instr. and Meth. A 556 (2) (2006) 490–494.

[92] S. Tsigaridas, et al., Precision tracking with a single gaseous pixel detector, Nucl. Instr. and Meth. A 795 (2015) 309 – 317.

[93] V. Gromov, et al, Development of a Front-end Pixel Chip for Readout of Micro-Pattern Gas Detectors, Proceedings, Topical Workshop on Electronics for Particle Physics, TWEPP-08, Naxos (CERN-2008-008) pp. 76–79.

[94] T. Behnke, et al., Testbeams at DESY, EUDET Memo-2007-11.

[95] D. Autiero, et al., Characterization of the T24 electron beam line available at DESY, Tech. rep., OPERA (2005).

[96] W. Koppert, GridPix: Development and characterisation of a Gaseous Tracking Detector, Ph.D. thesis, University of Amsterdam (2015).

[97] D. York, et al., Unified equations for the slope, intercept, and standard errors of the best straight line, American Journal of Physics 72 (3) (2004) 367–375.

[98] X. Llopart, T. Poikela, The Timepix3 manual, CERN, 2nd Edition (2014).

[99] A. Delbart, et al., New developments of Micromegas detector, Nucl. Instr. and Meth. A 461 (1-3) (2001) 84 – 87.

[100] J. Visser, et al., SPIDR: a read-out system for Medipix3 & Timepix3, Journal of Instrumentation 10 (12) (2015) C12028.

[101] Wenzel Elektronik, High voltage power supply N.1130-4, data sheet.

[102] H. Groenstege, J. Kuijt, MiniHV V2: A modular, remote controlled high voltage system, Tech. rep., Nikhef (2011).

[103] G. Barrand, et al., GAUDI - The software architecture and framework for building LHCb data processing applications, in: Proceedings, 11th International Conference on Computing in High-Energy and Nuclear Physics, Padua, 2000, pp. 92–95.

[104] R. Brun, F. Rademakers, ROOT - An object oriented data analysis framework, Nucl. Instr. and Meth. A 389 (2) (1997) 81 – 86.

[105] V. Blobel, C. Kleinwort, A New method for the high precision alignment of track detectors, in: Advanced Statistical Techniques in Particle Physics. Proceedings, Conference, Durham, UK, March 18-22, 2002, 2002, pp. URL–STR(9). arXiv:hep-ex/0208021.

[106] M. D. Gaspari, et al., Design of the analog front-end for the Timepix3 and Smallpix hybrid pixel detectors in 130 nm CMOS technology, Journal of Instrumentation 9 (01) (2014) C01037.

[107] E. Frojdh, et al., Timepix3: first measurements and characterization of a hybrid-pixel detector working in event driven mode, Journal of Instrumentation 10 (01) (2015) C01039.

[108] A. Boldyrev, et al., Tracking performance of GasPixel detectors in test beam studies, Nucl. Instr. and Meth. A 807 (2016) 47 – 55.

[109] T. Alexopoulos, et al., A spark-resistant bulk-micromegas chamber for high-rate applications, Nucl. Instr. and Meth. A 640 (1) (2011) 110 – 118.

[110] M. Vandenbroucke, Discharge reduction technologies for Micromegas detectors in high hadron flux environments, Journal of Instrumentation 7 (05) (2012) C05014.

[111] C. Adloff, et al., Resistive micromegas for sampling calorimetry, SISSA, PoS TIPP2014 (2014) 054.

[112] R. Santonico, R. Cardarelli, Development of resistive plate counters, Nucl. Instr. and Meth. 187 (2) (1981) 377 – 380.

[113] W. Riegler, Induced signals in resistive plate chambers, Nucl. Instr. and Meth. A 491 (1-2) (2002) 258 – 271.

[114] W. Riegler, Extended theorems for signal induction in particle detectors VCI 2004, Nucl. Instr. and Meth. A 535 (1-2) (2004) 287 – 293, proceedings of the 10th International Vienna Conference on Instrumentation.

[115] W. Riegler, Electric fields, weighting fields, signals and charge diffusion in detectors including resistive materials, Journal of Instrumentation 11 (11) (2016) P11002.

[116] F. Bakker, P. Rewiersma, Honeycomb strip amplifier, Tech. rep., Nikhef (1994).

[117] V. Prodanovic, et al., Optimization of Silicon-rich Silicon Nitride Films for Electron Multiplication in Timed Photon Counters, Procedia Engineering 120 (2015) 1111 – 1114.

[118] ORTEC, Model 672 Spectroscopy Amplifier Operating and Service Manual (2002).

[119] Courrier CERN Vol. 19, N° 1, MARS 1979.

[120] S. Tsigaridas, et al., Towards spark-proof gaseous pixel detectors, Journal of Instrumentation 11 (11) (2016) C11016.

[121] M. Furukawa, et al., Surface morphologies of sputter-deposited aluminum films studied using a high-resolution phase-measuring laser interferometric microscope, Appl. Opt. 35 (4) (1996) 701–707.

[122] L. Malter, Thin Film Field Emission, Phys. Rev. 50 (1936) 48–58.

[123] K. Heijhoff, Improving the charge collection efficiency in GridPix, Master's thesis, University of Amsterdam (2016).

[124] Bronkhorst, Industrial Style Digital Mass Flow Meters and Controllers for Gases, data sheet.

[125] F. Sauli, Principles of operation of multiwire proportional and drift chambers, CERN Yellow Reports (1977) 92p.

[126] A. Sharma, Properties of some gas mixtures used in tracking detectors, SLAC ICFA Instrumentation Bulletin 16 (3) (1998) 18p.

[127] W. Diethorn, A methane proportional counter system for natural radiocarbon measurements, Ph.D. thesis, Carnegie Institute of Technology (1956).

S

Summary

The Standard Model of particle physics is a well established theory which classifies the fundamental building blocks of matter and describes their interactions via the exchange of the force carriers of the fundamental forces of nature, excluding the gravity. Its success was verified by the observation of the Higgs boson by the ATLAS and the CMS experiments at the LHC. Nevertheless, the Standard Model falls short in explaining a few phenomena that are observed in nature (matter-antimatter asymmetry, dark matter, etc.).

The scientists that are involved in this endeavour are looking forward to exploit even higher energies, where such physics processes might show up. The use of large machines called accelerators enable the acceleration of particle beams at extremely high energies. In the modern experiments two separate beams are accelerated independently and brought into collision at the interaction point. The energy at the centre of mass of the collisions is sufficient in order to produce new heavy particles. However these particles are unstable and after a short time decay to secondary particles. The interaction point is surrounded by advanced detector systems which literally take photographs of the particles that are produced during the collisions.

The detectors that are used in high energy physics experiments are a stack of several sub-systems each one with a specific functionality. One of the most important sub-systems, which is essential for the performance of the experiments, is the tracking detector. This system consists of several sub-detectors responsible for the reconstruction of the trajectory of the particles which fly away from the interaction point. In order to meet the requirements of the future experiments there are several tracking detector technologies under investigation. A novel detector concept with a large potential for future tracking applications is the GridPix detector.

The GridPix is an innovative detector concept which uses a gas mixture as detection medium, combined with a CMOS pixel chip as active readout anode. The pixels register the avalanche induced signals of ionisation electrons created by incident radiation. The recording of the drift time enables the 3D reconstruction of the creation position of single ionisation electrons with high accuracy.

A conducting grid is integrated on top of the chip by adding a few post-processing steps on the silicon wafers that contain the chips. The grid-holes are precisely aligned to the pixel pads, providing uniform performance. The grid is supported by 50 µm high insulating pillars located between the pixel readout pads, avoiding dead areas. A cathode electrode and a gas tight chamber complete the detector.

An incident ionising particle in the gas volume, creates electron-ion pairs along its trail, see figure S.1. Due to the electric field between the cathode and the grid, the electrons are separated from the ions and drift drift towards the grid and eventually enter a grid-hole. A high electric field between the grid and the chip accelerates any electrons that enter, causing electron avalanches which are registered by the pixels. As a prevention against discharges that might occur due to the high electric field the chip is covered with a thin resistive layer.

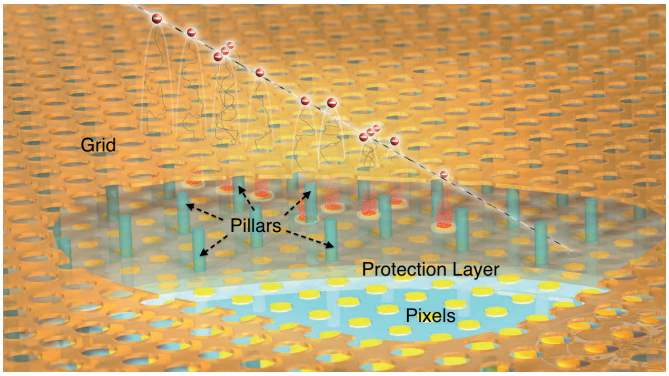

Figure S.1: *Illustration of a GridPix detector showing the grid (orange) supported by pillars (green), the protection layer (grey) and the pixel chip (blue) with readout pads (yellow). An incident ionising particle liberates electrons along its track which drift to the grid, initiating an electron avalanche (red) in the strong electric field below the grid.*

The GridPix technology is still under development. The pixel chips used in GridPix detectors are designed by the Medipix collaboration at CERN. The chips of the Medipix family feature a high granularity pixel array which contains 256×256 pixels. The pixel-size is 55 µm $\times$ 55 µm giving a total area of about 2 cm^2. Previous applications were based on the Timepix chip which provides timing information that enables the recording of the time-of-arrival (ToA) or the time-over-threshold (ToT). Despite the success, there were a few limitations in the position resolution along the drift direction originating from its time-to-digital converter (TDC) with 10 ns resolution and the slow front-end ($\geq$ 100 ns rise-time) which limit the resolution along the drift direction.

The limitations of Timepix chip, led to the realisation of its successor, the Timepix3 chip. The design was aiming to a faster front-end ($\leq$ 25 ns rise-time) and a

high resolution TDC per pixel. In addition, for the performance of GridPix detectors the simultaneous measurement of time via ToA and charge via ToT is essential. In order to implement these topologies within a pixel, a series of prototype chips has been developed and tested towards the final development for the Timepix3 chip.

This thesis is aiming to the development of the GridPix detectors based on the Timepix3 chip and the characterisation of their tracking performance.

In the first place, a miniature GridPix detector based on a prototype chip pronounced as "Gossipo2" has been developed. The Gossipo2 chip was the first chip to implement the topology of a high resolution TDC in each pixel. The chip was produced in a multi-project wafer run and contains a 16×16 pixel array. The chip was turned into a complete GridPix detector, with a drift gap of 1.3 mm and tested in an electron beam at DESY in order to measure its tracking performance.

The detector was flushed with a CO_2/DME (48/52) gas mixture yielding a drift velocity of 5.1 µm/ns and a low diffusion of about 25 µm/$\sqrt{\text{mm}}$. The electron beam was set to an energy of 4.4 GeV with a rate of about 1 kHz/cm^2. The detector was mounted on manually adjustable rotation and translation stages allowing the precise alignment and the investigation of several track-angles.

The results obtained show high performance in terms of efficiency, ionisation-electron position measurement, and tracking precision for a gaseous pixel detector. The efficiency to see at least one hit is 99.8%; the efficiency to record sufficient hits to fit a track is 95.5%. The hit-position resolutions given in Table. S.1 are significantly improved over Timepix chip results in the drift direction, thanks to the fast front-end and high-resolution TDC in each pixel of the chip.

Table S.1: *The hit position resolution at various heights which is associated to the creation position of a single ionisation electron. The resolution is given in three dimensions which defines the size of the resolution voxel.*

z (mm)	σ_x (µm)	σ_y (µm)	σ_z (µm)
0.0	15.9	15.9	66.7
0.6	24.1	24.1	69.5
1.2	30.1	30.1	72.3

The hit-position resolution defines the tracking performance of the detector. For each event, the reconstructed hit positions in three dimensions are projected to the xz and the yz planes and are fitted with a straight line. From the covariance matrix of the fit we derive the track resolution in three dimensions and the angular resolution of each projected angle. The track resolution resolution depends on the track length i.e. the number of ionisations while its average is the fundamental detector resolution and is independent of the track angle.

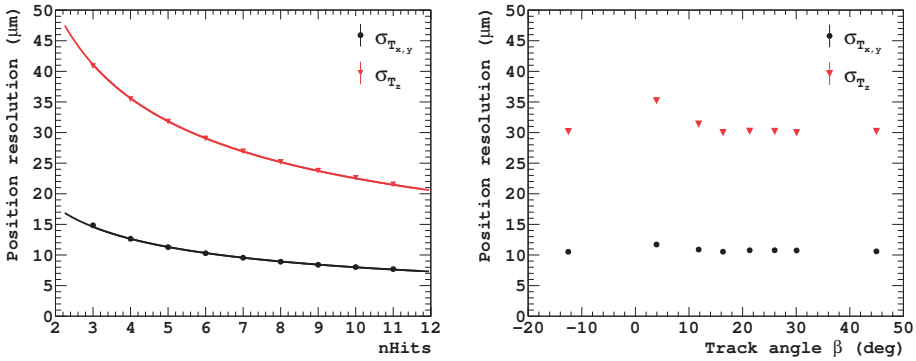

Figure S.2: *On the left, the track position resolution dependence on the number of hits for the in-plane and the drift directions. The curves are fitted with a* $1/\sqrt{N_{\text{hits}}}$ *dependency. On the right, the average track position resolutions which is constant over a wide range of the track angle.*

Figure S.2 shows the results obtained for the track resolution. For a typical track with 6 hits on average, we achieved 10 µm for the in-plane position resolution and about 30 µm for the position resolution along the drift direction. The improved hit-resolution has also a significant impact on the angular resolutions of the fitted tracks, typically 45 mrad, which is improved compared to previous measurements.

The detector has a more fundamental set of track-resolution parameters which consists of a 3D vector ($\sigma_{T_x}, \sigma_{T_y}, \sigma_{T_z}$) and two angles ($\sigma_\alpha$, σ_β). With this information the resolutions in rotated reference frames can be derived.

The tracking performance that was measured with the small scale prototype is the proof of principle for the a high-resolution TDC per pixel. The performance of this prototype chip technology led to a significant improvement to the position resolution in the drift direction, which however is dominated by the timewalk effect. Timewalk is an effect which occurs internally in the chip. It is a result of the variations in the amplitude of the induced signal on the pixels. Due to timewalk, low amplitude pulses need more time to cross the threshold level compared to large ones and as a result they appear to arrive later.

The correction for the timewalk effect is one of the basic motivations which drives the development of GridPix detectors based on the Timepix3 chip. Besides, the improvements in the resolution of its TDC, the Timepix3 offers also the simultaneous measurement of the ToA and the ToT. This feature enables the correction for timewalk, improving further the resolution along the drift direction. Therefore, the next step to take was to develop detectors based on the Timepix3 chip.

We developed a gaseous pixel detector with a drift gap of 14 mm, by using a 60 µm pitch micromegas grid, manually-placed on top of a Timepix3 chip of 55 µm pixel pitch. The detector was tested in a hadron beam at SPS/CERN in order to obtain the correction for timewalk and measure its impact on the tracking performance. The detector was flushed with a CO_2/DME (50/50) gas mixture while a silicon telescope was used as an external track reference. Figure S.3 shows the timewalk correction for the Timepix3 chip obtained with the detector operating at the minimum useful threshold of ~ 500 e^-.

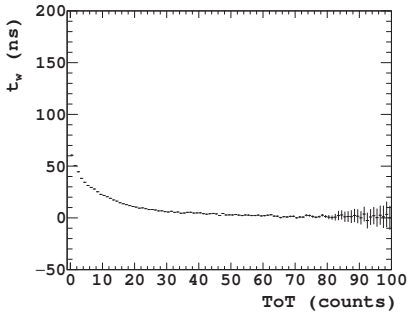

Figure S.3: *The timewalk dependence on the ToT. The timewalk values are used in order to apply a ToT-depended correction of the arrival time direclty on the raw data. As expected the timewalk is larger for low ToT values.*

This is the first timewalk correction for the Timepix3 chip obtained with real particle data. Thanks to the timewalk correction, we measure an improved set of track-resolution parameters, $(\sigma_{T_x}, \sigma_{T_y}, \sigma_{T_z}) = (10, 10, 19)$ µm and $(\sigma_\alpha, \sigma_\beta) = (4.5, 4.5)$ mrad and an improved single hit resolution along the drift direction. Table S.2 shows the single hit position resolution for various drift heights.

Table S.2: *The hit position resolution (corrected for timewalk) at various ionisation heights for a gaseous pixel detector based on the Timepix3 chip.*

z (mm)	σ_x (µm)	σ_y (µm)	σ_z (µm)
0.0	17.3	17.3	36.2
1.0	34.3	34.3	46.7
2.0	45.2	45.2	55.3
5.0	68.3	68.3	75.4
10.0	95.0	95.0	100.2

The results obtained after an offline correction for electric field distortions and show the resolution that can be achieved with a parallel electric field. Due to the remaining systematics, these results find the random error limit to the resolution.

The performance of a GridPix detector with a proper guard and a parallel electric field would be improved. The distortions would be very much reduced and only the timewalk correction would be needed. In addition, a high quality InGrid with no mismatch between grid-holes and pixels would improve further the performance. There would be twice as many hits, improving position and angular track resolution by $1/\sqrt{2}$. However, the reliability of the detectors for long term operation in harsh radiation environments is under question due to the discharges occurring in the gas. A single discharge (or spark) could deliver lethal damage on the sensitive electronics of the pixel chip. The last part of the manuscript is devoted on the studies of the protection layer.

A setup for the characterisation of the performance of protection layers has been developed. The setup has been used in the lab and in a testbeam in order to test the performance of several protection layers against sparks induced by heavy ionising events. Tests performed on dummy and real Timepix3 chips while the setup has been flushed various gas mixtures.

The results obtained with dummy chips show that protection layers of Silicon Carbide (SiC) can be an alternative to the current Silicon-rich Silicon Nitride (SiRN) layers. The sparking tolerance of Timepix3 InGrids equipped with a SiRN protection was also tested. In contrast to experience in an earlier testbeam no damage was found on the layers after the extensive sparking with a high grid capacity. A first conclusion would be that the SiRN layer is quite robust without defects. However, more tests are required to verify if this protection is sufficient for protecting the sensitive electronics of the chip.

The research that has been performed in the context of this thesis shows the great potential of GridPix detectors for future tracking applications. Pixel chips with improved specifications can improve further the position resolution along the drift direction, which can be comparable to the in-plane position resolution. Moreover GridPix detectors equipped with high uniformity protection layers would be able to suppress all the discharges in the future. However the production techniques should be optimised further so that GridPix becomes a mature technology.

Stergios Tsigaridas
Amsterdam
November 2017

S

Samenvatting

Het Standaard Model van de deeltjesfysica is een goed geteste theorie, die de fundamentele bouwstenen van materie en hun onderlinge interactie beschrijft via de uitwisseling van "boodschapper" deeltjes. Deze deeltjes zijn gerelateerd aan de fundamentele natuurkrachten, met uitzondering van de zwaartekracht. Het succes van het standaard model is bevestigd door de observatie van het Higgs deeltje door de ATLAS en CMS experimenten in de Large Hadron Collider (LHC). Echter, een paar processen die in de natuur zijn waargenomen, kunnen niet door het Standaard Model voorspeld worden (de asymmetrie in de materie-antimaterie verhouding, de veronderstelling van het bestaan van donkere materie, etc.).

Betrokken wetenschappers zijn geïnteresseerd in het onderzoeken van het Standaard Model bij hogere energieën, zodat niet voorspelde processen wellicht beter begrepen kunnen worden. Grote machines, die deeltjesversnellers genoemd worden, zijn in nodig om deeltjes te versnellen tot extreem hoge energieën. In moderne experimenten worden twee onafhankelijke deeltjesbundels in tegengestelde richting versneld en met elkaar in botsing gebracht in een interactie punt. De energie in het massamiddelpunt van de botsingen is groot genoeg om nieuwe, zware, deeltjes te produceren. Deze zware deeltjes zijn echter instabiel en vervallen in zeer korte tijd naar secundaire deeltjes. Het interactie punt is omgeven door geavanceerde deeltjes detector systemen, die letterlijk foto's nemen van de secundaire deeltjes die geproduceerd zijn tijdens de botsingen.

De deeltjes detectoren die gebruikt worden in de hoge energie fysica zijn een opeenstapeling van verschillende subsystemen, die elk een specifieke functionaliteit hebben. Een van de belangrijkste subsystemen, essentieel is voor het succes van de experimenten, is een deeltjes volgdetector. Dit systeem bestaat uit verschillende sub-detectoren die verantwoordelijk zijn voor de reconstructie van het spoor van de deeltjes die vanuit het interactiepunt weggeschoten worden. Om aan de vereisten van toekomstige experimenten te voldoen, worden er verschillende volg detector technologieën onderzocht. Een nieuw detector concept, met groot potentieel voor toepassing in toekomstige deeltjes volg detectoren, is de GridPix detector.

GridPix is een innovatief detector concept dat een gasvormig detectie medium combineert met een CMOS pixel chip als actieve uitlees anode. De pixels registeren geïnduceerde signalen van elektronen lawines die veroorzaakt worden door passerende deeltjes. Door het meten van de drijftijd van individuele elektronen in het gas, is met hoge nauwkeurigheid een 3D reconstructie te maken van de ionisatie positie van enkele elektronen.

Bovenop de silicium plak, waarop een serie aan chips is geproduceerd, word met behulp van fotolithografische processen een plaatvormige elektrode aangebracht die via 50 micrometer lange pilaartjes aan de chip bevestigd is. In de elektrode zijn kleine gaatjes ge ëtst die precies zijn uitgelijnd met de pixel uitlees elektroden. Het plaatsen van de chip in een gasdichte kamer met een kathode completeren de detector.

Ioniserende deeltjes die het gas volume passeren, laten een spoor van elektron-ion paren achter op de afgelegde weg, zie figuur S.1. Door het elektrische veld tussen de kathode en het rooster op de chip worden de elektronen gescheiden van de ionen en drijven ze richting de chip, waar ze door een van de gaatjes het rooster passeren. Een groot elektrisch veld tussen het rooster en de chip versnelt de primaire elektronen tot een zodanig hoge energie, dat nieuwe elektron-ion paren geproduceerd kunnen worden. Deze lawine van secundaire elektronen wordt geregistreerd door een pixel op de chip. Ter bescherming tegen ontladingen, die zouden kunnen ontstaan door het grote elektrische veld tussen het rooster en de chip, is een dunne isolerende laag aangebracht op het oppervlak van de chip.

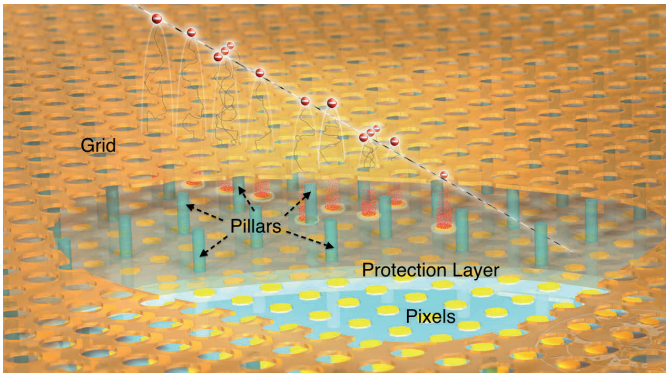

Figuur S.1: *Illustratie van een GridPix detector met het rooster (oranje) ondersteunt door paaltjes (groen), de beschermingslaag (grijs) en de pixel chip (blauw) met de uitlees elektrodes (geel). Een inkomend ioniserend deeltje bevrijd elektronen op zijn weg. De ionisatie elektronen drijven naar het rooster toe en lawine initiëren een lawine in het sterke elektrische veld tussen het rooster en de chip.*

De GridPix technologie is nog in ontwikkeling. De pixel chips die gebruikt worden in GridPix detectoren zijn ontworpen door de Medipix collaboratie op CERN. De chips van de Medipix familie hebben een fijne pixel matrix, die bestaat uit 256×256 pixels. De pixel grootte is 55 µm $\times$ 55 µm zodat de totale chip een oppervlakte heeft van ongeveer 2 cm^2. Vorige GridPix chips waren gebaseerd op de Timepix chip, die tijdsinformatie kan geven in termen van het tijdstip dat een signaal arriveert (ToA) of de tijd dat een signaal zich boven een drempel waarde bevindt (ToT). Ondanks het succes van de Timepix chip werd de positie resolutie in de elektron drijf richting beperkt door de Tijd naar Digitaal Convertor (TDC), met een 10 ns tijdsresolutie, en de trage front-end elektronica, met een stijgtijd van meer dan 100 ns.

De beperkingen van de Timepix chip hebben geleid tot de realisatie van een opvolger, de Timepix3 chip. Het doel van het ontwerp van Timepix3 was een snellere front-end elektronica, met een stijgtijd van kleiner dan 25 ns en een hogere resolutie van de pixel TDCs. Daarnaast is de mogelijkheid om zowel ToA en ToT simultaan te meten essentieel voor de prestaties van GridPix detectoren. Om deze functionaliteiten in de pixels te integreren is een serie aan prototype chips ontwikkeld, die geleid heeft tot het uiteindelijke ontwerp van Timepix3.

De studies in dit proefschrift hebben als doel Gridpix detectoren op basis van de Timepix3 chip te ontwikkelen en te karakteriseren.

Als eerste is een miniatuur GridPix detector ontwikkeld, die gebaseerd is op een Gossipo2 prototype chip. De Gossipo2 chip, was de eerste chip waarbij een hogere resolutie TCD geïntegreerd was in elke pixel. De chip is met meerdere chips tegelijk gefabriceerd op een silicium plak en heeft een pixel matrix van 16×16 pixels. De chip is gebruikt voor het bouwen van een complete GridPix detector, met een dikte van het gas volume van 1.3 mm. Vervolgens is de detector getest in elektronen bundel op DESY om zijn detectie prestaties te meten.

De detector werd gespoeld met een gasmengsel van CO2 en DME in een verhouding van 48:52, resulterend in elektronen drijfsnelheid van 5.1 µm/ns en een elektronen diffusie van ongeveer 25 µm/$\sqrt{\text{mm}}$. De elektronen bundel energie was 4.4 GeV met een deeltjes frequentie van 1 kHz/cm^2. De detector was gemonteerd op een handmatig instelbare rotatie en translatie tafel, zodat precieze uitlijning en belichting onder verschillende hoeken mogelijk was.

Voor een gasvormige pixel detector laten de metingen een relatief hoge detectie efficiëntie, ionisatie positie resolutie en spoor resolutie zien. De efficiëntie van detecteren van tenminste één enkele ionisatie is 99.8%; de efficiëntie voor het kunnen reconstrueren van een volledig spoor is 95.5%. De ionisatie positie resoluties (gegeven in tabel S.1) laten, in de drijfrichting, een significante verbetering zien ten opzichte van GridPix detectors gebaseerd op Timepix chips, door de snellere front-end elektronica en de hogere resolutie TDC in elke pixel van de chip.

Tabel S.1: *De ionisatie positie resolutie op verschillende hoogtes, gerelateerd aan de positie waar de ionisatie heeft plaats gevonden. De resolutie is gegeven in 3 dimensies die de afmetingen van een resolutie voxel definiëren.*

z (mm)	σ_x (µm)	σ_y (µm)	σ_z (µm)
0.0	15.9	15.9	66.7
0.6	24.1	24.1	69.5
1.2	30.1	30.1	72.3

De ionisatie positie resolutie definieert de kwaliteit van het gemeten spoor in de detector. Voor elke deeltjes detectie worden de drie dimensionale gereconstrueerde ionisatie posities geprojecteerd op het xz en yz vlak waarna ze gefit worden aan een rechte lijn. Uit de covariantie matrix van de fit halen we de spoor positie resolutie en de hoek resolutie van elke geprojecteerde hoek. De spoor resoluties zijn afhankelijk van het aantal ionisaties en dus van de lengte van het afgelegde pad in het gas. De resolutie in het zwaartepunt van het spoor is onafhankelijk van de hoek waarmee het deeltje binnenkomt en definieert daarmee de fundamentele detector resolutie.

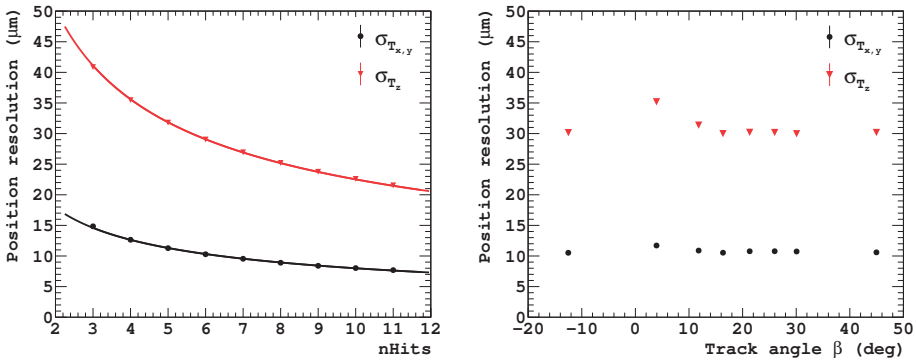

Figuur S.2: *Links, de spoor positie resolutie parallel aan het oppervlak van de chip en de spoor positie resolutie in de drijfrichting, uitgezet tegen het aantal gemeten ionisaties. De curves zijn gefit aan een $1/\sqrt{N_{\text{hits}}}$ functie. Rechts, de gemiddelde spoor positie resolutie, die constant is over een groot bereik van hoeken.*

Figuur S.2 laat de spoor positie resolutie zien als functie van aantal gemeten ionisaties en de hoek van het spoor van het deeltje met het chip oppervlak. Voor een typische meting met 6 ionisaties per spoor, bereiken we een 10 *micron* positie resolutie parallel aan het vlak van de chip en een 30 *micron* positie resolutie in de drijf richting. De verbeterde ionisatie positie resolutie heeft ook effect op de hoek

resoluties van het gefitte spoor, typisch 45 mrad, dat een verbetering is ten opzichte van vorige metingen.

De detector heeft een meer fundamentele set van spoor resolutie parameters, die bestaat uit een 3D vector ($\sigma_{T_x}, \sigma_{T_y}, \sigma_{T_z}$) en twee hoeken ($\sigma_\alpha$, σ_β). Met deze informatie kunnen de resoluties in geroteerde referentie frames bepaald worden.

De kwaliteit van de sporen van de detector, die gemeten zijn met een kleinschalige prototype detector, bewijzen het principe van verbeterde metingen met een hoge resolutie TDC per pixel. De prestaties van deze prototype chip hebben geleid tot een significante verbetering van de positie resolutie in de drijfrichting, die desondanks nog steeds beperkt wordt door het "timewalk" effect. Het timewalk effect is een effect dat voorkomt uit de elektronica van de chip. Het is het resultaat van de variaties in amplitude van de geïnduceerde signalen op de pixels. Door timewalk duurt het voor signalen met een kleine amplitude langer voordat ze over een vooraf ingestelde drempel waarde komen. Vergeleken met signalen van grote amplitude, lijkt het dan of de kleine signalen later arriveren.

De mogelijkheid tot corrigeren van de effecten van timewalk is een van de belangrijkste motivaties die geleid hebben tot de ontwikkeling van GridPix detectoren, gebaseerd op de Timepix3 chip. Behalve de verbeteringen die hebben geleid tot een hogere resolutie TDC, bied de Timepix3 chip ook de functionaliteit voor het simultaan meten van ToA en ToT. Dit biedt de mogelijkheid voor een correctie op de gemeten aankomsttijd van de elektronen, waardoor de resolutie in de drijf richting verbeterd kan worden. Daarom was de volgende stap het ontwikkelen van detectoren gebaseerd op de Timepix3 chip.

We hebben een gasvormige pixel detector ontwikkeld met een 14 mm dik gas volume, door een micromegas rooster met een spoed van 60 µm handmatig bovenop een Timepix3 chip te plaatsen, met een pixel spoed van 55 µm. De detector is getest in een hadronen bundel in de SPS/CERN om het succes van de timewalk correctie en de invloed op de kwaliteit van de gereconstrueerde sporen te testen. De detector werd gespoeld met een CO_2/DME gas mengsel met de verhouding 50:50. Een silicium bundel telescoop is gebruikt als externe referentie. Figuur S.3 laat de timewalk correctie zien voor een Timepix3 chip, verkregen met een detector ingesteld op een minimale bruikbare drempelwaarde van ongeveer 500 elektronen.

Dit is de eerste timewalk correctie die is toegepast voor een Timepix3 chip op metingen van echte deeltjes. Door timewalk correctie zijn de positie resoluties in de drijf richting van enkele ionisaties verbeterd. Dat heeft geleid tot verbeterde spoor resoluties van ($\sigma_{T_x}, \sigma_{T_y}, \sigma_{T_z}$) = (10, 10, 19) µm en ($\sigma_\alpha$, σ_β)= (4.5, 4.5) mrad. De positie resolutie van enkele ionisaties voor verschillende drift afstanden is gegeven in tabel S.2.

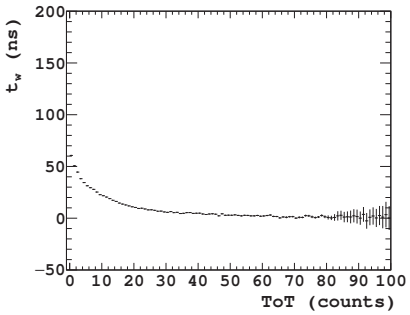

Figuur S.3: *De ToT afhankelijkheid van timewalk. De timewalk waarden zijn gebruikt om een ToT afhankelijke correctie te doen op de arriveer tijd in de ruwe data. Volgens verwachting groeit de timewalk bij kleiner wordende ToT waarden.*

Tabel S.2: *De positie resoluties van enkele ionisaties, gecorrigeerd door timewalk, voor verschillende ionisatie hoogtes, zoals gemeten met een gasvormige pixel detector gebaseerd op de Timepix3 chip.*

z (mm)	σ_x (µm)	σ_y (µm)	σ_z (µm)
0.0	17.3	17.3	36.2
1.0	34.3	34.3	46.7
2.0	45.2	45.2	55.3
5.0	68.3	68.3	75.4
10.0	95.0	95.0	100.2

De positie resoluties van enkele ionisaties, gecorrigeerd door timewalk, voor verschillende ionisatie hoogtes, zoals gemeten met een gasvormige pixel detector gebaseerd op de Timepix3 chip.

De prestaties van GridPix zouden verbeterd kunnen worden door de homogeniteit van het elektrisch veld te verbeteren. Het effect van verstoringen in het elektrisch veld wordt daardoor gereduceerd, zodat alleen een timewalk correctie nodig is. Daarnaast zouden nog betere prestaties te realiseren zijn, met een hoge kwaliteit, goed uitgelijnde Ingrid, met dezelfde spoed als die van de pixels. In dat geval zouden er twee keer zoveel ionisaties gemeten kunnen worden, wat leidt tot een verbetering van een factor $1/\sqrt{2}$ in resolutie. De betrouwbaarheid van de detectoren is, door ontladingen in het gas, niet gegarandeerd bij lange termijn gebruik en intense straling. Een enkele ontlading (of vonk) is in staat onherstelbare schade toe te brengen aan de gevoelige elektronica van de pixel chip. Het laatste deel van dit proefschrift gaat over het bestuderen van een beschermingslaag, die de chip moet beschermen tegen

ontladingen.

Voor het karakteriseren van de prestaties van beschermingslagen is een opstelling ontwikkeld. Deze opstelling is gebruikt in het laboratorium en in een deeltjesversneller, om de beschermende eigenschappen van verschillende beschermingslagen tegen ontladingen te testen. De testen zijn uitgevoerd op zowel echte als model Timepix3 chips, terwijl de detectoren gespoeld werd met verschillende gas mengsels.

De resultaten die verkregen zijn met de model chips, laten zien dat beschermingslagen gemaakt van Silicium Carbide (SiC) een alternatief kunnen zijn voor de huidige Silicium rijke Silicium Nitride (SiRN) lagen. De ontladingstolerantie van Timepix3 Ingrids, die uitgerust waren met een SiRN beschermingslaag, zijn ook getest. In tegenstelling tot ervaringen in een eerdere bundel test, is er geen schade gezien na vele ontladingen, bij een grote rooster capaciteit. Een eerste conclusie zou zijn dat een SiRN laag erg robuust als het geen defecten bevat. Echter, meer testen zijn nodig om te verifiëren of deze laag genoeg bescherming biedt aan de gevoelige elektronica van de chip.

Het onderzoek dat is uitgevoerd in het licht van dit proefschrift laat zien dat er een groot potentieel is voor GridPix detectoren in toekomstige deeltjes volg detectoren. Pixel chips met verbeterde specificaties kunnen de positie resolutie in de drijf richting verder verbeteren, zodat deze vergelijkbaar is met de positie resolutie parallel aan het vlak van de chip. Bovendien, zouden GridPix detectoren die uitgerust zijn met een zeer uniforme beschermingslaag, in staat zijn alle ontladingen te onderdrukken. Echter, de productie technieken moeten verder geoptimaliseerd worden, zodat GrixPix een volwassen technologie wordt.

Stergios Tsigaridas
Amsterdam
November 2017

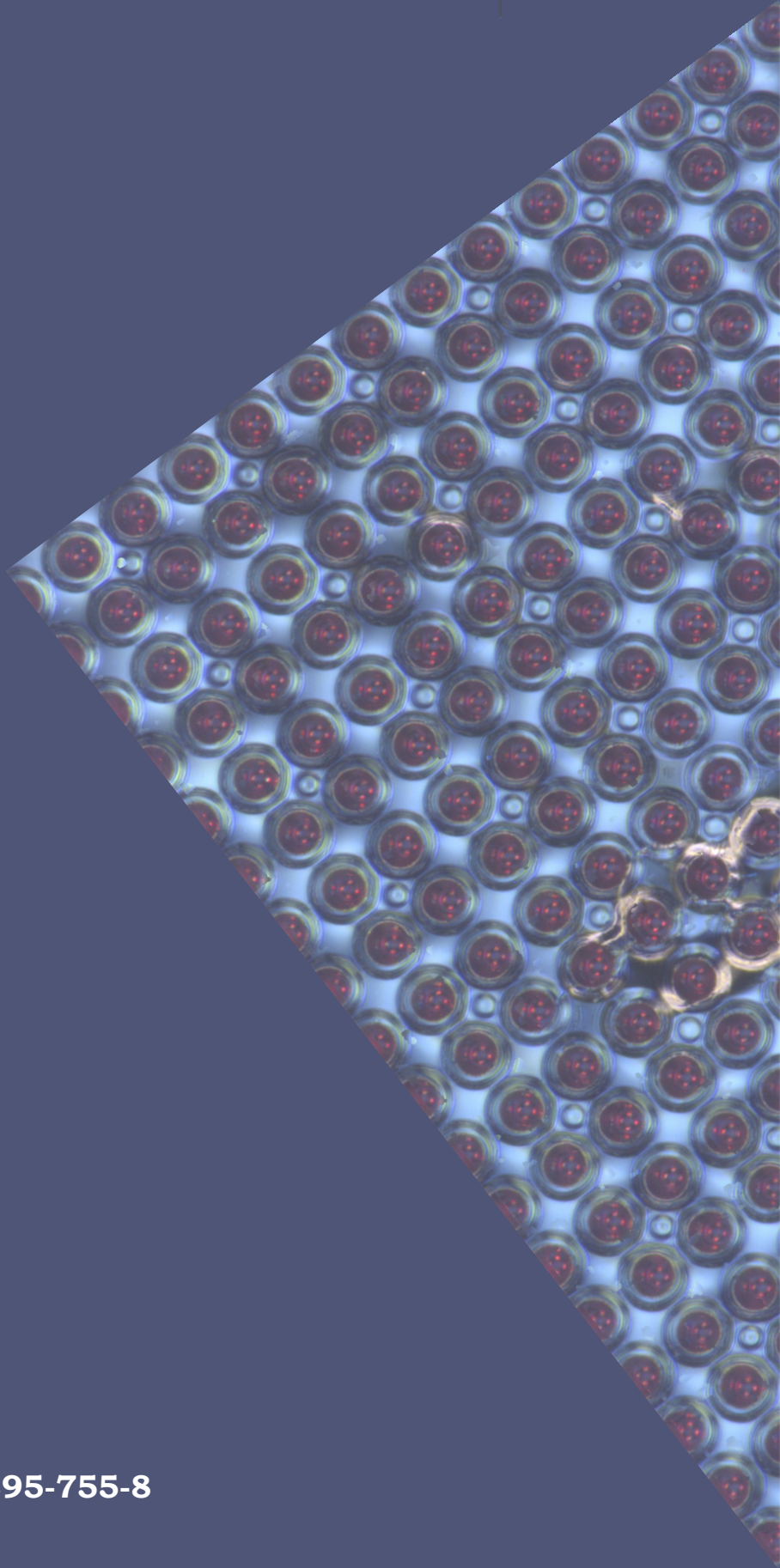

ISBN 978-946-295-755-8